

REPORT DOCUMENTATION PAGE			Form Approved OMB NO. 0704-0188	
<small>Public reporting burden for this collection of information is estimated to average 1 hour per response, including the time for reviewing instructions, searching existing data sources, gathering and maintaining the data needed, and completing and reviewing the collection of information. Send comment regarding this burden estimate or any other aspect of this collection of information, including suggestions for reducing this burden, to Washington Headquarters Services, Directorate for Information Operations and Reports, 1215 Jefferson Davis Highway, Suite 1204, Arlington, VA 22202-4302, and to the Office of Management and Budget, Paperwork Reduction Project (0704-0188), Washington, DC 20503.</small>				
1. AGENCY USE ONLY (Leave blank)	2. REPORT DATE 26 October 2000	3. REPORT TYPE AND DATES COVERED FINAL 15 July 1996 - 14 July 2000		
4. TITLE AND SUBTITLE Interdendritic Fluid Flow Effects on Single Crystal Grain Defects		5. FUNDING NUMBERS DAAH04-96-1-0321		
6. AUTHOR(S) R.A. Overfelt				
7. PERFORMING ORGANIZATION NAMES(S) AND ADDRESS(ES) Space Power Institute Auburn University Auburn, AL 36849		8. PERFORMING ORGANIZATION REPORT NUMBER		
9. SPONSORING / MONITORING AGENCY NAME(S) AND ADDRESS(ES) U.S. Army Research Office P.O. Box 12211 Research Triangle Park, NC 27709-2211		10. SPONSORING / MONITORING AGENCY REPORT NUMBER AR036194.2-RT-DPS		
11. SUPPLEMENTARY NOTES The views, opinions and/or findings contained in this report are those of the author(s) and should not be construed as an official Department of the Army position, policy or decision, unless so designated by other documentation.				
12a. DISTRIBUTION / AVAILABILITY STATEMENT Approved for public release; distribution unlimited.				
<div style="text-align: right;"> <b>DTIC QUALITY INSPECTED 4</b>  <b>20001122 125</b> </div>				
13. ABSTRACT (Maximum 200 words) <p>This research project has been investigating the phenomenon of grain defect formation in nickel-base superalloys. Cylindrical samples of the nickel-based multicomponent alloy PWA 1484 were produced by Howmet Corporation. Utilization of this alloy enabled the application in this research of previous data on this alloy on dendrite arm spacings and thermophysical properties. Samples were re-solidified under carefully controlled laboratory conditions to modify the solidification length scales (mushy zone lengths and dendritic spacings) and the density differences within the mushy zone during solidification. The primary dendrite arm spacings that developed in the Bridgman-grown samples were examined in terms of current theoretical models of the effects of process parameters. Low thermal gradient conditions necessitated modifying the theoretical relationship for primary dendrite arm spacings by the factor <math>[1+f(\phi)]</math>, where <math>f(\phi)</math> is a function of the ratio of radial-to-longitudinal thermal gradients (<math>G/G_L</math>). Validated computational models of the directional solidification process showed that the mushy zone isotherms were flat for these conditions. In addition, for the range of thermal gradients and solidification velocities investigated (<math>\sim 5\text{-}50\text{ }^\circ\text{C/cm}</math> and <math>0.0005\text{--}0.01\text{ cm/sec}</math>, respectively), no samples exhibited channel segregates or freckle grain defects, in agreement with industrial experience for flat mushy zone isotherms.</p>				
14. SUBJECT TERMS Casting, Solidification, Defects, Dendrite Arm Spacing			15. NUMBER OF PAGES	
			16. PRICE CODE	
17. SECURITY CLASSIFICATION OR REPORT UNCLASSIFIED	18. SECURITY CLASSIFICATION OF THIS PAGE UNCLASSIFIED	19. SECURITY CLASSIFICATION OF ABSTRACT UNCLASSIFIED	20. LIMITATION OF ABSTRACT UL	

Grant Number: DAAH04-96-1-0321

Principal Investigator: Dr. R.A. Overfelt

### Problem Statement

Directionally solidified and single crystal castings of multicomponent nickel-base superalloys often exhibit spurious, surface grain defects in their final microstructures. Such grain defects (often called 'freckles') are believed to be due to convective instabilities that form in the mushy zone due to normal segregation of lower density elements and inverse segregation of higher density elements. Convective instabilities in the mushy zone can sweep materials out of the mushy zone and form non-aligned grains and regions of segregation that lower the mechanical properties of the castings. The dendrite arm spacings in the mushy zone microstructure can influence the convective instability by increasing the permeability of the mushy zone through larger primary dendrite spacings or by decreasing the permeability of the mushy zone through smaller primary dendrite arm spacings. The segregation and accompanying grain defects could be prevented by proper design of the basic casting process if a more detailed scientific understanding of the mushy zone microstructure was available for application in numerical process simulations. The specific aims of this project were to: (1) develop a fundamental understanding of the development of dendritic microstructure in the mushy zone for nickel-based superalloys, in general, and PWA 1484 alloy in particular; and (2) evaluate the practical impact of solidification process parameters of withdrawal velocity ( $V$ ) and applied thermal gradient ( $G$ ) to devise empirical criteria functions that manufacturers could utilize in computer simulations of solidification to predict and eliminate these defects.

### Most Important Results

#### (1) Dendrite Arm Spacings

The primary arm spacings that developed in the Bridgman-grown samples were examined in terms of current theoretical models of the effects of process parameters. Under conditions of high longitudinal thermal gradients ( $G_L \geq 30^\circ\text{C}/\text{cm}$ ), only negligible radial thermal gradients ( $G_r$ ) were found in the samples. For such experimental conditions, the primary dendrite arm spacings ( $\lambda_1$ ) were well described by the theoretical relationship  $\lambda_1 \propto G^{-1/2} V^{-1/4}$ . In contrast, at low longitudinal thermal gradients ( $G_L \leq 30^\circ\text{C}/\text{cm}$ ), a significant radial thermal gradient ( $G_r$ ) was found in the directionally solidified samples and the presence of radial temperature gradients enhanced secondary arm growth which increased the primary arm spacings. These conditions necessitated modifying the theoretical relationship for primary dendrite arm spacings by the factor  $[1+f(\phi)]$ , where  $f(\phi)$  is a function of the ratio of radial-to-longitudinal thermal gradients ( $G/G_L$ ). The modified relationship,  $\lambda_1 \propto [1+f(\phi)] G^{-1/2} V^{-1/4}$ , was found to match the experimental results very well.

This finding has important practical implications for the production of single crystal castings. Investment casting of production size single crystals is usually accomplished under conditions of low axial thermal gradients. Radial thermal gradients can then become significant in comparison. Thus the actual primary dendrite arm spacings would

be expected to be larger than the spacings theoretically predicted. Larger dendrite arm spacings would lead to increased permeability of the mushy zone and a greater potential for interdendritic convection effects and freckle defects. Additional work is required to further quantify this result and extend it to production casting systems.

(2) *Effects of Process Parameters (G and V)*

Prior data from a limited research project on the nickel-based multicomponent alloy PWA 1484 indicated that it would be prudent to obtain a much larger set of samples of this same alloy and expand the investigation to cover a wider range of process parameters. Forty-eight cylindrical samples (8 inch long and with diameters up to 0.75 inch) were produced at Howmet Corporation in 1997 and shipped to Auburn University for our controlled directional solidification experiments. These samples were all that have been required from our industry sponsors for us to thoroughly investigate the effects of the following experimental parameters:

- (1) Axial Thermal Gradient ( $\sim 5\text{-}50\text{ }^{\circ}\text{C}/\text{cm}$ )
- (2) Solidification Velocity ( $\sim 0.0005 - 0.01\text{ cm}/\text{sec}$ )
- (3) Constant vs. Changing Velocity Conditions (intermittent start/stop)

None of these samples exhibited freckle grain defects or regions of segregation commonly called channel segregates.

An axisymmetric heat transfer and fluid flow model of the directional solidification process (furnace, retort, crucible, and sample) was developed using the commercial finite-volume code called SAINTS. This software is very well documented public domain software with accessible source code. Excellent agreement was found between the computational model and the experimental thermocouple data from the casting experiments.

The computational model showed that radial thermal gradients were very low in these samples and the resulting mushy zone interfaces were quite flat. These results were discussed with Dr. Tony Giamei of the United Technologies Research Center. Dr. Giamei noted unpublished research that indicates freckle grain defects are rarely seen in samples when the mushy zone is within  $10^{\circ}$  of horizontal whereas the defects are almost a certainty when the mushy zone exceeds  $30^{\circ}$  of horizontal. This is in excellent agreement with our experimental data.

**REPORT DOCUMENTATION PAGE (SF298)**  
**(Continuation Sheet)**

Page 4 of 5

**Grant Number:** DAAH04-96-1-0321

**Principal Investigator:** Dr. R.A. Overfelt

**List of Manuscripts** (copies attached)

1. "Influence of Bulk Convection on Freckle Formation in Casting," V. Sahai, R.A. Overfelt and P. Banerjee, Proceedings of the Fourth International Special Emphasis Symposium on Superalloys 718, 625, 706 and Derivatives, Edward A. Loria, Ed. 1997 (TMS, Warrendale, PA) pp. 107-118.
2. "Two-dimensional Combined Radiation and Conduction Transient Heat Transfer in Directional Solidification," Deming Wang, Harry Whitesell, and Tony Overfelt, Proceedings of the 1999 ASME Design Engineering Technical Conference, Sept. 12-15, 1999, Las Vegas, NV.
3. "Influence of Solidification Variables on the Dendrite Arm Spacings of Ni-base Superalloys," H. S. Whitesell, L. Li, and R.A. Overfelt, Metallurgical and Materials Transactions, Vol. 31B, June 2000, pp. 546-551.
4. "Influence of Directional Solidification Variables on the Cellular and Primary Dendrite Arm Spacings of PWA1484," L. Li and R.A. Overfelt, paper submitted to J. Materials Science.
5. "Influence of Solidification Variables on the Microstructure, Macrosegregation, and Porosity of Directionally Solidified Mar-M247," Harry S. Whitesell and Ruel A. Overfelt, paper submitted to Materials Science and Engineering journal.

**List of Conference Presentations**

1. "Influence of Bulk Convection on Freckle Formation in Casting," V. Sahai, P. Banerjee and R. Overfelt, manuscript presented at the Fourth International Special Emphasis Symposium on Superalloys 718, 625, 706 and Derivatives, June 15-18, 1997, Pittsburgh, PA.
2. "Thermophysical and Related Property Measurements for Casting Process Design," Ruel A. Overfelt, presented at the 102nd AFS Casting Congress, Atlanta, GA, May 10, 1998.
3. "Porosity Formation in Directionally Solidified Mar-M-247 Castings: Theoretical Model," Deming Wang, Harry Whitesell, Ruel. A. Overfelt, presented at the 1999 Annual TMS Fall Meeting, Oct 31 - Nov. 4, 1999, Cincinnati, OH.
4. "Porosity Formation in Directionally Solidified Mar-M-247 Castings: Experimental Characterization," Harry Whitesell and Ruel. A. Overfelt, presented at the 1999 Annual TMS Fall Meeting, Oct 31 - Nov. 4, 1999, Cincinnati, OH.
5. "Computational Simulation of the Directional Solidification of PWA1484," Deming Wang, Lichun Li, Ruel A. Overfelt, presented at the 1999 Annual TMS Fall Meeting, Oct 31 - Nov. 4, 1999, Cincinnati, OH.



6. "Heat Transfer Simulation in Directional Solidification," D. Wang and R.A. Overfelt, presented at the Southeastern Conference On Theoretical and Applied Mechanics - SECTAM XX, April 18, 2000, Callaway Gardens, GA.
7. "Microstructure and Segregation of Directionally Solidified Superalloy PWA 1484," L. Li, H.S. Whitesell, and R.A. Overfelt, presented at the Southeastern Conference On Theoretical and Applied Mechanics - SECTAM XX, April 17, 2000, Callaway Gardens, GA.

### Scientific Personnel

Principal Investigator:	Dr. R.A. (Tony) Overfelt, Auburn University
Post-Doctoral Fellows:	Dr. Vivek Sahai, Auburn University
	Dr. Probal Banerjee, Auburn University
	Dr. Deming Wang, Auburn University
Graduate Research Assts:	Mr. Lichun Li, Auburn University
	(Ph.D. expected in May 2001)
	Mr. Harry Whitesell, Auburn University
	(Currently working for Applied Materials Inc., Santa Clara, CA; Ph.D. expected in May 2001)

### Reportable Inventions

None

# **Influence of Bulk Convection on Freckle Formation in Castings**

V. Sahai, R. A. Overfelt, and P. Banerjee

Space Power Institute, 231 Leach Center, Auburn University, Auburn, Alabama 36849

## **ABSTRACT**

In recent years, there has been an increased usage of single crystal superalloys in high temperature components because of the requirements for high creep resistance. For these complex alloys, it is necessary to understand the molten alloy convective phenomena that can cause deleterious grain defects. In particular, it is believed that the penetration of the bulk convection into the mushy zone can assist in the initiation of upward flowing liquid jets, i.e. channels, which sweep dendritic fragments out of the mushy zone and into the bulk liquid. These fragments can then serve as nuclei for growth of spurious grains that lead to defects called freckles. In the present work, a detailed quasi-steady state, axisymmetric FIDAP model is utilized to simulate the thermal buoyancy convection that occurs during directional solidification. The governing equations for the alloy and the crucible are solved subject to appropriate boundary conditions to determine the velocity and temperature distributions. The results obtained show how the major process parameters such as solidification velocity, and crucible diameter influence convection in the mushy zone. Finally, the numerical results are shown to agree with existing experimental data on freckle formation in metal alloy systems.

## **I. INTRODUCTION**

New alloys and turbine blade designs for next generation aircraft promise to continue pushing the limits of manufacturing technology by requiring ever more complex components to be produced. Unfortunately, the more complex the geometry of the turbine blade, the lower the production yield and the higher the cost of the casting. In fact, scrap rates of 40% are common with some single crystal designs due to grain defects referred to as slivers, equiaxed grains, freckles, and freckle chains. In addition to the costs of recurring scrap, these spurious grain defects can significantly delay the introduction of new casting designs as foundry personnel are forced to empirically adjust their processes prior to full-scale production. Currently, the fundamental solidification phenomena controlling the origins of these defects are only qualitatively understood.

In general, single crystal turbine blades are cast in a specialized vacuum furnace with two compartments, a hot zone and a cold zone as shown in Figure 1(a) below. A baffle is used to separate these chambers and minimize energy exchange between them except for a circular opening for the mold. To increase productivity, multiple parts are usually cast in a cluster of molds. Initially, the mold cluster sits inside the hot zone above the melting temperature. Liquid metal is then poured into the mold, and the mold is gradually withdrawn into the cold

zone to establish directional solidification conditions. Single crystal growth of highly aligned dendrites as shown in Figure 1(b) is achieved through a starter block and a grain selector to ensure that the casting originates from a single grain. A copper chill plate is usually used to improve the vertical heat flux and columnar grain growth in the starter block.

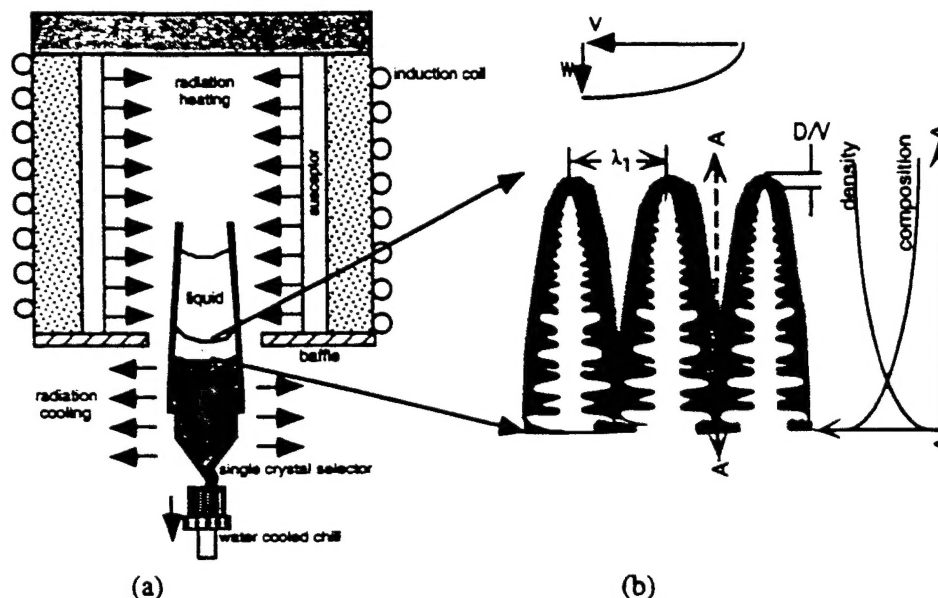


Figure 1.(a) Process schematic of single crystal investment casting process  
(b) Highly aligned columnar growth with interdendritic liquid of less density than bulk liquid.

Single crystal turbine blades produced by this process often contain defects called freckle chains on their outer surface. Freckle chains are extended trails of macrosegregation containing excess eutectic material, second phase particles, and small equiaxed grains. Giamei and Kear [1] and Copley et al.[2] showed that freckle chains are caused by upwardly flowing jets originating in the mushy zone. Although the exact mechanism for debris generation is unknown [3], these jets are believed to be responsible for causing the erosion of dendrite arms and leaving a trail of dendritic debris. Copley et al.[2] showed that the location of the freckles is influenced by mushy zone orientation and shape.

Sample and Hellawell [4] deduced a phenomenological model which described the initiation of freckle chains. According to this model, the key event involves a perturbation, possibly caused by the convection from the bulk fluid, which initiates a plume. The plume draws the surrounding low density segregated liquid from the mushy zone. This flow causes a local depression in the liquidus and produces an open channel, thus providing a self-sustaining path for feeding the plume. McCay [5] postulated that the pluming could be the result of a Rayleigh-Bernard instability at the interface between the bulk fluid and the mushy zone. These plumes are postulated to be the initiating mechanisms for freckle chains.

The formation of freckles may be enhanced by low thermal gradients, low solidification velocities, and a large density inversion of the segregated liquid. Copley et al.[2] suggested that the casting's cooling rate should be above a critical cooling rate or freckles would be likely. Sarazin and Hellawell[6] calculated mushy zone Rayleigh numbers to characterize the freckle formation tendency. They showed that increases in interdendritic spacing or density differences caused by temperature and/or composition changes enhance the potential for freckle formation. Pollock et al. [7] also investigated the dominating influence of cooling rate and resultant primary dendrite arm spacing on freckle chain formation in a series of directionally solidified nickel-based superalloys. Their results showed clearly that decreasing the interdendritic spacing would decrease the permeability of the mushy zone and retard feeding and development of plumes essential for freckle formation.

Muller [8] in his monograph on crystal growth extensively examined the natural convection in simply shaped cavities and determined the critical Rayleigh numbers for the onset of steady convection and for transition from steady to unsteady convection over a wide range of aspect ratios for a top seeded Bridgman apparatus. McCay et al.[9] studied the thermosolutal convection in the presence of a mushy zone in the directional solidification of aqueous ammonium chloride materials by optical and laser particle tracking techniques. Dependent upon the Rayleigh number, they noticed both Bernard type cellular convection and pluming flows. The presence of a mushy zone increased resistance to flow and raised the critical Rayleigh numbers for onset of both the cellular and plume-like flows. These trends are consistent with the results described by Sample and Hellawell[4] and Pollock[7]. This work of McCay et al. [9] is especially useful in understanding the convection regimes and provides insight for developing mathematical and computational models of freckle formation.

Heinrich et al.[10] developed a mathematical model which simulated the convection in directionally solidified binary alloys. Their results showed that the interdendritic convection in the mushy zone is mainly driven by the convection in the bulk liquid. These results were confirmed by a finite element analysis of a simple 2-D rectangular cavity with adiabatic side walls performed by Felicelli et al.[11]. Their predictions of the location of channels agreed with known experimental observations. Motakef[12] developed scaling laws for the convective flow for bottom seeded vertical Bridgman crystal growth and showed that increases in the crucible Rayleigh number due to the increases in the temperature gradient or length scale exponentially increases the strength of the convective flow. Sahai [13] showed that increases in the crucible diameter also enhances the size and strength of the convective cells in a Bridgman apparatus.

In a separate study[14], the authors of the present paper developed a computational model of an investment cluster of a nickel based superalloy PWA 1484 cast at HOWMET Corporation. This study showed that mushy zone orientation and the volumes of the different parts of the casting have a major influence on freckle formation. It also confirmed the importance of cooling rates in the development of freckles.

The above-mentioned study concluded that the interaction between the low-density segregated liquid in the mushy zone and the natural convection in the bulk liquid must be clearly understood if quantitative predictions of freckle chains in complex turbine components are to be realized. The chemistries of alloys like PWA 1484 are very complex and there are little data available on the phase diagram or segregation coefficients for this alloy. The focus will therefore be placed on understanding the thermal behavior of these systems. In this paper, a computational model is presented which examines the thermal buoyancy convection during the directional solidification of nickel-based superalloys. The model will be used to study the penetration of the bulk convection into the mushy zone. The effect of the major process parameters such as aspect ratio (changes in diameter), withdrawal rate (which influences the solidification rate), and thermal gradient were studied. In this work results showing the effects of diameter and withdrawal rate are shown. The predictions from the model will then be compared to known experimental results on freckle formation.

## II. Model Description

The heat and mass transfer processes that occur during directional solidification are extremely complicated. In order to make the problem tractable, a somewhat simplified numerical model is considered in the present work. This section describes the geometry of the model used and presents the appropriate governing equations. In the directional solidification process, there is a continuous translation of the ampoule through the furnace which results in a time dependent process. Between the initial and final transients, however, Su et al.[15] (for aluminum-copper alloys), Overfelt et al.[16] (for Inconel 718), and Wang [17] (for gallium-doped germanium) found that there exists a region where the crystal solidification rate equals the ampoule translation rate. The dendrite arm spacing remains constant in this regime. The present model describes the convection that occurs in this regime. The translation of the ampoule can be simulated by assuming that the melt of a given composition is introduced at the top of the ampoule at a uniform velocity. At the same time, the solidified crystal of the same

average composition is continuously removed at the bottom with a growth rate equal to melt input velocity. The ampoule is assumed to be sufficiently long so that the transients in velocity, temperature, pressure, and concentration due to the decrease in melt length and displacement of the ampoule can be safely neglected. The assumption of a long ampoule also justifies the neglect of thermal end effects and avoids the initial and final transients that occur during crystal growth.

One of the primary purposes of this study was to consider different diameter-to-length ratios. In order to avoid numerical instabilities due to application of inlet conditions, it was necessary to add an additional adiabatic zone at the top. This extended length model ensures that the bulk convection cell will not distort the flow at the inlet. The dimensions associated with this model are given in Table 1.

**Table 1. Nondimensional Model Parameters**

Property	Superalloy	Crucible
Density	1.0	0.4818
Melt Viscosity	$Pr=0.1635$	
Specific Heat	$dH/dT$ ; see Eq. 6	1.6736
Melt Thermal Conductivity	1.0	
Volume Expansion	1.0	
Latent Heat	$St=.3185$	
Solid Conductivity	$k_s/k_m = 0.8016$	$k_{cr}/k_m = 0.1635$
Crucible Thickness		0.01860
Crucible Inner Diameters Investigated		0.12, 0.079, 0.040
<b>Growth Process Parameters</b>		
Bulk Rayleigh Numbers Investigated	$7.2 \times 10^8$ , $4.5 \times 10^8$ (hot zone of $1600^\circ\text{C}$ , and $1500^\circ\text{C}$ at $1g$ )	
Nondimensional Liquidus Temperatures	0.7316, 0.8778	
Nondimensional Solidus Temperatures	0.6060, 0.7296 (for Rayleigh numbers listed above)	
Maximum & Minimum Temperatures	1.0 & 0.0	
Sample Length	12 cm	
Top Adiabatic Zone Length	4 cm	
Growth Rates Investigated	$Pe=0.15, 0.30, 0.75, 1.50$ , and $3.00$ (velocities from $0.0005$ to $0.01$ cm/s)	

To model both the convective and heat transfer processes which occur, the applicable set of continuity, motion, and energy equations for the growth material and ampoule are simplified using the ideas of the quasi-steady state model described above. The melt material is considered to be incompressible and Newtonian, and the velocity and temperature fields are assumed to be axisymmetric. Coupling of the thermosolutal buoyancy effects in the mushy zone with the bulk convection effects is neglected in this work. The solidification of the growth material is treated as a porous medium. The governing equations are thus written in terms of a superficial ('Darcian') velocity which can be defined as:  $v = (1-fs(T))v_l$  and  $w = (1-fs(T))w_l$  where  $fs(T)$  is the fraction solid and  $v_l$  and  $w_l$  represent the actual liquid velocities in the radial and axial direction. Since a major theme of the present research is to conduct parametric studies, the equations are written in their nondimensional form by scaling the variables with respect to their characteristic values. The characteristic values used for scaling lengths,



velocities, and pressures are respectively,  $L$ ,  $\alpha_m/L$ , and  $(\rho_m \alpha_m^2)/L^2$ . Here,  $L$  represents the length of the crucible,  $\rho_m$  is the density of the melt, and  $\alpha_m$  is the thermal diffusivity of the melt. For the temperature, it is convenient to use the following dimensionless form:

$$\theta = \frac{T - T_c}{T_h - T_c} = \frac{T - T_c}{\Delta T} \quad (1)$$

where  $T_c$  and  $T_h$  are respectively the maximum and minimum temperatures in the cold and hot zones of the furnace. To account for the advection of latent heat in the mushy zone, the enthalpy form of the energy equation was used. The enthalpy was nondimensionalized with respect to the product of the melt specific heat and overall temperature difference ( $c_p \Delta T$ ). The dimensionless form of the equations governing the mass, momentum, and heat transfer are then

$$\frac{1}{r^*} \frac{\partial}{\partial r^*} (r^* v^*) + \frac{\partial}{\partial z^*} (w^*) = 0 \quad (2)$$

Momentum Equations:

$$\begin{aligned} \frac{1}{(1 - fs(T))^2} (v^* \frac{\partial w^*}{\partial r^*} + w^* \frac{\partial w^*}{\partial z^*}) = - \frac{\partial p^*}{\partial z^*} - Ra Pr (\theta - 1) \\ + \frac{Pr}{(1 - fs(T))} \left( \frac{1}{r^*} \frac{\partial}{\partial r^*} \left( r^* \frac{\partial w^*}{\partial r^*} \right) + \frac{\partial^2 w^*}{\partial z^{*2}} \right) - \frac{Pr}{Da_z} w^* \end{aligned} \quad (3)$$

$$\begin{aligned} \frac{1}{(1 - fs(T))^2} (v^* \frac{\partial v^*}{\partial r^*} + w^* \frac{\partial v^*}{\partial z^*}) = \\ - \frac{\partial p^*}{\partial r^*} + \frac{Pr}{(1 - fs(T))} \left( \frac{\partial}{\partial r^*} \left( \frac{1}{r^*} \frac{\partial (r^* v^*)}{\partial r^*} \right) + \frac{\partial^2 v^*}{\partial z^{*2}} \right) - \frac{Pr}{Da_r} v^* \end{aligned} \quad (4)$$

Energy Equation:

$$v^* \frac{\partial H^*}{\partial r^*} + w^* \frac{\partial H^*}{\partial z^*} = \frac{1}{r^*} \frac{\partial}{\partial r^*} \left( r^* \frac{\partial (k^* H^*)}{\partial r^*} \right) + \frac{\partial^2 (k^* H^*)}{\partial z^{*2}} \quad (5)$$

Here,  $Pr$  is the Prandtl number ( $\nu/\alpha_m$ ),  $Ra$  is the Rayleigh number ( $g \beta_T \Delta T L^3/\alpha_m \nu$ ), and  $Da$  is the Darcy number ( $K_z/L^2$ ,  $K_r/L^2$ ). The symbols undefined so far include the kinematic viscosity:  $\nu$ , the volumetric coefficient of thermal expansion:  $\beta_T$ , the nondimensional thermal conductivity:  $k^* = (k/k_m)$ , and the permeability:  $K_z$  (axial) and  $K_r$  (radial).

To model the effects of phase change from melt to solid, temperature dependent functions were used for the thermal conductivity, permeability, and enthalpy. The thermophysical properties utilized were typical for nickel-based superalloys [18]. The specific heat is computed from the slope of the enthalpy-temperature curve based on the temperature at the point. The enthalpy-temperature curve is constructed such that it reflects the specific heat of

the solid( $c_{ps}$ ), liquid( $c_{pl}$ ), and the latent heat release( $\Delta H$ ) in the mushy zone. The latent heat release in the mushy zone is controlled by the fraction solid curve  $f_s(T)$  of the growth material. The fraction solid values were determined by using a cooling curve analysis [14, 19]. The fraction solid curve used in this analysis is shown in Figure 2. The equation for the enthalpy function can be written as:

$$H(T) = \int c_{ps} dT + \Delta H (1 - f_s(T)) + \int c_{pl} dT. \quad (6)$$

This curve has been nondimensionalized with respect to the product of the melt specific heat and the overall temperature difference. The latent heat is thus nondimensionalized by the Stefan number ( $c_{pl} \Delta T / \Delta H$ ).

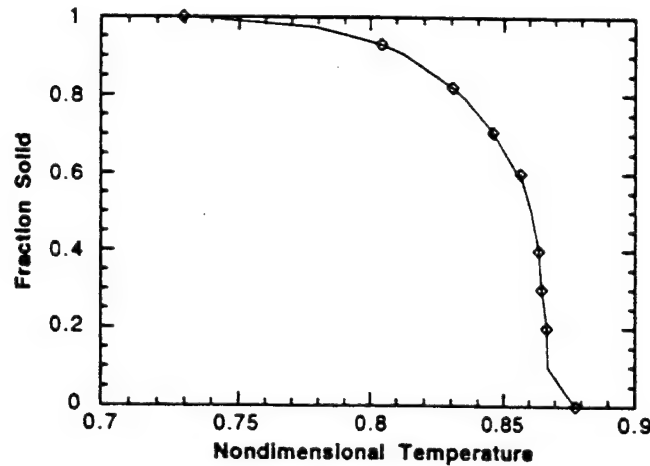


Figure 2. Fraction Solid vs. Nondimensional Temperature at a Rayleigh Number of  $4.5E+8$

The viscosity values in the fully molten region used were typical for nickel-based superalloys[20]. Between the fully molten region and the fully solid region, the permeability utilized in the computational model must rapidly decrease to values sufficient to completely suppress all fluid motion. Several investigators have measured effective viscosity values of semisolid slurries[21,22,23] and found that effective viscosity values for equiaxed microstructures increase rapidly at solid fractions of 0.4-0.6 for a wide range of shear rates. Bhat *et al.*[24] and Ganesan *et al.*[25] have numerically calculated permeability data for cross flow through columnar dendritic microstructures ( $K_T$ ) obtained experimentally for different solid fractions and numerically estimated the flow parallel to the primary dendrite arms ( $K_L$ ). These researchers provide recommendations of cross-flow and parallel-flow permeability as a function of solid fraction and show that the permeability rapidly decreases at solid fractions of 0.4-0.6, similar to the viscosity results. In this work, the decrease in convective ability in the mushy zone was simulated by a decreasing permeability, using the values obtained by Ganesan[25] and Bhat[24]. They found that the parallel flow permeability values are consistently higher than the cross flow values which is expected for columnar growth.

The present problem considers the heat transfer that takes place through the ampoule walls of finite thickness. This equation is presented only in its nondimensional form.

Energy Equation for Crucible Wall:

$$Pe \frac{\partial \theta}{\partial z^*} = \frac{\alpha_c}{\alpha_m} \left( \frac{1}{r^*} \frac{\partial}{\partial r^*} \left( r^* \frac{\partial \theta}{\partial r^*} \right) + \frac{\partial^2 \theta}{\partial z^{*2}} \right) \quad (7)$$

Here,  $Pe$  is the Peclet number ( $v_g L / \alpha_m$ ) representing the nondimensionalized growth rate ( $v_g$  is the growth velocity), and  $\alpha_c$  is the thermal diffusivity of the crucible.

A schematic diagram of the computational model is shown in Figure 3. Since the anticipated flows are assumed to be axisymmetric, the modeled region extends radially from the centerline to the outer edge of the crucible wall. Because it is assumed that the model is quite long in the axial direction, the end effects are neglected. Therefore, the top of the melt is kept at the hot zone temperature and the bottom of the crystal is at the cold zone temperature. The effect of the pull rate is considered by supplying melt at a uniform rate on top and extracting the solidified crystal at a rate equal to the growth rate modified by density differences. At the outer edge of the crucible wall, a temperature boundary condition representative of the radiation and convection characteristics from the crucible wall to the furnace enclosure is imposed. The nondimensional parameters of the growth material, crucible, and furnace conditions are listed in Table 1.

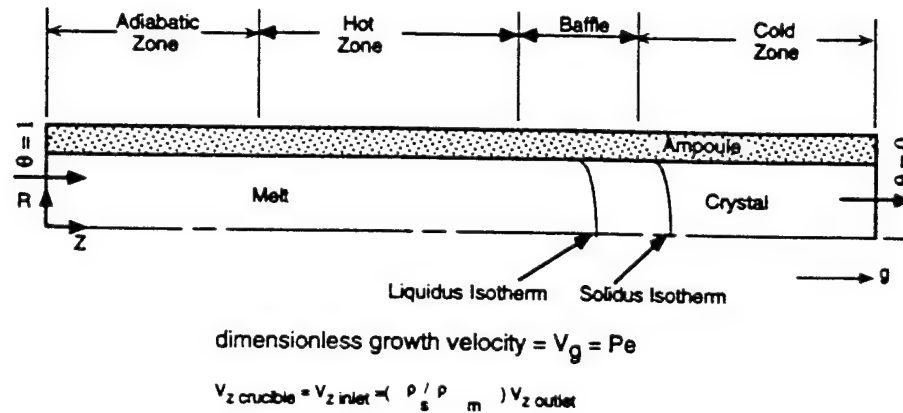


Figure 3. Schematic Diagram of the Extended Length Directional Solidification Model utilized in this study.

### III. Solution Methods

FIDAP, a finite-element-based, commercial software package, has been used for this simulation. One of the advantages of FIDAP is its ability to handle problems involving heat and mass transfer and latent heat release. Thus, it is especially suited for problems such as this study. The finite element method has the ability to solve complex flow domains and difficult boundary conditions. The first step is to discretize the domain into a set of simply shaped, nine node quadrilateral elements. Along boundaries and surfaces where boundary conditions are to be applied three node quadrilateral elements are used. Within each element the dependent variables are represented as interpolated functions expressed in terms of the values at elemental nodal points. The partial differential equations governing the fluid flow are then replaced by algebraic equations in each element using the Galerkin method, a weighted residual technique. The resulting algebraic equations are solved using the Newton-Raphson method under two convergence criteria to determine the values of the dependent variables throughout the domain. The first criteria is used for the solution vector and the second applies to the

residual vector. Both criteria in this simulation were set to 0.01%. A solution is obtained when all the variables to be solved meet both convergence criteria.

In the absence of a top adiabatic zone, the model leads to numerical instabilities when either the diameter is increased or the Rayleigh number is increased beyond approximately  $10^6$ . Under these conditions, the upper flow cell increases in both size and intensity. As it approaches the inlet, the strong convection interferes with the ability of the code to enforce the inlet boundary condition.

In order to alleviate these difficulties in the simulation of large diameter crystal growth, the model shown in Figure 3 was used. In Figure 3, an additional adiabatic zone is placed on top of the hot zone. With this geometry, the conditions of the melt inlet are now displaced upwards to the top of the adiabatic zone. This extra length allows the convective streamline cell that forms between the adiabatic zones to grow. Since there is very little change in temperature between the melt inlet and the bottom of the adiabatic zone, the possibility of convective cells forming in this region is quite small. Thus, this extended length model ensures that the upper convective cell will not distort the inlet flow. The extended length model presented here is similar to that used in a previous study [13]. The earlier study, however, considered the solute segregation due to the thermal buoyancy convection and solid-liquid interface deformation of gallium doped germanium (no mushy zone effects were considered). The results of that study compared well with a similar quasi-steady state model of the Bridgman process used by Adornato and Brown[26] which examined the effect of various parameters on solute segregation in the melt. Also, the use of the current set of equations gives excellent agreement with the model results given by Voller and Prakash[27].

The temperature boundary conditions applied to the edge of the crucible were determined from a separate set of simulation experiments using the commercial finite element code ProCast. Simulations of actual laboratory directional solidification experiments were performed and compared with embedded thermocouple data to determine transient crucible edge temperatures [28]. The thermal boundary conditions thus obtained are shown in Figure 4.

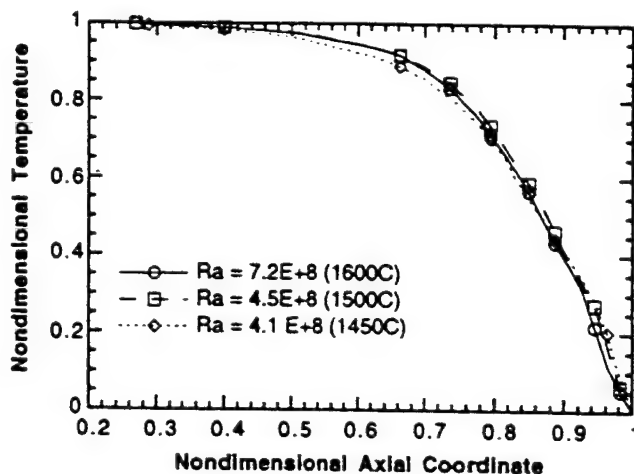


Figure 4. Thermal Boundary Conditions Determined from Thermocouple - Validated ProCast Simulations for the Rayleigh Numbers (Furnace Temperatures as shown)

#### IV. Results and Discussion

The primary purpose of this study is to assess the effects of various solidification process parameters (solidification velocity and crucible diameter) in enabling penetration of bulk convection into the mushy zone. The greater the penetration, the greater is the interaction

of the bulk convection with the lower density interdendritic liquid. Coupling of the thermosolutal buoyancy effects in the mushy zone with the bulk convection effects is neglected due to lack of information on solute partitioning and solutal effects on density. It is the radial component of velocity that causes the circular motion of the fluid into the mushy zone across the dendrites (see Figure 1b). The amount of penetration can thus be quantified by evaluating the nondimensional radial velocity adjacent to the mushy zone. In this paper, the radial velocity at the nondimensional liquidus temperature is the principal figure of merit used to assess convective penetration into the mushy zone.

Typical results for the extended length model are shown in Figure 5 where the effects of solidification velocity are examined for a Rayleigh number of  $4.5 \times 10^8$ . Since axisymmetric flows were assumed, only half of the cells bounded by the centerline and the crucible are shown. The microstructural data by Overfelt[16] and by McLean[29] show that for a constant temperature gradient, increases in the solidification velocity increase the cooling rate and result in a decrease in the primary dendrite arm spacing. This reduction in spacing decreases the tendency for freckles to occur[7]. Figures 5a-5c show the predicted steady state streamlines for Peclet numbers of 0.15, 1.50, and 3.00 (solidification velocities of 0.0005 cm/sec, 0.005 cm/sec, and 0.01 cm/sec). In addition the nondimensional liquidus and solidus isotherms are shown in each case. Increasing the Peclet number decreases the magnitude of the convection cells, especially the upper cell. Inspection of the predicted position of the mushy zone shows that the equilibrium position moves downward in the pulling direction as the steady-state velocity is increased, as expected. The change in mushy zone position also decreases the penetration of the lower convection cell into the mushy zone. Thus the model predicts that increasing the Peclet number will decrease both the magnitude of the convection cells as well as their penetration into the mushy zone. These results thus indicate a decrease in the potential for freckle forming buoyant plumes as a casting's cooling rate is increased, in agreement with solidification results of Copley *et al.*[2] and Pollock *et al.*[7].

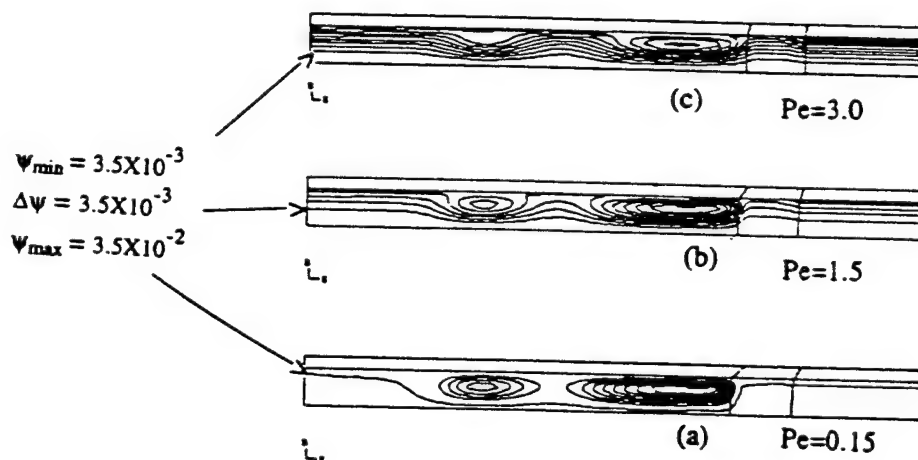


Figure 5. Predicted Steady State Streamlines for a Rayleigh Number of  $4.5 \times 10^8$  (1500 °C) and Peclet Numbers of (a) 0.15, (b) 1.5, and (c) 3.0 (Solidification velocities of 0.0005 cm/s, 0.005 cm/s and 0.01 cm/s). All arrows point to the minimum streamline value.

Figure 6 shows the nondimensional radial velocity at the liquidus for a Rayleigh number of  $4.5 \times 10^8$  and a range of Peclet numbers. The values of the nondimensional velocity are most significant in the upper part of the mushy zone which agrees with the results from Heinrich[10] and Felicelli[11]. The nondimensional radial velocity increases from zero at the centerline to a maximum at a nondimensional radial coordinate of 0.03 and drops back to zero at the no-slip crucible wall. Increasing the Peclet number is predicted to decrease the radial component of velocity at the liquidus temperature at all radial positions. The maximum



nondimensional radial velocity at the liquidus temperature is predicted to decrease from 5 at a Peclet number of 0.15 to 1.9 at a Peclet number of 3.00. These results are in agreement with the predicted streamlines shown in Figure 5.

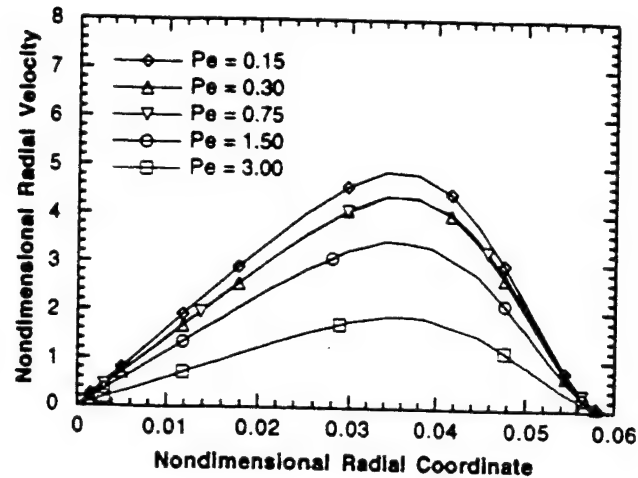


Figure 6. Nondimensional Radial Velocity at the liquidus temperature for a Rayleigh number of  $4.5 \times 10^8$  ( $1500^\circ\text{C}$ ) and the Peclet numbers indicated

The effect of crucible diameter at a Peclet number of 0.75 and Rayleigh numbers of  $7.2 \times 10^8$  and  $4.5 \times 10^8$  is shown in Figure 7. These two Rayleigh numbers produce average thermal gradients of  $90$  and  $50^\circ\text{C}/\text{cm}$  in the samples, respectively. The beneficial effect on the nondimensional radial velocity due to decreasing the Rayleigh number, i.e., hot zone temperature or thermal gradient, is relatively minor. The maximum nondimensional radial velocity only decreases from  $4.2$  to  $3.4$  when the Rayleigh number decreases from  $7.2 \times 10^8$  to

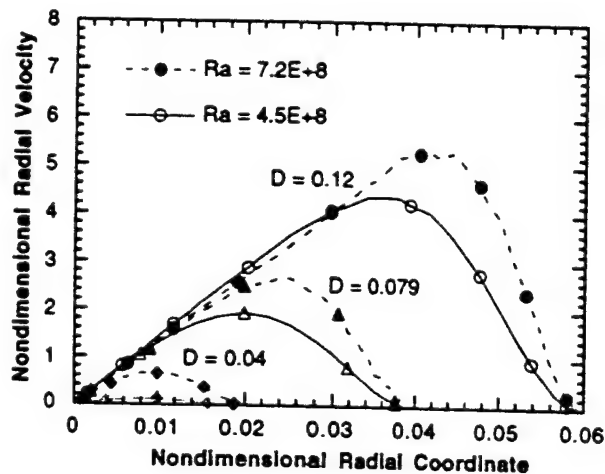


Figure 7. Nondimensional Radial Velocity at the Liquidus Temperature for a Peclet Number of  $0.75$  (solidification velocity of  $0.0025 \text{ cm/sec}$ ) and the Rayleigh Numbers and Crucible Diameters Indicated.

$4.5 \times 10^8$  (hot zone decreases from  $1600^\circ\text{C}$  to  $1500^\circ\text{C}$ ). However, decreasing the crucible diameter from 0.12 to 0.040 decreases the maximum nondimensional radial velocity from 6.1 to 0.1 when the Rayleigh number is  $7.2 \times 10^8$  (hot zone:  $1600^\circ\text{C}$ ). A decrease in radial velocity by a factor of 61 is predicted when the crucible diameter decreases by a factor of 3. Thus the model predicts that decreasing the crucible diameter will decrease the magnitude of the convection cells and their penetration into the mushy zone which indicate a decrease in the potential for freckle forming buoyant plumes. Heinrich [10] also showed the benefits associated with a small diameter casting. His model for a Pb-10%Sn alloy predicted that for a 1.5 mm crucible diameter the bulk fluid motion stabilized and all convection was avoided and thus no freckles could occur. This result also agrees with the investment casting foundry experience that thin wall castings are much less susceptible to freckle defects [30].

## V. Conclusions

An axisymmetric heat and mass transfer model of directional solidification of a typical nickel-based superalloy has been developed. Dimensionless forms of the governing equations were utilized for the computations, which were performed for a number of cases where the Rayleigh number, Peclet number, and crucible diameter have been parametrically varied. The following conclusions can be drawn from the results of the simulations:

(1) Increasing the Peclet number (or solidification velocity) lowers the position of the mushy zone and decreases the magnitude of the bulk convection. This decreases the penetration of bulk convection into the mushy zone which should decrease the potential for freckle forming plumes, consistent with previous experimental results.

(2) Decreasing the crucible diameter significantly decreases the overall convection, including the bulk convection that has penetrated into the mushy zone. This also decreases the potential for freckle formation. This is consistent with previous results and investment foundry experience.

## Acknowledgments

The authors gratefully acknowledge the financial support from NASA's Office of Space Access and Technology under Grant No. NAGW-1192 and Howmet Corporation, Whitehall, MI. In addition, technical discussions with Boyd Mueller of Howmet Corporation, Larry Graham of PCC Airfoils, Inc., and Tony Giamei of United Technologies Research Center were especially helpful.

## References

1. A.F. Giamei, and B.H. Kear, "On the Nature of Freckles in Nickel Base Superalloys," *Met. Trans.*, Vol. 1(1970) 2185-2191.
2. S.M. Copley et al., "The Origin of Freckles in Unidirectionally Solidified Castings", *Met. Trans.*, Vol 1(1970) 2193-2204.
3. A. Hellawell, "The Grain Structure of Castings: Some Aspects of Modeling," in *Modeling of Casting, Welding and Advanced Solidification Processes VII*, Mark Cross and John Campbell, Eds. (TMS, Warrendale, PA, 1995) 565-576.
4. A.K. Sample, A. Hellawell, "The Mechanisms of Formation and Prevention of Channel Segregation during Alloy Solidification," *Met. Trans.*, Vol. 15A (1984) 2163-2173.
5. T.D. McCay, and M.H. McCay, "Experimental Measurement of Solutal Layers in Unidirectional Solidification", *Journal of Thermophysics*, Vol. 2 (July 1988) 197.
6. J.R. Sarazin, and A. Hellawell, "Channel Formation in Pb-Sn, Pb-Sb, and Pb-Sn-Sb Alloy Ingots and Comparison with the System  $\text{NH}_4\text{Cl-H}_2\text{O}$ ", *Met. Trans.*, Vol. 19A(1988) 1861-71.
7. T.M. Pollock et al., "Grain Defect Formation during Directional Solidification of Nickel Base Single Crystals," in *Superalloys 1992*, Eds. S.D. Antolovich, R.W. Stusrud, R.A. Mackay, D.L. Anton, T. Khan, R.D. Kissinger, and D.L. Klarstrom, (TMS, Warrendale, Pa 1993) 125-134.
8. Muller, G., *Crystals: Growth, Properties, and Applications*, 12, (Berlin, Springer-Verlag)

9. M.H. McCay, T.D. McCay, and J.A. Hopkins, "The Nature and Influence of Convection on the Directional Dendritic Solidification of a Metal Alloy Analog,  $\text{NH}_4\text{Cl}$  and  $\text{H}_2\text{O}$ ", Metall. Trans., 24B (August 1993) 669.
10. J.C. Heinrich et al., "Thermosolutal Convection during Dendritic Solidification of Alloys: Part II. Nonlinear Convection," Met. Trans., 20B(1989) 883-891.
11. S.D. Felicelli, J.C. Heinrich, and D.R. Poirer, "Simulation of Freckles during Vertical Solidification of Binary Alloys", Met. Trans., 22B(December 1991) 847.
12. S. Motakef, "Interference of Buoyancy-Induced Convection With Segregation During Directional Solidification: Scaling Laws", Journal of Crystal Growth, 102 (1990) 197-213.
13. V. Sahai, J. W. Williamson, and R.A. Overfelt, "Controlling Convection and Segregation by Using Baffles in Bridgman Growth of Large Diameter Crystals at Low Gravity," in Heat Transfer in Microgravity Systems, Edited by S.S. Sadhal and A. Hashemi, ASME, HTD-Volume 235(1993) 1-10.
14. R.A. Overfelt et al., "Microstructure and Grain Defect Formation in Superalloys", (proprietary report, Space Power Institute, Auburn Univ. 1995).
15. R. J. Su, W. A. Jemian, and R.A. Overfelt, "Transient Effects In The Directional Solidification Of Al-Cu Alloys", to be published in Journal of Crystal Growth.
16. R.A. Overfelt et al. "Solidification Map of Directionally Solidified Inconel 718", Microstructural Science, Vol. 22.
17. C.A. Wang, Crystal Growth and Segregation in a Vertical Bridgman Configuration, (Ph.D. Thesis, Massachusetts Institute of Technology, 1984).
18. R.E. Taylor, private communication, Thermophysical Properties Research Laboratory, Inc., W. Lafayette, IN, 1995.
19. L. Backerud, G. Chai, and J. Tamminen, Solidification Characteristics of Aluminum Alloys, Vol. 2: Foundry Alloys, (AFS/Skanaluminium, Des Plaines, IL 1990)2-15.
20. R.A. Overfelt, C.A. Matlock, and M.E. Wells, "Viscosity of Superalloy 718 by the Oscillating Vessel Technique," submitted to Materials and Metallurgical Transactions: B.
21. D.B. Spencer, R. Mehrabian, and M.C. Flemings, Met. Trans., 3 (1972) 1925-1932.
22. V. Laxmanan, and M.C. Flemings, Metall. Trans., 11A (1980)1927-1937.
23. H. K. Moon, (Ph.D. Thesis, Massachusetts Institute of Technology, 1990).
24. M.S. Bhat, D.R. Poirier, and J.C. Heinrich, "Permeability for Cross Flow through Columnar-Dendritic Alloys," Metall. and Materials Trans., Vol. 26B(1995) 1049-1056.
25. S. Ganesan, C.L. Chan, and D.R. Poirer, "Permeability for Flow Parallel to Dendrite Arms", Materials Science and Engineering, Vol. A151(1992) 97-105.
26. P.M. Adornato, and R.A. Brown, "Convection and Segregation in Directional Solidification of Dilute and Non-Dilute Binary Alloys: Effect of Ampoule and Furnace Design", J. Crystal Growth, 80 (1987) 155-190.
27. V.R. Voller, and C. Prakash, "A Fixed Grid Numerical Modeling Methodology for Convection-Diffusion Mushy Region Phase-Change Problems," International Journal of Heat and Mass Transfer, Vol. 30, (1987) 1709-1719.
28. V. Sahai, P. Banerjee, and R.A. Overfelt, unpublished research 1995.
29. M. McLean, Directionally Solidified Materials for High Temperature Service, (London, The Metals Society, 1983).
30. B. Mueller, private communication, HOWMET Corporation, Whitehall, MI, 1995.

DETC99/CIE-XXXX

## Two-Dimensional Combined Radiation and Conduction Transient Heat Transfer in Directional Solidification

Deming Wang  
Space Power Institute  
Auburn University, Auburn, AL 36849

Harry S. Whitesell  
Mechanical Engineering Department  
Auburn University, Auburn, AL 36849

Tony Overfelt  
Mechanical Engineering Department  
Auburn University, Auburn, AL 36849

### Abstract

This paper presents a computer-aided heat transfer simulation method to predict the thermal characteristics of an alloy sample in a special furnace for directional solidification. A two-dimensional transient heat transfer by radiation combined with conduction is developed to calculate the energy exchange between the symmetric furnace and the sample. Two kinds of control volumes are used to obtain a set of highly efficient finite difference equations for heat conduction and heat radiation with changeable view factors. The simulation results are verified by measurable experimental results. Using the two-dimensional computer simulation model, many thermal properties of the samples can be obtained, such as temperature distribution, solidification velocity, the shapes and positions of the liquid/solid interface and thermal gradient at the interfaces. These are very important to analyze microstructure of casting alloy, avoid casting defects and control casting quality.

### Nomenclature

$A_k$  = small area of a radiative surface  $k$  ( $\text{cm}^2$ )  
 $T$  = temperature ( $^{\circ}\text{C}$ )  
 $T_s$  = critical temperature of solid, during solidification ( $^{\circ}\text{C}$ )  
 $T_l$  = critical temperature of liquid, during solidification ( $^{\circ}\text{C}$ )  
 $t$  = time (sec)  
 $k$  = thermal conductivity  
 $\rho$  = density of mass ( $\text{kg}/\text{cm}^3$ )  
 $c_p$  = heat capacity

$r$  = radial dimension (m)  
 $z$  = axial dimension (m)  
 $r_n$  = radius of an inner side of a control volume (m)  
 $r_s$  = radius of an outer side of a control volume (m)  
 $r_x$  = radius of the center of a control volume (m)  
 $F_{k-j}$  = view factor from radiative surfaces  $k$  to  $j$   
 $q$  = radiative heat flux ( $\text{W}/\text{m}^2$ )  
 $q_o$  = outgoing radiative heat energy ( $\text{W}/\text{m}^2$ )  
 $\theta_i$  = a view angle  
 $S_b$  = the rate of heat generation per unit volume  
 $\sigma$  = Stefan-Boltzmann constant,  $5.668 \times 10^{-12}$  ( $\text{W}/\text{cm}^2 \cdot \text{K}^4$ )  
 $S_x$  = distance along direction of radiative propagation (m)  
 $v$  = traversing velocity of a sample relative to the furnace, (m/s)  
 $N$  = number of radiative surfaces of finite control volumes  
 $\epsilon_i$  = emissivity of the surface  $i$   
 $\delta_{kj}$  = Kronecker delta  
 $\Delta r$  = dimension of a finite volume in radial direction (m)  
 $\Delta z$  = dimension of a finite volume in axial direction (m)

### 1 Introduction

In directional solidification (DS) processing of castings, the temperature distribution, isothermal surfaces, thermal gradient in the mushy (pasty) zone and solidification rates are very important. These variables affect the orientation and amount of dendrites, shapes of grains, solute segregation and deleterious casting defects, such as microporosity, freckles and segregation channels. In order to avoid the casting defects, the temperature distribution

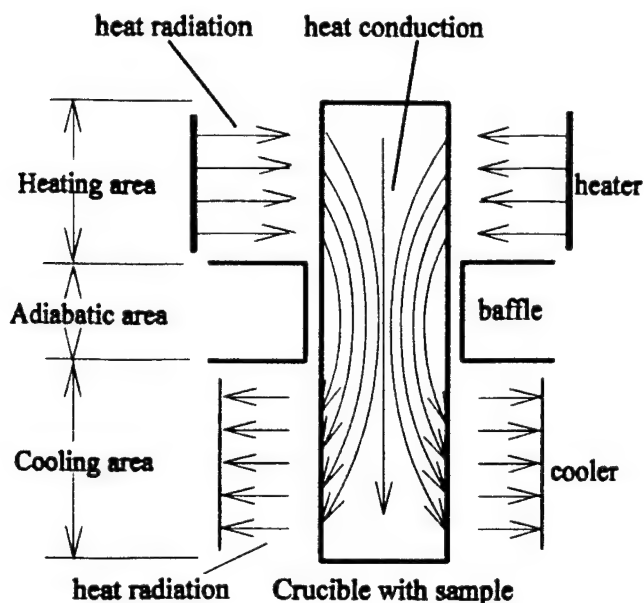


**Fig.1 Heat flux on a casting sample in a DS furnace**

factors to influence the microstructure and the casting quality. and thermal gradients of castings during directional solidification must be strictly controlled. However, the structure of furnaces used for directional solidification are often complex. The temperature distribution within the casting not only depends on furnace temperature but also on the thermal properties of the casting alloy, crucibles, retorts etc. An accurate heat transfer analysis model is needed.

Generally, directional solidification is induced by withdrawing a casting alloy from a furnace through an insulated region of high thermal gradient and into a cooling region. These three areas are called heating, adiabatic and cooling areas (see Fig. 1). A baffle is used to isolate the hot and cool areas and also used to keep the

isothermal surfaces in the freezing zone of the casting alloy flat.

During directional solidification the casting can also be divided into three zones dependent on the states of material: liquid zone, mushy zone (liquid+solid zone) and solid zone (see Fig. 2). The interfaces between these three zones can be determined by the phase diagram of an alloy or by experimental determination of the critical temperatures of an alloy. The isothermal surfaces in the sample have different shapes, convex, planar, concave, depending on which zone the sample is located.

When a sample is at a stationary position in a DS furnace, the heat transfer will approach equilibrium. When designed properly, the mushy zone will be fixed in the baffle area of the furnace. An ideal case is when the mushy zone of the sample is fixed in the adiabatic area and the mushy zone isotherms can be kept flat. When the sample moves in the direction from the heating area of the furnace to the cooling area, the mushy zone antiparallel relative relating to the sample. The mushy zone velocity is called the solidification velocity. In the DS process, the solidification velocity does not necessarily equal the moving velocity of the sample. If the solidification velocity is smaller than the velocity of the sample, the mushy zone will leave its original position in the baffle area and move to the cool area. The interface will also assume a concave shape.

Heat transfer in actual furnaces is quite complex. Many investigators insert thermocouples into the casting alloy to measure the temperature distribution and thermal gradients. Clyne [1] did an experimental investigation of the thermal characteristics. The experiment revealed the velocity of the advancing interface may be significantly greater than the crucible traverse velocity due to thermal diffusions of samples. The experiment also showed the furnace thermal field is very sensitive to the temperature gradient of the sample and the heat divergence between the sample and environment. Overfelt's experiment showed that the different traverse velocities effect the growth of dendrites in axial and radial directions [2]. When the traverse velocity is low, the radial temperature gradient is quite small. A columnar dendritic microstructure well aligned with traverse direction. Route [3] did some experiments to display the shape of the melt/solid interface by an autoradiographic experimental method. The experiment showed that furnace end effects can be a dominant factor in Bridgman systems, and can cause significant differences between imposed and actual growth rates. However, the traditional experimental methods are expensive, give only limited measurement data due to experimental conditions and geometry constraints.

Computer models have been considered as a best way to predict the temperature distribution and thermal gradient. During the past two decade, one-dimensional heat transfer models have been widely used. At the early of 1980's, two typical kinds of analytic models were proposed by Naumann and Jasinski respectively [4-6]. They developed a one-dimensional analytical description of axial heat flow in a translating rod that is applicable for Biot number. Their models can accommodate different properties of the sample in the solid and molten state, different heat transfer coefficients in the hot and cold zones, finite length effects in one zone, and approximate ampule effects by adjusting the Biot numbers to account for heat transfer in the ampule.

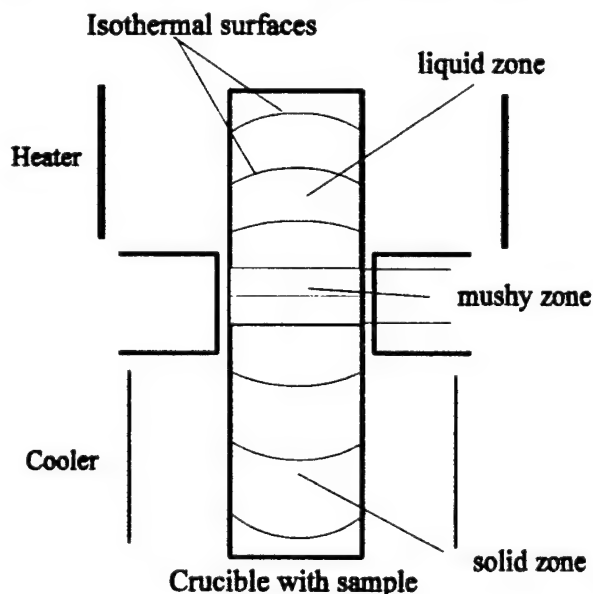


**Fig.2 Isothermal surfaces in the casting sample for DS**



Unfortunately, these models cannot predict temperature gradients in the radial direction. Another disadvantage is the Biot number parameter for the sample has to be estimated, it is often a difficult task. The temperature distribution of the sample is very sensitive to this parameter.

Recently, two dimensional heat transfer models have been proposed for symmetric directional solidification furnace sets [7]; these models provide more information, e.g., the temperature distribution, thermal gradient in axial and radial directions and liquid/solid interface shapes of directionally solidified alloys. The boundary conditions at the side wall are typically given as a linear function of the temperature gradient. Because heat transfer between sample and heater/cooler is quite complex, we cannot accurately estimate or simply elucidate them. A more accurate model is employed by Bartholomew and Hellawell [8]. Two kinds of heat transfer forms, heat conduction and radiation, were used to calculate energy change between heater/cooler and casting alloy.

A quite good heat transfer model in a whole DS furnace system was proposed by Hong [9-10], which includes the encapsulated fluid between the heater and the ampule, conjugate heat transfer around and within the sample, and phase change dynamics between melt and crystal. However, Hong's model does not calculate the heat radiation in detail. In addition, reflective radiation is neglected in his finite element method.

The contribution of this paper is to provide a simple and efficient numerical calculation method to evaluate heat transfer in an axisymmetric DS furnace. Finite difference equations with control volume method are used to calculate two-dimensional transient heat transfer, which includes heat conduction and heat radiation. Two different kinds of finite control volumes are respectively used for heat conduction and heat radiations. A net-radiation method with changeable view factors is used during DS process as casting sample moves out of the furnace chamber.

## 2 Numerical Model for Heat Conduction and Radiation

The heat transfer in the solidification process is very complex, including conduction, radiation and convection. In order to make the problem tractable, for our small diameter sample, we simplify the system governing equations by considering the temperature field in the absence of buoyant convection in small diameter samples. An axisymmetric furnace for directional solidification can be simplified as in figure 3. The system temperature control equations will be developed in following sections.

### 2.1 Temperature governing equations

Combined conduction and radiation heat transfer is considered as a main energy transfer in the furnace for directional solidification. A two dimensional temperature governing equation in symmetric cylindrical coordinates is derived from the basic laws of energy conservation:

$$\frac{\partial T}{\partial t} - \frac{k}{\rho c_p} \left( \frac{1}{r} \frac{\partial T}{\partial r} + \frac{\partial^2 T}{\partial r^2} + \frac{\partial^2 T}{\partial z^2} \right) = \frac{S_h}{\rho c_p} + \frac{1}{\rho c_p} \left( \frac{\partial q}{\partial r} + \frac{\partial q}{\partial z} \right) \quad (1)$$

where  $S_h$  is the rate of heat generation per unit volume, such as latent heat released solidification. The radiative flux  $q$  is also an

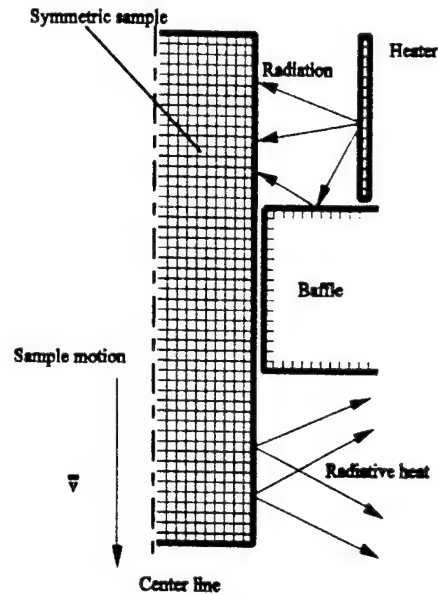


Fig.3 Heat transfer grid model for DS

unknown variable, which will apply on the surface of a body by heat radiation when the sample is heated or cooled.

Heat radiation in a furnace can be considered as another form of heat transfer inside the enclosure. The radiation flux leaves a surface, travels to the other surfaces, is partially reflected, and is then re-reflected many times within the enclosure with partial absorptions at each contact with a surface. It would be very time consuming to follow the beams of radiation as they undergo this process. Fortunately, it is not necessary to do this. An analysis can be formulated in a convenient manner by using the net-radiation method [11]. Two basic heat balance equations can be obtained:

$$q_k = \frac{\epsilon_k}{1 - \epsilon_k} (\sigma T_k^4 - q_{o,k}) \quad (2)$$

$$q_k = q_{o,k} - \sum_{j=1}^N F_{k-j}(t) q_{o,j} \quad (3)$$

where  $F_{k-j}(t)$  is a view factor from  $k$  to  $j$ , which can be obtained by

$$F_{k-j}(t) = \frac{1}{A_k} \int_{A_k} \int_{A_j} \frac{\cos \theta_j(t) \cos \theta_k(t)}{\pi S_{jk}^2} dA_k dA_j \quad (4)$$

When the sample continuously moves with time, the view factor is a function of time (see Fig. 4).

The temperature distribution on the sample/crucible can be obtained from equations (1)-(4). But these are very nonlinear partial differential equations, the exact solutions are difficult to be obtained. Many numerical methods can be used to solve the 2D transient thermal transfer equations, such as finite difference equations, finite element analysis, and etc.

### 2.2 Finite difference equations with control volume

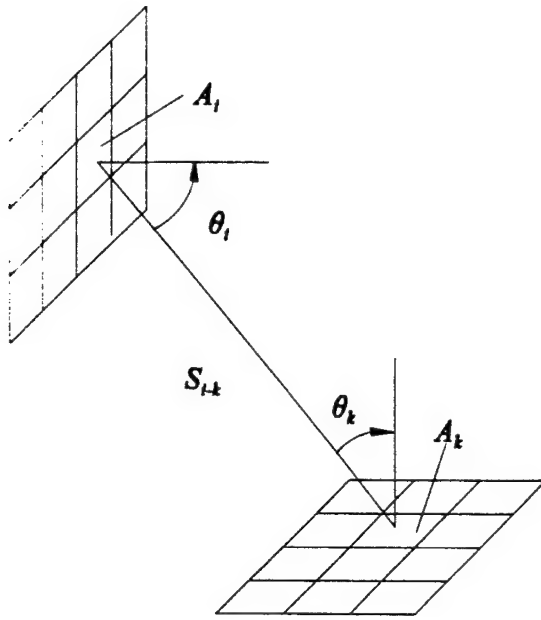


Fig. 4 Geometry for a view factor between radiative surfaces of finite control volume

Finite difference equations with the control volume have been widely used to solve the temperature control equations of heat conduction problems [12]. Here we extend the method to solve the equations of heat conduction combined with radiation. Two kinds of control volumes are used in different calculation domains; one is a calculation domain with heat conduction, and another is for a calculation domain with heat conduction and radiation. For the first problem, a two-dimensional control volume is used, so we can get two-dimensional temperature distribution in the sample and determine the shapes of isothermal surfaces within the mushy zone. And for the second problem, a one-dimensional control volume is used, which tremendously simplifies temperature control equation for heat conduction combined with heat radiation.

#### – 2D Control volume for heat conduction

We use a two-dimensional control volume for the calculation domain inside the sample, where we only consider heat conduction. Two-dimensional control volume means we consider heat transfer in two dimensions for a finite control volume because the calculation domain is a symmetric cylinder. The size of the cross section is  $\Delta r \times \Delta z$ . The centering the node P (pole), and let the upper-case letter E (east), W (west), N (north) and S (south) denote its neighboring nodes and  $(\delta z)_E$ ,  $(\delta z)_W$ ,  $(\delta r)_N$ ,  $(\delta r)_S$  denote the distances between the nodes (see Fig.5).

The temperature governing equation without radiative heat flux also can be expressed by an integration form for a small volume with a cross area  $\Delta z \times \Delta r$  within a small time duration  $\Delta t$ :

$$\frac{1}{\Delta t} \int_t^{t+\Delta t} \int_S \int_W^E r \frac{\partial T}{\partial t} dr dz dt$$

$$= -\frac{k}{\rho c_p} \frac{1}{\Delta t} \int_t^{t+\Delta t} \int_S \int_W^E \left[ \frac{1}{r} \frac{\partial T}{\partial r} + \frac{\partial^2 T}{\partial r^2} + \frac{\partial^2 T}{\partial z^2} \right] dr dz dt$$

$$= \frac{1}{\Delta t} \int_t^{t+\Delta t} \int_S \int_W^E S_h dr dz dt \quad (5)$$

where N, S, E and W respectively indicate four surfaces of the cross section of the small volume. For equation (5), the unsteady term may be discretized as:

$$\frac{1}{\Delta t} \int_t^{t+\Delta t} \int_S \int_W^E \frac{\partial T}{\partial t} dr dz dt = \frac{\Delta r \Delta z}{\Delta t} \left( \frac{r_n + r_s}{2} \right) (T_p - T_p^o) \quad (6)$$

The superscript "o" indicates the value at the old time  $t$ , whereas no superscript is assigned for the value at the new time  $t + \Delta t$ . The conduction-diffusion terms are integrated by using a fully implicit scheme in which only new time values are used for evaluation of the temperature.

$$\frac{k}{\rho c_p} \frac{1}{\Delta t} \int_t^{t+\Delta t} \int_S \int_W^E \left[ \frac{1}{r} \frac{\partial T}{\partial r} + \frac{\partial^2 T}{\partial r^2} + \frac{\partial^2 T}{\partial z^2} \right] dr dz dt$$

$$= \left\{ r \left( \alpha(T, r, z) \frac{\partial T}{\partial z} \right)_W^E \Delta r + r \left( \alpha(T, r, z) \frac{\partial T}{\partial r} \right)_S^N \Delta z \right\} \quad (7)$$

Integrate the source term, the right side term in Equ. (5), similarly as

$$\frac{1}{\Delta t} \int_t^{t+\Delta t} \int_S \int_W^E S_c(T_p) dx dy dt = S_c(T_p^o) \Delta r \Delta z \quad (8)$$

Thus we obtain the following general finite difference equation for the heat conduction:

$$a_p T_p = a_E T_E + a_W T_W + a_N T_N + a_S T_S + b \quad (9)$$

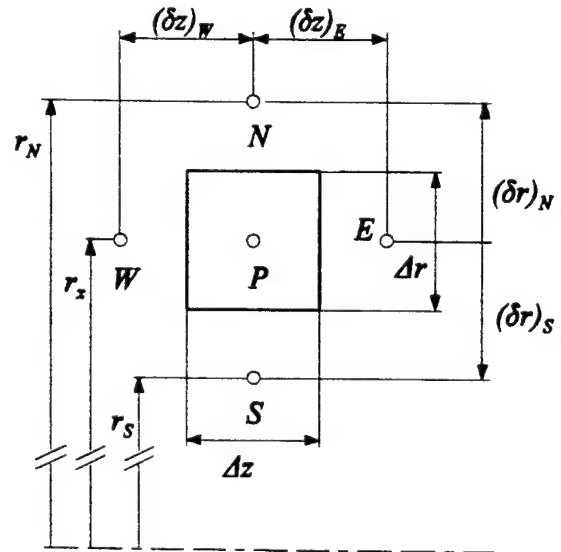


Fig. 5 Control volume for difference equations

where

$$a_E = \frac{\alpha_e(T, r, z) r_x \Delta r}{(\delta z)_e} \quad (9a)$$

$$a_W = \frac{\alpha_w(T, r, z) r_x \Delta r}{(\delta z)_w} \quad (9b)$$

$$a_N = \frac{\alpha_N(T, r, z) r_x \Delta r}{(\delta z)_N} \quad (9c)$$

$$a_S = \frac{\alpha_s(T, r, z) r_s \Delta r}{(\delta z)_s} \quad (9d)$$

$$a_P = \frac{\Delta x \Delta y r_x}{\Delta t} + a_E + a_W + a_N + a_S \quad (9e)$$

$$b = S_c(T_p^o) \Delta z \Delta r + \frac{r_x \Delta z \Delta r}{\Delta t} T_p^o \quad (9f)$$

and

$$r_x = \frac{r_n + r_s}{2} \quad (9g)$$

### 1D Control volume for heat conduction and radiation

For some calculation domains, such as surface boundaries of casting samples, heat will be applied on by radiation. So, the radiative flux  $q$  in Eq. (1) cannot be deleted. The radiative flux is a function of surface temperatures and radiative view angles. The system control equations are a set of nonlinear partial differential equations. In order to simplify the numerical calculation, we use one-dimensional control volume to handle the system temperature control equation (1) with heat conduction and radiation.

"1D Control volume" means that we only consider heat transfer as one dimension along the normal direction of the radiative surface. The numerical calculation error due to the one dimension simplification will be very small when the grids of the calculation domain are small. The one dimension control volume greatly simplifies system control equations for heat conduction combined with heat radiation. If the heat radiation applies on the west boundary control volume (see Fig. 5), a linear relationship for one dimension in  $x$  direction can be obtained between temperatures and radiative heat flux  $q$ :

$$T_p = T_w^o - q_k \frac{c_p \rho (\delta x)_w}{k} \quad (10)$$

Where  $q_k$  is a radiative heat flux, which can be solved by equations (2) - (3). When a radiative surface is comprised by many surfaces of small finite control volumes of a sample, each small surface can be considered as an isothermal area. Equations (3) and (4) can be rewritten as

$$q_k = \frac{\epsilon_k}{1 - \epsilon_k} (\sigma(T_k)^4 - q_{o,k}) \quad (11)$$

$$q_k = q_{o,k} - \sum_{j=1}^N F_{k-j}(t) q_{o,j} dA_k dA_j \quad (12)$$

where  $q_k$ ,  $T_k$  are heat flux and temperature in the radiative surface of a finite control volume. They are considered as constants.

### Changeable view factor during DS process

When the process of the directional solidification begins, the sample will move out of the furnace. The relative position between heat radiation surfaces will change with time. The view factors  $F_{k-j}(t)$  is a function of time. In order to get a numerical calculation, the view factor function also has to be discretized. The time duration depends on the casting sample moving speed and the width of the radiative surface of a finite control volume in the moving direction. The  $F_{k-j}^t$  is considered as a constant during  $\Delta t$ . The  $\Delta t$  can be calculated by the following equation:

$$\Delta t = \frac{\Delta z}{v} \quad (13)$$

Combining equations (11) and (12), the numerical linear algebraic equations can be derived as:

$$\frac{1}{\epsilon_j} q_k - \sum_{j=1}^N \frac{1 - \epsilon_j}{\epsilon_j} F_{k-j}^t q_j = \sigma(T_k^o)^4 - \sum_{j=1}^N F_{k-j}^t \sigma(T_j^o)^4 \quad (14)$$

or rewritten a compact form

$$[A][q] = [C](\sigma(T^o)^4) \quad (15)$$

where the element of  $[A]$  is

$$a_{ij} = \frac{\delta_{ij}}{\epsilon_i} - \frac{1 - \epsilon_i}{\epsilon_i} F_{i-j}^t \quad (16)$$

and the element of  $[C]$  is

$$c_{ij} = \delta_{ij} - F_{i-j}^t \quad (17)$$

where

$$\begin{aligned} \delta_{ii} &= 1, & i &= j \\ \delta_{ij} &= 0, & i &\neq j \end{aligned} \quad (18)$$

The view factor

$$F_{k-j}^t = \frac{\cos(\theta_k^t) \cos(\theta_j^t)}{\pi s_{k-j}^2} A_j \quad (19)$$

where  $\theta_k^t$  and  $\theta_j^t$  are directional angles of the radiative flow at  $k$  and  $j$  surfaces at time  $t_k$

Equation (15) is also a set of linear algebraic equations for the grid point values  $T$  and  $q_k$ . Solving the equations (15) and (10),

we can get a set of radiative heat  $q_k$  and  $T$  on the grid points of the 1D control volume.

### 3 Application

Using the above discussed simulation method, a computer simulation program, SIMUDS (computer-aided simulation of a furnace for directional solidification) has been developed by Auburn University. This program has been applied in a following experimental furnace for directional solidification. The calculation results are compared to some measured experimental results.

#### 3.1 Experimental setup and furnace device

The experimental setup for this study is illustrated schematically in Fig. 6. The sample chosen is the nickel-based superalloy Mar-M247 (Mar-M is a trademark of Martin Marietta Company). The superalloy bars were supplied by Howmet Corporation with a nominal composition (weight%) Al-5.7Co-10.1Cr-8.4W-10Ta-3.1. Each bar was approximately 20 cm long and 1.25 cm in diameter and was placed in high density alumina tubes with appropriate spacers to elevate the sample into the hot area of the furnace. To reduce oxidation, the entire sample is enclosed in an alumina retort that isolates the sample from the atmosphere. A vacuum is drawn in the retort and replaced with high purity argon gas. The entire sample assembly retort is connected to a linear drive system, which allows precise control of the withdrawal velocity during the directional solidification experiment.

The furnace has an asymmetric geometric structure, which consists of two heaters (a main heater and a booster heater. The main furnace (its height of the sample is 17.78 cm) is used to provide energy to melt the sample. The adiabatic zone (its height is 10.6 cm) is designed to produce flat isotherms. The booster furnace (its height is 17.78 cm) is used to extend and control the adiabatic zone. When directional solidification begins, the retort moves out of the furnace chamber, the bottom of the sample is cooled by surrounding air.

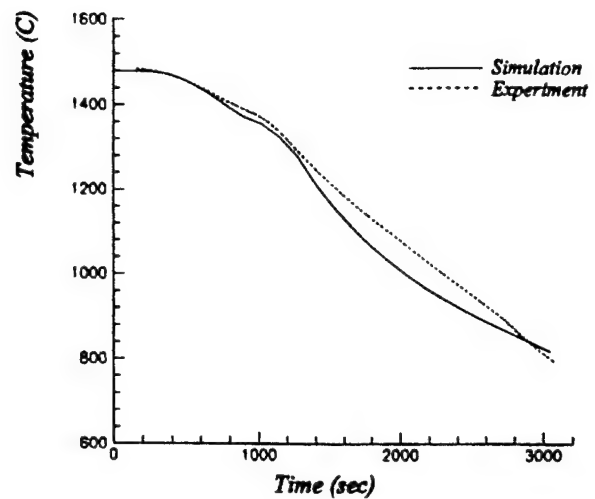


Fig. 7 Comparison of temperature at center middle of the sample

#### 3.2 Simulation results and analysis

The temperature of the main heater is defined at 1500°C, which is well above the liquidus temperature of the alloy. The temperature of the booster heater is controlled at 680°C. The withdraw velocity of the sample is set at 0.01 cm/s. Three thermocouples at fixed positions A, B and C (see Fig. 6) are used to record the temperature profile on the retort, crucible and inside the sample. These data are used to verify the simulation results from computer model. Figure 7 shows that the simulation result accurately matches the experimental data (Measuring position C, middle position inside sample). Similar agreement was also seen between the simulation results and thermocouple data at positions A and B.

From the computer simulation model, we can also obtain important other thermal properties during DS process. If we know the critical solidification temperature (such as  $T_s = 1276^\circ\text{C}$  and  $T_L = 1329^\circ\text{C}$  for Mar-M247), we can determine the interface positions of liquid/mushy zones and mushy/solid zones at every

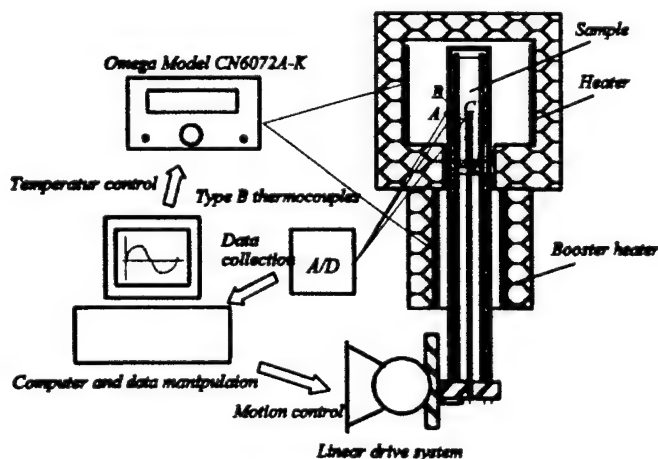


Fig. 6 A furnace and control set for directional solidification

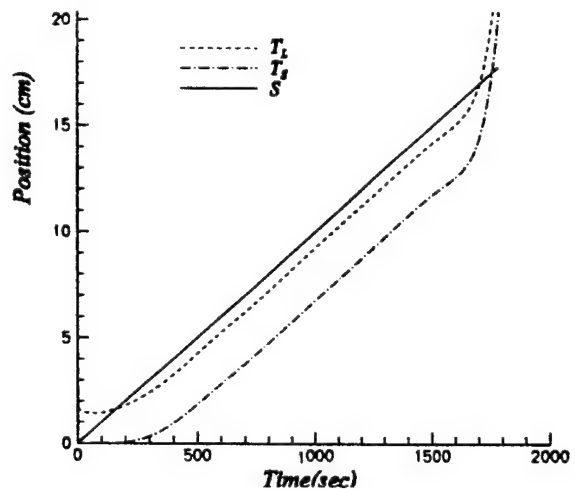


Fig. 8 Interface positions of the sample during DS

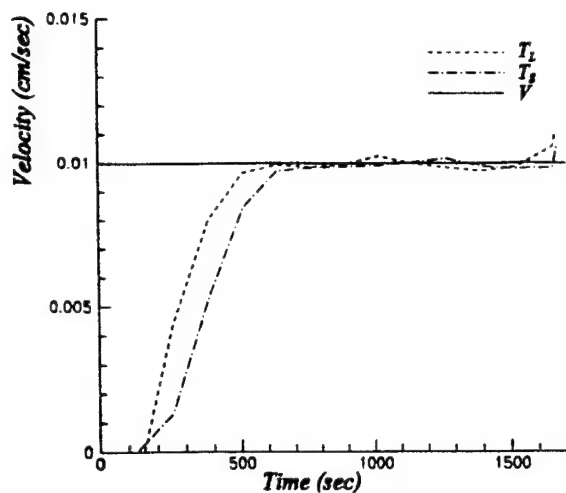


Fig. 9 Interface velocities of the sample during DS

instantaneous moment of solidification process. Fig. 8 and Fig. 9 show how the interface positions and velocities change with solidification time, where  $T_L$  and  $T_S$  express liquid/mushy interface and mushy/solid interface,  $S$  and  $V$  express the displacement and velocity of the sample. Isotherms from the simulation of the DS process are shown in Fig. 10. At the beginning ( $t=0$ ), the sample is almost completely melted. When solidification begins, the mushy zone move up with time. The shapes of the mushy zone interfaces also indicate that the radial thermal gradients are very small and crystal growth is predominantly along the axial direction. The height of mushy zone is constant when the two end effects are not concerned, which keeps the dendritic structure constant through the sample during the entire experiment.

Figures (11) and (12) show the axial and radial thermal gradients at  $T_S$  and  $T_L$  during the entire experiment. Such information is critical to interpret metallurgical microstructures in castings after solidification is complete.

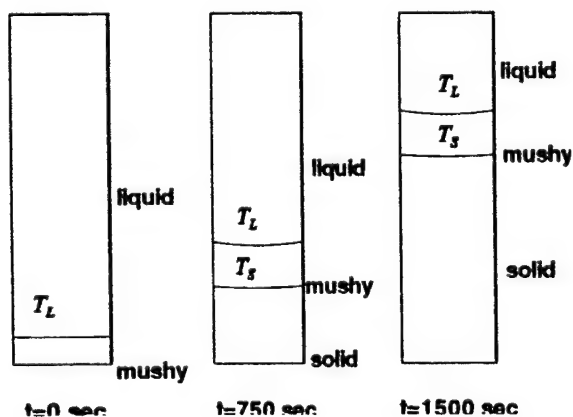


Fig. 10 DS simulation of castings

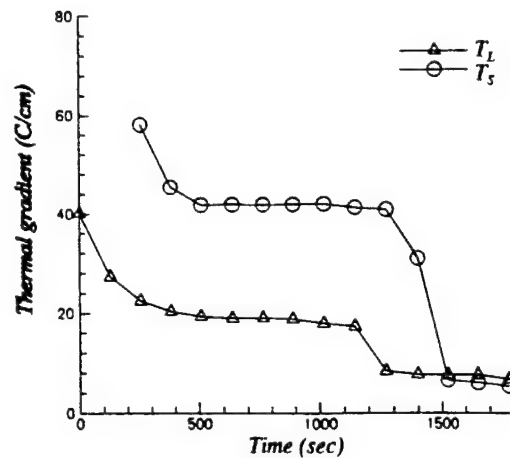


Fig. 11 Thermal gradients at interfaces in axial direction

#### 4 Conclusion

In a special furnace for directional solidification, two main heat transfer forms; radiation and conduction, can be considered to accurately calculate the temperature distribution in a casting sample during directional solidification. Finite difference equations with control volumes is a highly efficient method to solve system temperature control equations, which deal with heat conduction and radiation.

In order to increase calculation efficiency, we can use two different control volumes. One is 2D finite control volume, which is used for calculation domains containing heat conduction. Another is 1D finite control volume used for calculation domains containing heat conduction and radiation.

The simulation results are verified by experimental thermocouple data. Using the computer simulation results, many thermal properties of samples can be obtained, such as 2D temperature distribution, liquid/solid interface positions and shapes, solidification velocity, and 2D thermal gradients at interfaces.

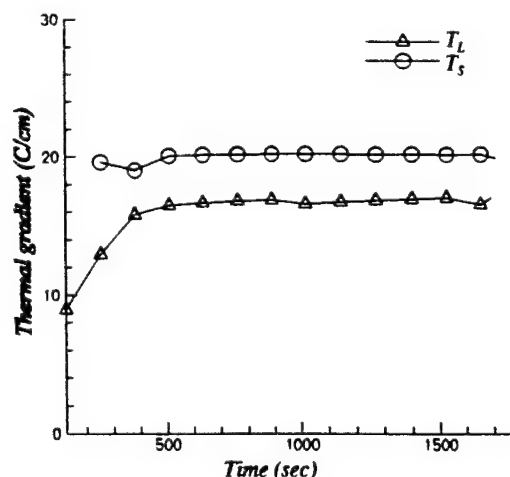


Fig. 12 Thermal gradients in interfaces in radial direction



## Acknowledgments

This material is based upon work supported by, or in part by, the U.S. Army Research Office under Grant DAAH04-96-1-0321 and NASA Marshall Space Flight Center under Cooperative Agreement NCC8-128.

## REFERENCES

- [1] T.W. Clyne, Heat Flow in Controlled Directional Solidification of Metals, *J. of Crystal Growth*, Vol. 50, pp.684-690, 1980.
- [2] R.A. Overfelt, C.A. Matlock, R.C. Wilcox, Comparison of the theory with experiment in one-directional analytical modeling of directional solidification, *J. of Crystal Growth*, Vol. 147, pp.403-407, 1995.
- [3] R.K. Route, M. Wolf and R.S. Feigelson, Interface Studies During Vertical Bridgman CdTe Crystal Growth, *J. of Crystal Growth*, Vol. 70, pp.379-385, 1984
- [4] R.J. Naumann, An Analytic Approach to Thermal Modeling of Bridgman-Type Crystal Growth, *J. of Crystal Growth*, Vol. 58, pp.554-568, 1982.
- [5] T. Jasinski and W.M. Rohsenow, Heat Transfer Analysis of The Bridgman-Stockbarger Configuration for Crystal Growth, *J. of Crystal Growth*, Vol. 61, pp.339-354, 1983.
- [6] T. Jasinski and R.J. Naumann, One-Dimensional Thermal Modeling of Vertical Bridgman-Type Crystal Growth, *J. of Crystal Growth*, Vol. 66, pp.469-471, 1984
- [7] Masatoshi Saitou and Akira Hirata, Numerical Calculation of Two-dimensional Unsteady Solidification Problem, *J. of Crystal Growth*, Vol. 113, pp.147-156, 1991
- [8] M.L. Bartholomew and A. Hellawell Changes of Growth Conditions in The Vertical Bridgman-Stockbarger Method for The Solidification of Aluminum. *J. of Crystal Growth*, Vol. 50, pp. 453-460, 1980.
- [9] Hong Ouyang and Wei Shyy, Multi-zone Simulation of the Bridgman Growth Process of  $\beta$ -NiAl Crystal, *Int. J. of Heat Mass Transfer*, Vol. 39, No. 10, pp. 2039-2051, 1996.
- [10] Hong Ouyang and Wei Shyy, Simulation and measurement of a vertical the Bridgman growth system for  $\beta$ -NiAl Crystal, *Int. J. of Heat Mass Transfer*, Vol. 40, No. 10, pp. 2293-2305, 1997
- [11] Robert Siegel, Thermal Radiation Heat Transfer, Hemisphere Publishing Corp., Washington, D.C., 1992.
- [12] Akira Nakayama, PC-Aided Numerical Heat Transfer and Convective Flow, CRC press, 1995
- [13] Patankar, S. V., Numerical Heat Transfer and Fluid Flow, Hemisphere Publishing Corp., Washington, D.C., 1980.

Table III. Raoultian Activity Coefficient of PbS (l),  $\gamma_{\text{PbS}}$ , in the  $\text{CuS}_{0.5}$ -CuS-PbS System Matte at 1533 K

$N_S$	$N_{\text{CuS}}$	$(p_{\text{S}_2})^{1/2}$ -ZL	$(p_{\text{S}_2})^{1/2}$ -SM	Mass Pct Pb	$a_{\text{Pb}}$	$p$ (PbS)	$p$ (Pb)	$p$ (Pb <sub>2</sub> )	$\gamma_{\text{PbS}}$
0.3437	0.0462	0.0285	0.1237	0.341	$9.93 \times 10^{-4}$	$19.9 \times 10^{-5}$	$3.4 \times 10^{-5}$	$9.5 \times 10^{-12}$	0.298
0.3429	0.0424	0.0252	0.1061	0.278	$9.28 \times 10^{-4}$	$16.4 \times 10^{-5}$	$3.2 \times 10^{-5}$	$8.3 \times 10^{-12}$	0.303
0.3422	0.0395	0.0228	0.0943	0.233	$8.61 \times 10^{-4}$	$13.8 \times 10^{-5}$	$2.9 \times 10^{-5}$	$7.1 \times 10^{-12}$	0.304
0.3416	0.0369	0.0210	0.0848	0.192	$7.80 \times 10^{-4}$	$11.5 \times 10^{-5}$	$2.7 \times 10^{-5}$	$5.8 \times 10^{-12}$	0.307
0.3411	0.0346	0.0196	0.0772	0.163	$6.99 \times 10^{-4}$	$9.6 \times 10^{-5}$	$2.4 \times 10^{-5}$	$4.7 \times 10^{-12}$	0.303

Note: Recalculation of Zhong-Lynch's experiments<sup>[4]</sup>;  $N_S$  refers to the atomic fraction of sulfur in the Cu-S-Pb melts;  $N_{\text{CuS}}$  refers to the mole fraction of CuS in the  $\text{CuS}_{0.5}$ -CuS-PbS system matte;  $(p_{\text{S}_2})^{1/2}$ -ZL is the square root of  $\text{S}_2$  partial pressure from Zhong and Lynch<sup>[4]</sup>;  $(p_{\text{S}_2})^{1/2}$ -SM is the square root of  $\text{S}_2$  partial pressure from Schuhmann and Moles<sup>[15]</sup> and  $p$  (i) refers to the partial pressure (in atm) of gaseous species i over molten matte at 1533 K.

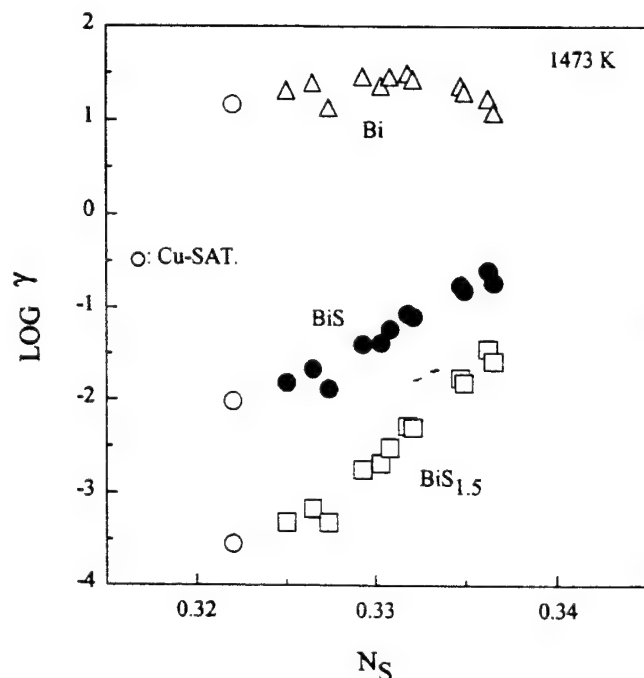


Fig. 2—Raoultian activity coefficients ( $\gamma$ ) of Bi (l), BiS (l), and BiS<sub>1.5</sub> (l) in the  $\text{CuS}_{0.5}$ -Cu(-CuS)-Bi,  $\text{CuS}_{0.5}$ -Cu(-CuS)-BiS, or  $\text{CuS}_{0.5}$ -Cu(-CuS)-BiS<sub>1.5</sub> system matte. The term  $N_S$  refers to the atomic fraction of sulfur in the Cu-S-Bi melt. Data points are from RJ,<sup>[3]</sup> except for the Cu-saturated mattes attributed to NEMP.<sup>[18]</sup>

## Influence of Solidification Variables on the Dendrite Arm Spacings of Ni-Based Superalloys

H.S. WHITESELL, L. LI, and R.A. OVERFELT

The primary ( $\lambda_1$ ) and secondary ( $\lambda_2$ ) dendrite arm spacings are key microstructural features of directionally solidified castings since they influence many of the important mechanical properties. For any given alloy, the spacings are controlled by the thermal gradient,  $G$ , and the solidification velocity,  $V$ , as well as any potential effects of convection.

Bouse and Mihalisin<sup>[1]</sup> reviewed the literature and summarized the effect of cooling rate ( $GV$ ) on  $\lambda_1$  and  $\lambda_2$  for eight different nickel-based superalloys. Hunt<sup>[2]</sup> and Kurz and Fisher<sup>[3]</sup> have shown that primary dendritic spacings in binary alloy systems under steady-state growth can be characterized by

$$\lambda_1 = KG^a V^b \quad [1]$$

where  $a = -1/2$ ,  $b = -1/4$ , and  $K$  is an alloy constant. Quested and McLean<sup>[4]</sup> investigated the primary spacings for four nickel-based superalloys and showed that  $\lambda_1$  was indeed proportional to  $G^{-1/2}V^{-1/4}$  when the dendritic structures were well established (high  $G$  and high  $V$ ). Quested and McLean noted that the experimental data deviated from Eq. [1] when plane front solidification was approached.

Bouchard and Kirkaldy<sup>[5]</sup> evaluated a range of binary alloys and found exponents for  $G$  and  $V$  to be generally  $(-0.3 \text{ to } -0.5)$  and  $(-0.1 \text{ to } -0.39)$ , respectively. Bouchard and Kirkaldy suggested that the difference between the experimentally measured exponents of  $G$  and  $V$  and the theoretical exponents  $(-0.5 \text{ and } -0.25)$  is mainly due to convection effects. Such an explanation is consistent with very careful directional solidification work reported by McCartney and Hunt<sup>[6]</sup> on alloys of Al-Cu-Mg. McCartney and Hunt chose ternary alloys with additions of Cu carefully selected to cancel out the buoyant effects of Mg and determined exponents of  $a = -0.55 \pm 0.02$  and  $b = -0.28 \pm 0.02$  very close to the theoretically expected values.

However, recently, Hunt and Lu<sup>[7]</sup> used a numerical model of solute transport in the liquid to describe the array growth

5. R.W. Ruddle, B. Taylor, and A.P. Bates: *Trans. Inst. Mining Metall.*, 1966, vol. 75C, pp. 1-12.
6. E.T. Turkdogan: *Physicochemical Properties of Molten Slags and Glasses*, The Metals Society, London, 1983, pp. 309-17.
7. A. Yazawa, S. Nakazawa, and Y. Takeda: in *Advances in Sulfide Smelting*, vol. 1, *Basic Principles*, H.Y. Sohn, D. B. George, and A.D. Zunkel, eds., TMS, Warrendale, PA, 1983, pp. 99-117.
8. M. Nagamori, W.J. Errington, P.J. Mackey, and D. Poggi: *Metall. Mater. Trans. B*, 1994, vol. 25B, pp. 839-53.
9. C.W. Bale and J.M. Toguri: *J. Thermal Anal.*, 1971, vol. 3, pp. 153-67.
10. O. Kubaschewski and C.B. Alcock: *Metallurgical Thermochemistry*, Pergamon Press, New York, NY, 1979, pp. 360 and 368.
11. I. Barin: *Thermochemical Data of Pure Substances*, VCH, Weinheim, 1989, pp. 1127 and 1129.
12. P.C. Chaubal and M. Nagamori: *Metall. Trans. B*, 1988, vol. 19B, pp. 547-56.
13. E.T. Turkdogan: *Physical Chemistry of High Temperature Technology*, Academic Press, New York, NY, 1980, p. 7.
14. M. Nagamori, Y. Takeda, and A. Yazawa: *Metall. Rev. MMIJ*, 1989, vol. 6(1), pp. 6-21.
15. R. Schuhmann and O.W. Moles: *Trans. TMS-AIME*, 1951, vol. 191, pp. 235-41.
16. P.C. Chaubal and M. Nagamori: *Metall. Trans. B*, 1982, vol. 13B, pp. 339-48.

H.S. WHITESELL and L. LI, Graduate Research Assistants, and R.A. OVERFELT, Associate Professor, are with the Mechanical Engineering Department, Auburn University, Auburn, AL 36849.  
Manuscript submitted August 16, 1999.

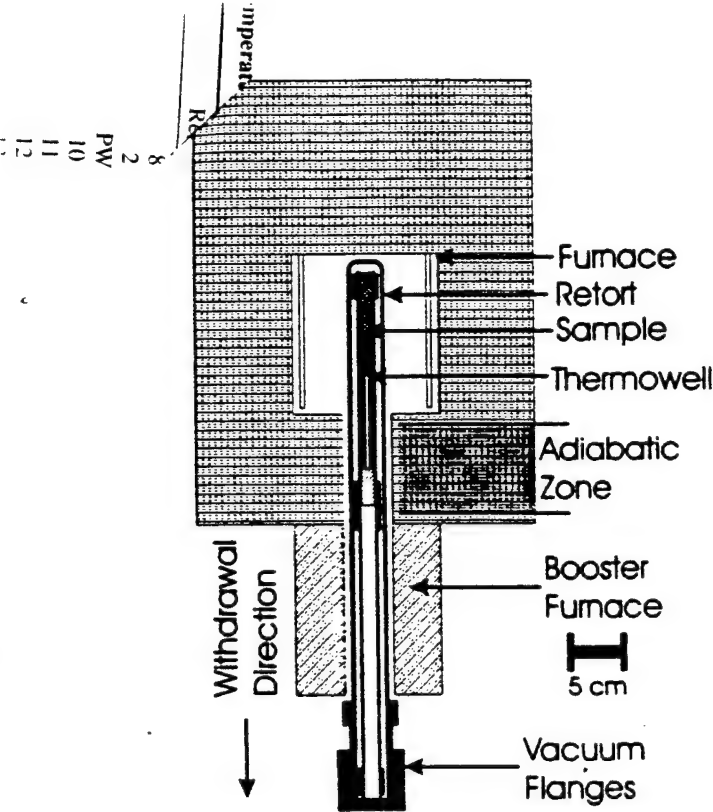


Fig. 1—Schematic of the modified Bridgman apparatus for performing directional solidification experiments.

of cells and dendrites, which enabled the prediction of self-consistent axisymmetric interface shapes and array spacing ( $\lambda_1$ ). For cellular growth, Hunt and Lu's model predicts  $\lambda_1 \propto V^{-0.6}$  with no significant dependence on thermal gradient. For dendritic growth, their model predicts  $\lambda_1 \propto G^{-0.6}V^b$  where the exponent on  $V$  is gradient dependent and calculated to be between  $-0.34$  and  $-0.58$ . Hunt and Lu note that over a narrow range of  $G$  and  $V$ , exponents on  $G$  and  $V$  can vary dramatically.

Ma and Sahm<sup>[8]</sup> considered the spacing between dendrites to be the sum of the dendrite trunk diameter and twice the sidearm lengths. These investigators developed a new analytical model of the dependence of primary spacing on  $G$  and  $V$  and found reasonable agreement with experimental data from several alloys. For cells, Ma and Sahm's model predicts  $\lambda_1 \propto V^{-0.5}$  with no dependence on gradient. For dendritic growth at high velocities, Ma and Sahm's model predicts  $\lambda_1 \propto G^{-0.5}V^{-0.25}$ , in agreement with earlier models.<sup>[2,3]</sup> For dendritic growth at lower velocities, a transition behavior is predicted where the microstructure changes from cells to cellular dendrites to fully developed dendrites.

Secondary dendrites result from capillarity instabilities at the dendrite tip. These perturbations are small at first and

then grow at the expense of the smaller arms in a process similar to Ostwald ripening. The driving force for this coarsening is the increase in interfacial energy at the tips of the smaller arms due to the higher curvature there. The coarsening kinetics generally produce the following relationship for secondary dendrite arm spacing:

$$\lambda_2 = M t_f^3 \quad [2]$$

where  $M$  is an alloy-dependent constant and  $t_f$  is the local solidification time given approximately by  $T_0(GV)^{-1}$ , where  $T_0$  is the equilibrium freezing range.<sup>[3]</sup>

The purpose of this article is to present new data on the dependence of primary and secondary dendrite arm spacings on thermal gradient, solidification velocity, and cooling rate for a wide variety of nickel-based superalloys. In addition, cooling rates lower than previously reported were used and the microstructural transition from cells to fully developed dendrites evaluated for PWA1484.

In this investigation, cylindrical investment cast bars (12.7- to 19-mm diameter and 23.3-cm long) were remelted and carefully solidified using a modified Bridgman apparatus, as shown in Figure 1. The samples were contained in an alumina retort with a high-purity argon atmosphere. Directional solidification at very low axial thermal gradients was accomplished by withdrawing the sample from the hot zone of the furnace through the adiabatic region and finally into the cooler region of the booster heater, as shown in Figure 1. The constant withdrawal speeds used varied between  $0.000005$  and  $0.001 \text{ m s}^{-1}$  and the constant hot zone temperatures applied varied between  $1400$  and  $1600$  °C. Sample temperatures and thermal gradients were recorded with a computer data acquisition system and dual  $0.38\text{-mm}$  diameter B-type (Pt-30 pct Rh/Pt-15 pct Rh) thermocouples spaced  $10 \text{ mm}$  apart and inserted into the center of the samples. The alloys investigated and their compositions are shown in Table I. The thermocouple data and validated computer simulations<sup>[9]</sup> of the sample/furnace system showed that solidification takes place in the adiabatic region. The primary dendrite arm spacings measured were constant over the central region of the solidified samples indicating that steady-state growth conditions were achieved. Thus, the solidification velocities were assumed to be equal to the withdrawal velocities.

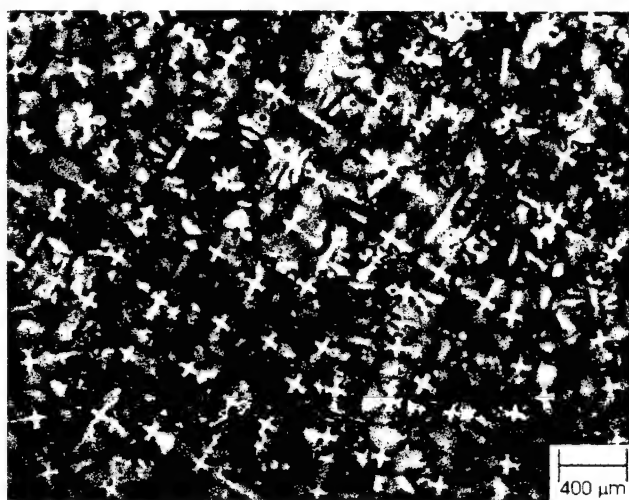
Samples for metallographic characterization were ground and polished using standard metallographic techniques. A variety of etchants have been used, but one that has worked well for analyzing dendritic microstructures for a variety of these nickel-based superalloys is  $10 \text{ mL HCl}$ ,  $10 \text{ mL HNO}_3$ ,  $0.3 \text{ g molybdc acid}$ , and  $15 \text{ mL distilled H}_2\text{O}$ . Metallographic investigations were performed with an Olympus PME3 inverted metallurgical microscope. Primary dendrite

Table I. Alloys and Compositions (Weight Percent) Investigated

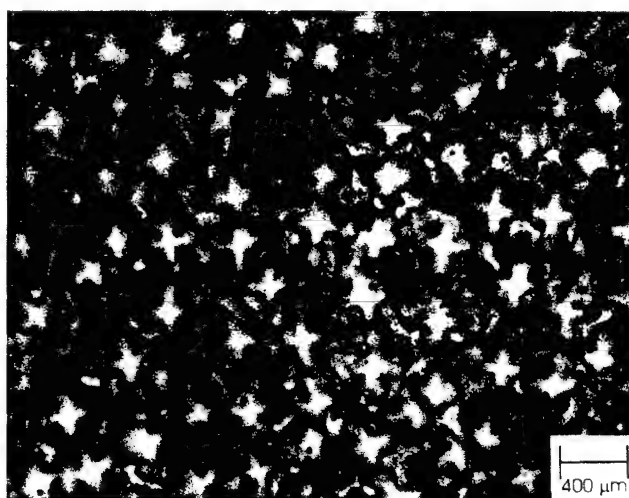
	Ni	W	Co	Cr	Al	Ta	Hf	Ti	Mo	Fe	Nb	Re	Cu	C	Zr	B
MAR-M247	bal	10.0	10.13	8.35	5.7	3.07	1.23	0.99	0.8	0.95	—	—	—	0.162	0.045	0.015
PWA-1484	bal	5.86	9.88	4.96	5.7	8.74	—	—	1.89	—	—	2.98	—	0.0238	0.0028	0.001
René-N5	bal	5.0	7.4	6.9	6.3	6.6	0.12	—	1.45	—	—	2.97	—	—	—	—
René-108	bal	9.86	9.60	8.43	5.5	2.99	1.47	0.70	0.49	0.12	—	—	0.01	0.08	0.01	—
IN-718	bal	—	—	18.3	0.5	—	—	0.83	2.0	18.9	4.6	—	0.15	0.08	—	—



(a)

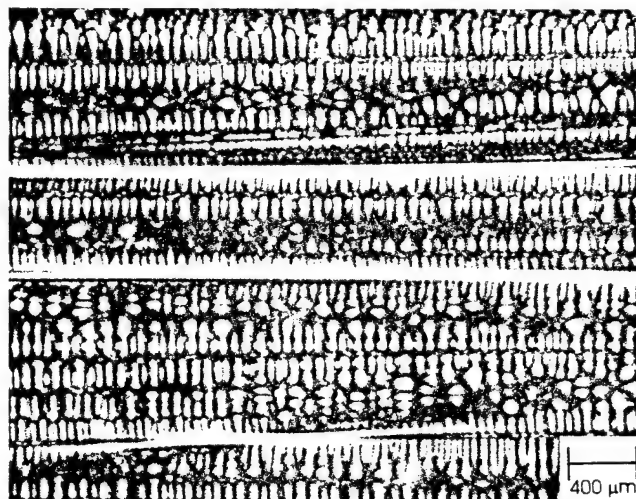


(b)

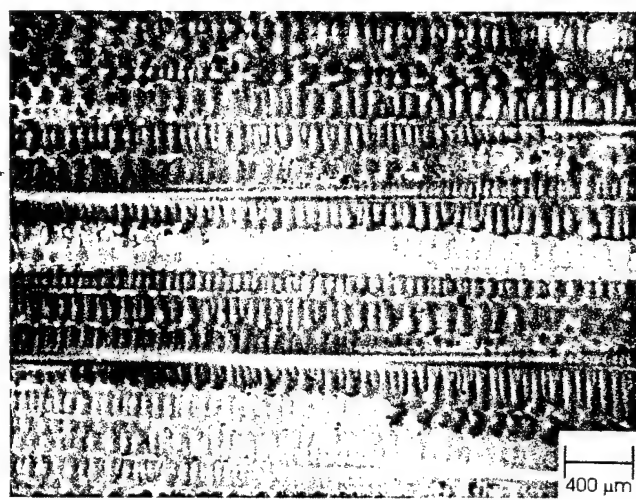


(c)

Fig. 2—Transverse sections of MAR-M-247 grown at the solidification conditions indicated. (a)  $G = 36\text{ }^{\circ}\text{C/cm}$ ,  $V = 0.01\text{ cm/s}$ ,  $GV = 0.36\text{ }^{\circ}\text{C s}^{-1}$ ; (b)  $G = 38.3\text{ }^{\circ}\text{C/cm}$ ,  $V = 0.005\text{ cm/s}$ ,  $GV = 0.192\text{ }^{\circ}\text{C s}^{-1}$ ; and (c)  $G = 43\text{ }^{\circ}\text{C/cm}$ ,  $V = 0.0005\text{ cm/s}$ ,  $GV = 0.022\text{ }^{\circ}\text{C s}^{-1}$ .



(a)



(b)



(c)

Fig. 3—Longitudinal section of PWA 1484 grown at the solidification conditions indicated. (a)  $G = 20.4\text{ }^{\circ}\text{C/cm}$ ,  $V = 0.01\text{ cm/s}$ ,  $GV = 0.204\text{ }^{\circ}\text{C s}^{-1}$ ; (b)  $G = 23.4\text{ }^{\circ}\text{C/cm}$ ,  $V = 0.005\text{ cm/s}$ ,  $GV = 0.117\text{ }^{\circ}\text{C s}^{-1}$ ; and (c)  $G = 31.1\text{ }^{\circ}\text{C/cm}$ ,  $V = 0.001\text{ cm/s}$ ,  $GV = 0.031\text{ }^{\circ}\text{C s}^{-1}$ .

arm spacings were estimated from transverse photomicrographs using the usual relationship  $\lambda_1 = (A/N)^{0.5}$ , where  $A$  is the cross-sectional area of the photograph and  $N$  is the number of primary arms in the photograph.<sup>[10]</sup> This relationship is valid for a square array.<sup>[6]</sup> Secondary dendrite arm spacings were measured from longitudinal sections and from well-aligned dendrite trunks. Compositions of the primary segregating elements along the length of the samples were determined on transverse cross sections using a JEOL\* 840

\*JEOL is a trademark of Japan Electron Optics Ltd., Tokyo.

scanning electron microscope with an Oxford Instruments energy dispersive spectroscopy system with programming to compensate for atomic number, absorption, and fluorescence effects.

Typical transverse micrographs from MAR-M-247\* sam-

\*MAR-M-247 is a trademark of Lockheed Martin, Baltimore, MD.

ples grown at a variety of  $G$  and  $V$  conditions are shown in Figure 2. As expected, the microstructure of the MAR-M-247 alloy exhibited a decreasing primary dendritic spacing as the thermal gradient and/or the solidification velocity increased. Although the details of the interdendritic phases present (carbides, Laves phases, etc.) varied from alloy to alloy depending upon the composition and the solidification parameters employed,  $\lambda_1$  for all alloys exhibited a similar behavior. Figure 3 shows typical longitudinal sections from directionally solidified samples of PWA1484 displaying some well-aligned primary dendrite trunks with secondary dendrite arms (Figures 3(a) and (b)). There is an obvious transition from dendritic (Figures 3(a) and (b)), to cellular growth (Figure 3(c)) at a cooling rate of  $0.031^\circ\text{C s}^{-1}$ .

The results on primary dendrite arm spacings are summarized in Figures 4(a) and (b), which show the relationship between  $\lambda_1$  and the  $G^aV^b$  parameter ( $a = -0.5$  and  $b = -0.25$ ). Figure 4(a) includes new data from the alloys given in Table I as well as data from the literature<sup>[1,4,11-13]</sup> and extends the  $G^aV^b$  parameter to significantly higher values (i.e., lower cooling rates) than previously reported in the literature. To more clearly evaluate the transition from cellular growth to fully developed dendritic growth, the primary spacing data for a single alloy, PWA 1484, are plotted against the  $G^{-0.5}V^{-0.25}$  parameter in Figure 4(b). The velocities used are shown and the morphologies of the cellular and/or dendritic microstructural results are also labeled. At the highest values of  $G^{-0.5}V^{-0.25}$  (lowest cooling rates), the results are bounded with the smallest  $\lambda_1$  data by cellular growth. Conversely, at the lower values of  $G^{-0.5}V^{-0.25}$  (highest cooling rates), the results are bounded with the largest  $\lambda_1$  data by fully developed dendritic growth (where primary, secondary, and tertiary arms are exhibited). In between, dependent upon the specific values of  $G$  and  $V$  employed, the microstructure changes from cellular to cellular-dendritic to dendritic to well-developed dendritic with tertiary arms. The error bars in Figure 4(b) represent actual experimental scatter ( $\pm 2\sigma$ ) in measurements of  $\lambda_1$  and maximum estimated uncertainties in measurements of  $G$  ( $\pm 5$  pct) and  $V$  ( $\pm 1$  pct). Additional work on PWA1484 is ongoing to establish whether the Ma and Sahm model can quantitatively describe this transition behavior.

The primary and secondary dendrite arm spacings are also often correlated with cooling rate. The terms  $\lambda_1$  and  $\lambda_2$  are

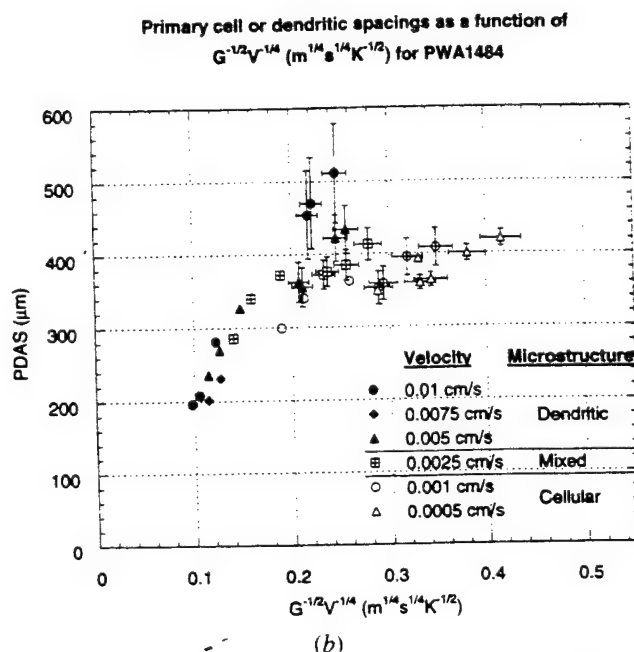
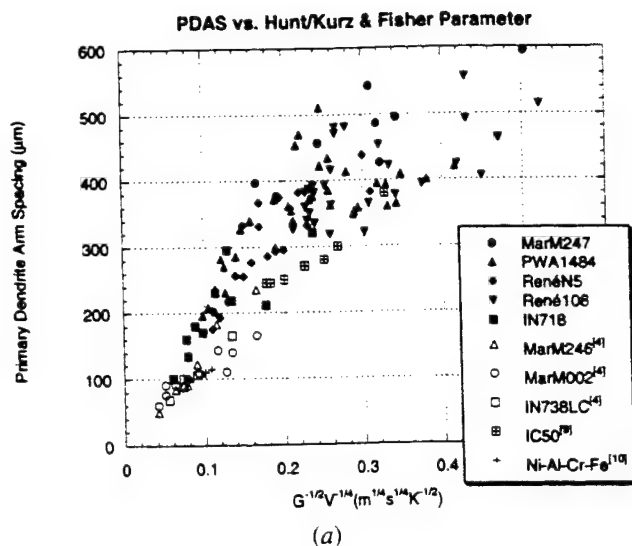


Fig. 4—Primary dendrite arm spacing ( $\lambda_1$ ) as a function of the solidification parameter  $G^{-1/2}V^{-1/4}$ : (a) a wide range of nickel-based superalloys and (b) PWA 1484.

shown vs cooling rate in Figures 5(a) and (b), respectively. The primary dendrite arm spacing generally increases as the cooling rate decreases. The secondary dendrite arm spacing is theoretically proportional to  $(GV)^{-1/3}$ . Figure 5(b) shows the secondary dendrite arm spacings vs cooling rate for three of the alloys given in Table I as well as data from the literature.<sup>[1]</sup> A regression analysis on the secondary dendrite arm spacing data showed that the experimentally measured exponent for the entire data set is 0.38, in reasonable agreement with Eq. [2].

Low- $g$  experiments have shown that when natural convection effects are eliminated during directional solidification of Al-Cu alloys, dendrites grow under diffusion control and their spacings follow Eq. [1].<sup>[14]</sup> The directionally solidified samples in this investigation exhibited no significant longitudinal macrosegregation, as evidenced by the compositional results of typical MAR-M-247 and PWA 1484 samples



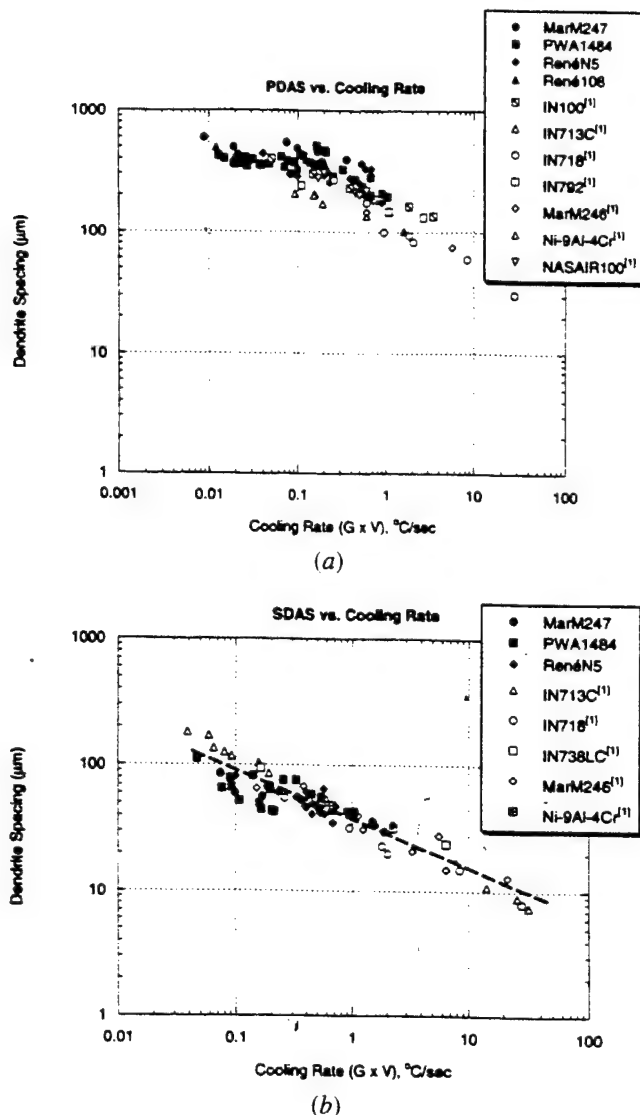


Fig. 5—Dendrite arm spacings for a wide range of nickel-based superalloys as a function of the cooling rate ( $GV$ ): (a) primary ( $\lambda_1$ ) and (b) secondary ( $\lambda_2$ ).

shown in Figure 6. In addition, no significant radial segregation was found. These results indicate that convection effects were minimal in these samples and would not have played a major role in determining the DS (directional solidification) microstructures or the dendritic/cellular spacings.

Dendritic spacing data for families of alloys are often correlated with the cooling rate ( $GV$ ) or the  $G^{-0.5}V^{-0.25}$  parameter. Although potentially useful for empirical predictions of microstructural development, such correlations may not yield valuable insight into the fundamental solidification behavior. The present data on PWA 1484 indicate that when convection is minimized and dendritic structures are well established during directional solidification,  $\lambda_1$  is proportional to  $G^{-1/2}V^{-1/4}$ . Such behavior, within the experimental uncertainty, is expected from the results of theoretical models. However, when the imposed thermal gradient and solidification velocity enable microstructures to exhibit a mixed morphology of dendrites and cells, the solidification behavior is more complex and current theoretical spacing models must be extended.

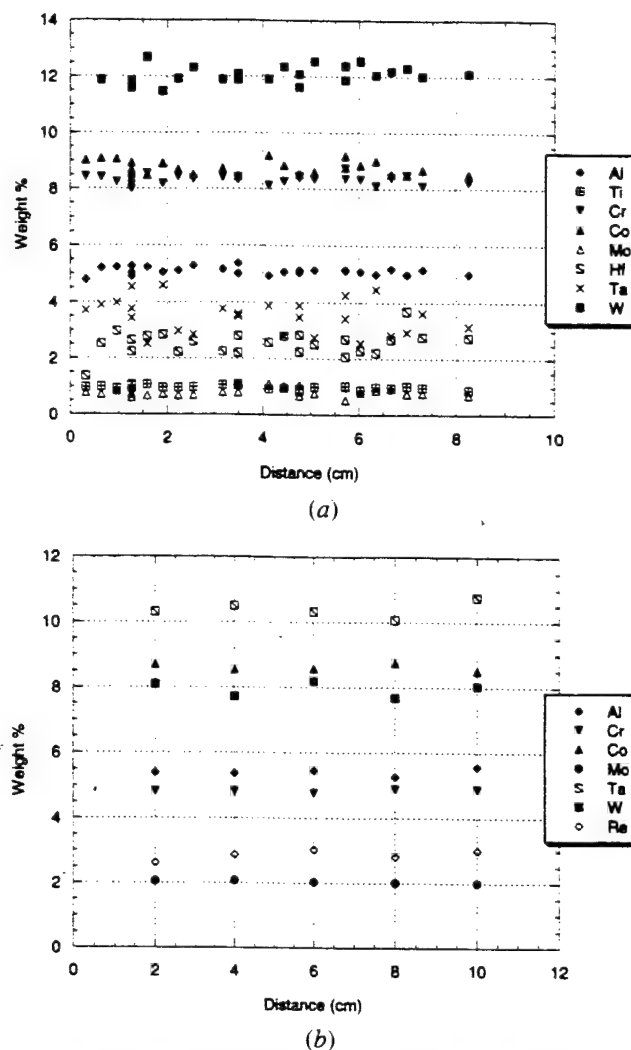


Fig. 6—Longitudinal segregation in typical samples of (a) MAR-M-247:  $V = 0.005 \text{ cm s}^{-1}$  and  $G = 38.3 \text{ °C cm}^{-1}$ ; and (b) PWA1484:  $V = 0.001 \text{ cm s}^{-1}$  and  $G = 38 \text{ °C cm}^{-1}$ .

## ACKNOWLEDGMENTS

This material is based upon work supported by, or in part by, the United States Army Research Office under Grant No. ARO DAAH04-96-1-0321 and NASA's Office of Life and Microgravity Science and Applications through Cooperative Agreement Number NCC8-128. Cast samples were graciously provided by Howmet Corporation (Whitehall, MI). Permission to publish the data on PWA1484 was kindly provided by Pratt & Whitney Company (West Palm Beach, FL), while General Electric Company (Lynn, MA) kindly permitted publication of the René' N5 and René' 108 data. Technical discussions and the assistance of Dr. Boyd Mueller and Mr. Terry Simon, Howmet Corp., in preparing the investment castings are especially appreciated.

## REFERENCES

1. G.K. Bouse and J.R. Mihalisin: *Superalloys, Supercomposites and Superceramics*, Academic Press Inc., London, 1989, pp. 99-148.
2. J.D. Hunt: *Solidification and Casting of Metals*, The Metals Society, London, 1979, Book 192, p. 3.
3. W. Kurz and D.J. Fisher: *Fundamentals of Solidification*, Trans Tech Publications, Aedermannsdorf, Switzerland, 1992, pp. 80-89.



4. P.N. Quested and M. McLean: *Mater. Sci. Eng.*, 1984, vol. 65, pp. 171-80.
5. D. Bouchard and J.S. Kirkaldy: *Metall. Mater. Trans. B*, 1997, vol. 28B, pp. 651-63.
6. D.G. McCartney and J.D. Hunt: *Acta Metall.*, 1981, vol. 29, pp. 1851-63.
7. J.D. Hunt and S.-Z. Lu: *Metall. Mater. Trans. A*, 1996, vol. 27A, pp. 611-23.
8. Dexin Ma and Peter R. Sahm: *Metall. Mater. Trans. A*, 1998, vol. 29A, pp. 1113-19.
9. D.-M. Wang: Auburn University, Auburn, AL, unpublished research, 1999.
10. M. Vijayakumar, S.N. Tewari, J.E. Lee, and P.A. Curreri: *Mater. Sci. Eng.*, 1991, vol. A132, pp. 195-201.
11. H.K. Kim, J.C. Earthman, and E.J. Lavernia: *Acta Metall. Mater.*, 1992, vol. 40 (4), pp. 637-47.
12. J. Lapin, A. Klimova, R. Velisek, and M. Kursa: *Scripta Mater.*, 1997, vol. 37(1), pp. 85-91.
13. J. Chen, J.H. Lee, Y.S. Yoo, S.J. Choe, Y.T. Lee, and B.Y. Huang: *High Temp. Mater. Processes*, 1999, vol. 18(3), pp. 109-23.
14. M.D. Dupouy, D. Camel, and J.J. Favier: *Acta Metall. Mater.*, 1992, vol. 40 (7), pp. 1791-1801.

## Formation of Aluminum Titanate-Mullite Composite from Bauxite Red Mud

T. MAHATA, B.P. SHARMA, S.R. NAIR, and D. PRAKASH

Aluminum titanate ceramics have a low thermal expansion coefficient, which results in excellent thermal shock resistance, low Young's modulus, moderate strength, and low wettability by liquid metals.<sup>[1,2]</sup> The former three properties are related to the presence of extensive microcracks in the sintered body.<sup>[2]</sup> Crystallographic anisotropy in the thermal expansion coefficient<sup>[3]</sup> is mainly responsible for the development of microcracks during cooling from the sintering temperature. Mechanical strength can be improved by incorporation of a second phase such as mullite or zirconia.<sup>[4,5]</sup> The dispersed second phase acts as a barrier against microcrack coalescence. Due to the combination of the aforementioned physical and mechanical properties, aluminum titanate and its composites are potential materials for applications as liquid metal flow regulators, risers, thermocouple sleeves, burner nozzles, ceramic filters, etc.<sup>[1,6,7]</sup> The present article deals with the preparation of an aluminum titanate-mullite composite material from bauxite red mud.

Red mud, the waste by-product of Bayer's process in aluminum extraction, contains mainly oxides of aluminum, titanium, iron, and silicon. Most of the Indian red muds are characterized by high titania content (16 to 25 wt pct).<sup>[8]</sup> In this article, experimental results are based on red mud obtained from M/s BALCO (Kobra, MP, India). The composition of BALCO red mud after calcination at 800 °C is given in Table I. In the table, the unaccounted for balance 12.3 pct may be attributed to the presence of molecular water (mainly in  $\text{AlOOH}$ ) and oxides of several other elements such as V, Cr, Zr, Ga, Ba, Pb, Mn, and Mg. The red mud was first leached with water to remove water soluble sodium compounds. This was followed by leaching with

dilute hydrochloric acid to preferentially remove  $\text{Fe}_2\text{O}_3$ , leaving the residue rich in  $\text{Al}_2\text{O}_3$ ,  $\text{TiO}_2$ , and  $\text{SiO}_2$ . The details of the leaching experiments with three different acid concentrations are shown in Table II. With a low (1:3) HCl concentration, only 13.9 pct iron was removed. More than 90 pct iron was leached out with either 1:1 or 3:1 HCl. However, the removal of iron with 3:1 HCl was marginally higher than that with 1:1 HCl. On the other hand, the amount of residue obtained after leaching with 3:1 HCl was considerably less than that obtained after leaching with 1:1 HCl. It was confirmed that with 3:1 HCl, a substantial amount of  $\text{Al}_2\text{O}_3$  was also leached out along with the  $\text{Fe}_2\text{O}_3$ . Considering the objective of preferentially leaching away  $\text{Fe}_2\text{O}_3$ , while retaining most of the  $\text{Al}_2\text{O}_3$ ,  $\text{TiO}_2$ , and  $\text{SiO}_2$  values, 1:1 HCl concentration was considered to be optimum among the three different acid concentrations selected. The residual  $\text{Fe}_2\text{O}_3$  has been found to be useful in the present study, as discussed later.

The residue, obtained after leaching with 1:1 HCl, was calcined at 800 °C, 2 h. The composition of this residue is given in Table III.  $\text{Al}_2\text{O}_3$  powder (99.5 pct purity, 0.5  $\mu\text{m}$  median size) was mixed with this residue to independently adjust molar ratios of  $\{(\text{Al}_2\text{O}_3 + \text{Fe}_2\text{O}_3) / \text{TiO}_2\} = 1.0$  and  $\{\text{Al}_2\text{O}_3 / \text{SiO}_2\} = 1.5$  and thus to obtain a composite material consisting of aluminum titanate ( $\text{Al}_2\text{TiO}_5$ )-iron titanate ( $\text{Fe}_2\text{TiO}_5$ ) solid solution and mullite ( $3\text{Al}_2\text{O}_3 \cdot 2\text{SiO}_2$ ) phases after final reaction synthesis. Mixing was done for 8 hours by ball milling in a porcelain pot using 3-mm diameter alumina balls. Differential thermal analysis (DTA) (with a heating rate of 10 °C/min in argon) was carried out on this mixture to obtain the reaction synthesis temperature. The mixed powder was pelletized and heated to 1400 °C in air for 2 hours. X-ray diffraction (XRD) was carried out on as-received red mud, leached residue (calcined at 800 °C), and reaction synthesized product.

Figure 1 shows the XRD pattern of the as-received red mud. Major peaks have been assigned to silicates and titanates of iron and aluminum. Free ferric oxide ( $\text{Fe}_2\text{O}_3$ ) peaks are also seen in the pattern. The XRD pattern for leached residue, calcined at 800 °C, is presented in Figure 2.

Anatase ( $\text{TiO}_2$ ), rutile ( $\text{TiO}_2$ ), aluminum titanate ( $\text{Al}_2\text{TiO}_5$ ), and silica ( $\text{SiO}_2$ ) are the major phases present. Some very low intensity peaks correspond to  $\chi(\text{chi})/\kappa(\text{kappa})$  alumina. These results indicate that iron oxide has been leached out from its silicate and titanate compounds leaving a residue of titania and silica. Titania is mostly present in the anatase form. Material balance indicates that a part of alumina is also leached out with iron oxide.

The DTA curve in Figure 3 shows an exothermic peak starting at 1070 °C. This exothermic peak is attributed to the formation of mullite.<sup>[9,10]</sup> Formation of titanates of aluminum and iron are endothermic reactions.<sup>[11,12]</sup> Onset of endothermic reaction is indicated by a downward slope starting at 1160 °C. The small trough at 1180 °C may be attributed to the formation of iron titanate, which is reported to occur at a lower temperature than that of aluminum titanate.<sup>[13]</sup> The large endothermic peak starting at 1210 °C is largely due to the formation of aluminum titanate. Figure 4 shows the XRD spectrum of the composite obtained after heating the alumina-added residue to 1400 °C. The pattern is predominantly composed of aluminum titanate and mullite peaks. Peaks corresponding to alumina, titania, or iron oxide are not

T. MAHATA and D. PRAKASH, Scientific Officers, D. B.P. SHARMA, Scientific Officer, H. and Head of Division, and S.R. NAIR, Scientific Officer, C. are with the Powder Metallurgy Division, Bhabha Atomic Research Centre, Navi-Mumbai - 400 705, India.

Manuscript submitted February 17, 1999.

# **Influence of Solidification Variables on the Microstructure, Macrosegregation, and Porosity of Directionally Solidified Mar-M247**

H.S. Whitesell and R.A. Overfelt

Auburn University

Materials Engineering Program

Mechanical Engineering Dept., 201 Ross Hall, Auburn, AL 36849

## **ABSTRACT**

The solidification microstructure is critical in determining the amount and distribution of porosity that develops during the freezing of castings. However, microstructural effects during freezing are often characterized only by the corresponding permeability or tortuosity of the mushy zone. As the microstructural length scales (primary and secondary dendrite arm spacings) decrease (1) the mushy zone permeability would be expected to decrease, and (2) nucleated pores would be increasingly isolated. Although the first effect would tend to increase the observed porosity, the second effect would tend to decrease the porosity. To better understand these competitive mechanisms, a series of controlled unidirectional solidification experiments were performed on bars of nickel-base superalloy Mar-M247. Samples were produced with constant dendrite arm spacing throughout an extended length of each cast bar. The axial thermal gradient and withdrawal velocity imposed on each casting were varied between castings to produce a range of microstructures from equiaxed dendritic to cellular dendritic. Macrosegregation effects along the lengths of the bars were evaluated and the resultant impact upon the density along the length of each casting also characterized. The density measurements were found to be very sensitive to both (1) compositional macrosegregation in these castings and (2) internal porosity. Statistical analyses of microporosity in the castings were based upon metallographic

measurements. The development of microporosity in the unidirectionally solidified castings is shown to be dependent upon the hydrogen gas content of the samples and the imposed solidification velocity  $V$  through the sample's cast microstructures. An optimum withdrawal velocity of 0.005 – 0.01 cm/s was found which leads to a closely spaced dendrite arms, a large number of very small pores and a minimum porosity level. Lower velocities lead to increased porosity from larger pores whereas higher velocities lead to macroporosity due to centerline shrinkage.

## I. INTRODUCTION

Nickel-based superalloys have evolved into complicated alloy systems due to manufacturers' efforts to obtain the best combination of high temperature strength and oxidation resistance to enable higher operating temperatures in turbines. More recently, considerable research has concentrated on better understanding of the manufacturing processes to improve productivity and lower costs. Fundamental studies of the effect of solidification process parameters on microstructural development during casting of these complex superalloys are important because the as-solidified microstructure dictates subsequent heat treatments and the ultimate engineering performance of the casting. The dendrite arm spacings (primary and secondary), macro/microsegregation, distribution and morphologies of precipitates as well as porosity all influence subsequent mechanical properties.

Although equiaxed and chill castings have been widely used to study porosity formation, such castings exhibit coupled thermal gradients and solidification velocities that change over time. As reviewed by Sigworth and Wang<sup>1</sup>, these attempts to quantitatively relate porosity in

equiaxed castings to the imposed process parameters by means of the pressure drop through the mushy zone via Darcy's law have met with only limited success. Sigworth and Wang concluded that although Darcy's law can be applied to porous media flow of liquid metal through a mushy zone, the pressure drops associated with flow through the mushy zone are simply too small to contribute to porosity formation. These authors proposed an alternative "geometric model" that predicted increased probabilities of isolated pools of liquid metal as thermal gradients decreased.

Unidirectional solidification is a powerful technique for studying solidification phenomena since the thermal gradient and the solidification velocity can be de-coupled. In addition, the mushy zone's interdendritic feeding geometry is simplified with respect to complex, equiaxed mushy zones. The aligned dendritic or cellular growth expected from careful unidirectional solidification experiments is shown schematically in Figure 1. Unfortunately, few experimentalists (e.g., Lecomte-Beckers<sup>2</sup>, Kao, Chang and Lee<sup>3</sup>, Lin and Sekhar<sup>4</sup>, and Ho and Sekhar<sup>5</sup>) have applied directional solidification techniques to investigate porosity formation.

Porosity is generally expected to nucleate heterogeneously when the local pressure tending to close pores is exceeded by the local pressure to open pores. The overall ambient pressure ( $P_o \sim 1$  atm), the metallostatic head pressure ( $P_p = \rho_L gh$ ) and the liquid-vapor surface tension pressure ( $P_\sigma = 2\sigma_{LV}/r$  for a spherical bubble of local radius  $r$ ) all tend to close pores. Gas pressure ( $P_g$ ) from partitioned gaseous species and the pressure drop in the mushy zone ( $\Delta P_{MZ}$ ) both tend to open pores. When the total net pressure to nucleate becomes higher than the combined pressures to close, conditions for pore nucleation are favorable and can be represented as:

$$P_T = (P_o + \frac{2\sigma_{LV}}{r} + \rho_L gh) - (P_g + \Delta P_{MZ}) \quad [1]$$

where  $\rho_L$  is the liquid metal density,  $g$  is the gravitational constant,  $h$  is the height of liquid metal,

and  $\sigma_{LV}$  is the liquid-vapor surface tension. Thus, when  $P_T < 0$ , porosity would be expected.

As noted by Piwonka and Flemings<sup>6</sup>, the space between aligned cells during directional solidification can be most simply modeled as capillary tubes with lengths approximately equal to the lengths of the aligned cells and diameters approximately equal to the intercellular spaces. Liquid metal flows down the intercellular space to feed the solidification shrinkage near the roots of the cells. The Hagen-Poiseuille equation describes pressure drop down a capillary tube as:

$$\Delta P = \frac{8 \mu L U}{r^2} \quad [2]$$

where  $\Delta P$  is the pressure drop,  $\mu$  is the viscosity of liquid,  $U$  is the velocity of liquid in the capillary tube, and  $r$  is the radius of the capillary tube. If the length of the capillary tube (i.e., interdendritic space) is described in terms of solidification variables ( $L \sim T_o/G$ ), and the solidification velocity ( $V_s$ ) is used, then the equation for pressure drop becomes

$$\Delta P_{MZ} = \frac{8 \mu \beta \Delta T_o V_s}{G r^2} \quad [3]$$

where  $\Delta T_o$  is the freezing range of alloy,  $G$  is the thermal gradient,  $\beta = (\rho_S - \rho_L)/\rho_S$ , and  $\rho_S$  and  $\rho_L$  are the densities of the solid and liquid, respectively.

Once an alloy is specified, the important metallurgical characteristics of equilibrium freezing range and equilibrium amount of eutectic are fixed. The only means remaining to exert control of microstructure in unidirectional solidification is in modifying the process parameters: thermal gradient and solidification velocity. The applied thermal variables play an important role in the formation of porosity during freezing. Higher hot zone temperatures provide larger thermal gradients, shorter mushy zones and suppressed development of secondary dendrite arms. The withdrawal velocity influences the interdendritic spacing due to the available time for solute

diffusion. Higher velocities promote the formation of secondary arms since there is less time for solute diffusion.<sup>7</sup> The simple models of Hunt<sup>8</sup> and Kurz & Fisher<sup>9</sup> indicate that the primary dendrite arm spacing,  $\lambda_1$ , should be proportional to  $G^{-1/2}V^{-1/4}$ . Recently Bouchard and Kirkaldy<sup>10</sup>, Ma and Sahm<sup>11</sup>, and Hunt and Lu<sup>12</sup> have shown that the exponent for  $G$  varies from -0.27 to -0.54 and  $V$  from -0.11 to -0.75 for many alloys. The authors' measurements<sup>13</sup> with a number of superalloys yielded exponents for  $G$  and  $V$  of -0.39 and -0.082, respectively.

Another microstructural variable likely to play a key role is the presence of secondary and tertiary dendrite arms. Low thermal gradients and high withdrawal velocities promote the formation of secondary dendrite arms. Although the presence of secondary dendritic arms decreases the permeability of the mushy zone for liquid metal flow normal to the primary dendritic arms, no effect on permeability for flow parallel to the primary arms has been reported.<sup>14,15</sup> Finally, secondary arm formation may actually reduce porosity by isolating pores and simply preventing their continued growth. Bachelet<sup>16</sup> *et. al.* proposed that there should be optimum casting conditions between fast and slow cooling leading to small evenly distributed micropores.

Accurate porosity data from aligned unidirectional solidification samples cast with a range of thermal gradients and solidification velocities are a prerequisite to understanding the important coupling phenomena among the process parameters and microstructural development that affect porosity in nickel-base superalloys for turbine applications. The material chosen for this research is the often-studied, nickel-based superalloy Mar-M247. The present paper reports on the roles of the process parameters on axial macrosegregation and the development of microstructure and porosity in Mar-M247.



## II. EXPERIMENTAL PROCEDURE

The experimental arrangement for the casting experiments is illustrated schematically in Figure 2. A vertical Bridgman furnace was used to melt and resolidify the samples. The withdrawal velocity was monitored and precisely controlled by personal computer. The sample was enclosed in an alumina retort which isolated the sample from the oxidizing atmosphere. A vacuum was drawn on the retort for each sample prior to melting and then the retort was backfilled with high purity argon gas. An Applied Test Systems Inc. box furnace (maximum temperature of 1600 °C) provided the hot zone and was controlled by a digital computer which enables multiple set points. A second booster furnace was utilized beneath the box furnace to modify the thermal conditions imposed on the samples and obtain low thermal gradients. An insulated adiabatic zone between the two furnaces was used to provide flat isotherms in that region. Sample temperatures and thermal gradients were recorded with a computer data acquisition system and dual 0.38 mm dia. B-type (Pt-30%Rh/Pt-15%Rh) thermocouples axially spaced 10 mm apart and inserted into the center of the samples. The thermocouple data showed that when the dendrites are aligned antiparallel to the thermal gradient, solidification takes place in the adiabatic region. The use of Bridgman directional solidification was critical for the present investigation because of the need for steady state solidification conditions (i.e., constant thermal gradients and constant solidification velocities) after allowing for the initial and final transients.

Table I gives the composition of the Mar-M247 alloy utilized in the present experiments. A series of twelve experiments were performed with three different hot zone temperatures (1600, 1500, 1400 °C) and four different withdrawal velocities (0.0005, 0.005, 0.01, 0.1 cm/s). The experimental data on macrosegregation and density for the 0.01 cm/s and 0.005 cm/s bars

were comparable and only the data for the 0.005 cm/s samples will be discussed below. Each as-cast cylindrical bar (length = 20 cm, diameter = 12.7 mm) was sectioned down the middle using wire EDM and 6.4 mm thick semicircular samples taken every 3 mm from one side. The other half of the bar was cut into 2.5 cm samples and mounted longitudinally for metallographic examination. Each sample was ground and polished using standard metallographic techniques. The etchant used to analyze microstructures was 10 mL HCl, 10 mL HNO<sub>3</sub>, 0.3 g molybdic acid, and 15 mL distilled H<sub>2</sub>O. An Olympus PME3 inverted metallurgical microscope was used to examine and photograph the samples. Primary dendrite arm spacings were estimated by averaging five transverse photomicrographs using the relationship  $\lambda_1 = (A/N)^{0.5}$ , where  $A$  is the cross-sectional area of the photograph and  $N$  is the number of primary arms in the photograph.<sup>17</sup> This relationship is valid for a square array.<sup>18</sup> Secondary dendrite arm spacings were measured from longitudinal sections by counting the number of secondary arms over a measured length on a minimum of three well-aligned dendrite trunks.

A number of samples were hot-isostatically-pressed (HIP) to close internal porosity. Samples were hot isostatically pressed in a commercial unit using typical hip parameters of  $103 \pm 3.4$  MPa at  $1218 \pm 3.9$  °C for 4.25 hrs.

Image analysis of porosity was performed on as-polished longitudinal sections to determine the number and shape of pores in a sample. Images were taken by a CCD camera mounted to the metallurgical microscope and connected to a personal computer. Greyscale 8-bit images from the CCD camera were analyzed using image analysis software. On each image, the threshold was adjusted to remove the light areas and leave only the dark pores. Careful manual control of the image processing assured that carbide shadows were rejected from the

measurements of the pores. Pores under two pixels in size (i.e., approximately 4.7  $\mu\text{m}$  diameter) were rejected. A total of 48 images were captured and analyzed for each sample corresponding to ~40% of the polished area.

Porosity measurements in castings are sometimes made by measuring the density of samples followed by a comparison with the density determined after hot-isostatic-pressing. The density of every 3 mm semicircular sample was measured a minimum of 5 times via Archimedes principle. The samples were carefully measured in air and in absolute ethanol with the temperature monitored by a thermometer.

Qualitative compositions of the primary segregating elements along the length of the samples were determined on transverse cross sections using a JEOL 840 scanning electron microscope with an Oxford Instruments energy dispersive spectroscopy (EDS) system with programming to adjust for atomic number, absorption and fluorescence (ZAF) effects.

Quantitative compositions of the primary segregating elements were determined on selected samples by direct current plasma emission spectrometry. Analyses of hydrogen and nitrogen were performed using the inert gas fusion technique.

### **III. EXPERIMENTAL RESULTS**

*A. Microstructural Characterization:* Figures 3(a-f) are typical transverse (a, c, and e) and longitudinal (b, d, and f) microstructures for the three withdrawal velocities. Transverse micrographs in Figure 3 show that the primary dendritic spacing increases as the withdrawal velocity decreases. The samples shown in Figures 3(c) and 3(d) demonstrate that increased solidification velocities result in secondary and tertiary arm formation to enhance solute

rejection. In Figure 3(e) the microstructure is cellular-dendritic with no secondary dendrite arms as verified by the corresponding longitudinal micrograph, Figure 3(f). When the samples are withdrawn at the highest velocity of 0.1 cm/s, cooling curves from in-situ thermocouples indicated that freezing occurs outside of the adiabatic zone and most of the heat is extracted in the radial direction. Such cooling conditions lead to predominantly dendritic growth inward from the sample surface to the sample centerline as shown in Figure 3(a) and 3(b) and such conditions can produce extensive centerline porosity. Porosity originating from this mechanism was not the focus of this work.

The primary dendrite arm spacings were measured along the lengths of a number of samples and these data are shown in Figure 4. Figure 4 confirms that the experimental setup results in reasonably constant primary dendrite arm spacing over a large portion of the casting lengths. The influence of  $G$  and  $V$  on the primary and secondary dendrite arm spacing have been reported in another publication<sup>13</sup> and will not be repeated here.

*B. Density Measurements:* The density of each semi-circular disc from along the length of each sample was measured to compare the as-cast density against: (1) the as-received density of the original samples, (2) density measurements obtained from selected samples after hot isostatic pressing, and (3) theoretical predictions of the density from measurements of the composition. The as-received density was determined to be 8.57 g/cm<sup>3</sup>. Hot-isostatic-pressing increased the density only slightly to 8.58 g/cm<sup>3</sup>. Figures 5(a-c) show the density vs. position from the bottom to the top of the unidirectionally solidified bars cast under each condition of withdrawal velocity and thermal gradient. The standard deviation of each density determination is included in the figures. All three of the highest velocity samples [Fig. 5(a),  $V=0.1$  cm/s]

exhibited density values near the bottom of the bars that were comparable to the density of the as-received and hot-isostatically-pressed value. However, all three of the highest velocity samples exhibited significant reductions in density values near the top of the bars. As noted above, metallographic examination of the tops of the bars revealed an equiaxed microstructure and significant porosity from the development of extensive centerline shrinkage.

Castings withdrawn at 0.01 cm/s and 0.005 cm/s were considered intermediate velocity samples and their density vs. distance data exhibited similar trends. As shown in Figure 5(b) for the 0.005 cm/s samples, except for three density datapoints near the tops of the bars where preferential cooling out the end (top) of the crucible created a local 'mini-pipe' end-effect, each sample's density was essentially constant along the length of the bar. These density values are comparable to the as-received, hot-isostatically-pressed density value.

The density data shown in Figure 5(c) for samples solidified at  $V=0.0005$  cm/s is extremely interesting. This was the slowest velocity investigated and each sample exhibited a cellular-dendritic microstructure with no secondary arm formation [Fig. 3(e) and 3(f)]. The density of all three samples at each furnace setting exhibited a density at their bottoms comparable to the density of the hot-isostatically-pressed, as-received sample. However, each sample displayed a decreasing density towards the top of the sample. The density of the 1400°C sample remained constant from the bottom to a position of approximately 3-4 cm while the density of the 1500°C sample remained constant from the bottom to a position of approximately 5-6 cm. The density of the 1600°C sample appears to begin to decrease almost from the very beginning of solidification (i.e., bottom of the sample). These decreases in density could be due to one or both of the following: (1) macrosegregation of lighter elements near the top and denser

elements near the bottom of each bar and/or (2) increases in porosity up the bar. These effects will be treated separately next.

*C. Longitudinal Macrosegregation Measurements:* To assess the level of longitudinal macrosegregation present, pieces from along samples grown at velocities of 0.005, and 0.0005 cm/s length were mounted, polished and examined using energy dispersive spectroscopy via the scanning electron microscope. The X-ray data showed that tungsten preferentially segregates to the matrix gamma and that tantalum segregates to the liquid while the remaining elements exhibited partition ratios approximately equal to 1. This behavior is consistent with the segregation analyses of Zeisler-Mashl.<sup>19</sup> The weight percentages of each element were averaged and plotted versus position along the unidirectionally solidified bars in Figure 6 for these two withdrawal velocities. The longitudinal segregation of tungsten and tantalum was greatest in the slowest velocity samples, Figure 6(b), and may influence the density measurements. However, as seen in Figure 6(a), segregation of tungsten and tantalum is not as large in the higher velocity sample and therefore would not influence the measured densities as significantly.

At the slowest velocity of 0.0005 cm/s, there is sufficient time for transport of species by both diffusion and convection in the liquid. The EDS measurements in Figure 6(b) indicate that tungsten is depleted in the liquid (i.e., inverse segregation to  $\gamma$ ) and tantalum is rejected into the liquid as solidification progresses. To further investigate this effect on the 0.0005 cm/s castings, samples from along the length of the castings were carefully analyzed for composition using direct current plasma emission spectroscopy with standards. In addition, selected samples from along the length of the same castings were also hot-isostatically-pressed. The density of the as-cast bars and the as-cast and hot-isostatically-pressed samples are shown in Figure 7. In addition,



the theoretical density based upon the composition of the samples was estimated using the methodology of Sung and Poirier<sup>20</sup> and these data are also shown in Figure 7 for comparison. The as-cast density, the as-cast and hot-isostatically-pressed density, and the theoretical estimate of the density all decrease with distance from the bottom of the cast bars. Thus compositional segregation along the length of the bars significantly lowers the measured density for the samples grown at 0.0005 cm/s.

*D. Metallographic Porosity Characterization:* Extensive metallographic measurements of porosity from the bottom and top regions of bars solidified at  $V=0.005$  and  $0.0005$  cm/s and  $G=25-43^{\circ}\text{C}/\text{cm}$  were also performed. These data are shown in Figures 8(a) and 8(b). Figure 8(a) shows low levels of porosity along the length of the bars until centerline shrinkage occurs at the tops of three bars where the porosity values are greater than 1%. The porosity scale is expanded in Figure 8(b) and shows the measured variation of microporosity for the six samples -- porosity levels greater than 0.5% were eliminated from the data sets to minimize the influence of centerline shrinkage. These microporosity data exhibit considerable scatter that is typical of porosity data in general.

Table III shows the means and standard deviations for the microporosity data shown in Figure 8(b). All samples solidified at 0.005 cm/s exhibited less microporosity than the corresponding samples solidified at 0.0005 cm/s. Analyses of the means by the Welch Test<sup>21</sup> indicate that this conclusion is highly significant at the 99% confidence level for both the top and bottom regions of all samples except only the top of the samples solidified using a furnace setting of  $1400^{\circ}\text{C}$ . The reductions in porosity average approximately 55% by increasing the solidification velocity from 0.0005 to 0.005 cm/s. Comparison of the standard deviations ( $\sigma$ ) of

porosity between the 0.005 and the 0.0005 cm/s samples shows that the 0.005 cm/s samples typically exhibit less scatter than the 0.0005 cm/s samples. Analysis of the variances ( $\sigma^2$ ) by the "F" test indicates that this conclusion is correct at the 99% confidence level for the tops and bottom of the samples except for the top region of samples cast using a furnace setting of 1400°C. Figures 9(a) and 9(b) show the population distributions for pore radii for the 0.005 and 0.0005 cm/s samples cast using all three furnace settings (1400-1600°C). Clearly, the higher velocity samples exhibits a larger number of smaller pores than the lower velocity samples.

The influence in thermal gradient (i.e., furnace setting) on porosity levels was not as clear. Statistically significant reductions in porosity due to an increase in thermal gradient were exhibited at the 95% confidence level only for the bottom regions of samples solidified at velocities of 0.005 and 0.0005 cm/s.

Even more unclear is any potential difference between the bottom and the top regions of castings. Although Figure 8(a) shows a clear propensity for large levels of macroporosity due to centerline shrinkage, the microporosity data of Table III and Figure 8(b) exhibit no statistically significant distinction between the amount of microporosity in the bottom regions of bars versus the top regions of samples. However, analysis of the variances by the "F" test shows that the scatter in the data is greater in the tops of the samples than the bottom of the samples at the 99% confidence level. The population of pores in the tops of the bars may be composed of a bimodal distribution of micropores and incipient cases of macropores, perhaps from the beginning of centerline shrinkage. Additional investigation of the transition from aligned axial dendritic growth to misaligned and radial dendritic growth is required to assess this possibility.

#### IV. DISCUSSION

##### A: *High Velocity Samples: $V_s=0.1$ cm/s*

The samples withdrawn at 0.1 cm/s did not exhibit aligned directional solidification since the withdrawal velocity was too high for solidification to be completed within the adiabatic zone.

Heat extraction was principally from the sides of the cylindrical samples and the dendrites grew radially inward. Near the top of each of these samples, extensive macroporosity developed to form severe centerline shrinkage. Porosity of this type can be interpreted from the simplified geometrical model of Sigworth and Wang<sup>1</sup>. As shown in Figure 10, withdrawal velocities too high to enable directional solidification will induce radial dendritic growth and created a tapered liquid feeding channel down through the center of the bar. Such a tapered channel can be characterized by an angle and molten metal feeding could be assumed to occur as long as the angle was greater than a certain critical angle  $\theta_c$ . As noted by Sigworth and Wang, local variations in the contraction of the casting from the mold and the orientations of the radially growing grains would cause uneven solidification and allow isolated 'pools' of liquid metal to freeze without feeding and exhibit shrinkage.

##### B. *Low Velocity Samples: $V_s=0.0005$ cm/s*

The castings withdrawn at velocities less than 0.1 cm/s all exhibited aligned growth of dendrites and/or cellular-dendrites as shown schematically in Figure 1. As noted above, the decrease in density from the bottom towards the top of the 0.0005 cm/s bars was principally due to macrosegregation effects and not porosity. However, as shown in Figures 8(b) and 9(b), microporosity certainly forms in the 0.0005 cm/s samples to overall levels of approximately 0.1-0.4%

A straightforward capillary flow analysis of the 0.0005 cm/s samples provides insight into the pore formation processes. The lack of secondary arms enables the interdendritic spaces of

the 0.0005 cm/s samples to be approximated as capillary tubes. This is an important aspect of the cellular-dendritic growth since it obviates the necessity of evaluating the transient permeability of a tortuous mushy zone during solidification and greatly simplifies calculation of pressure drops through the mushy zone. Figure 11(a) shows a lightly etched transverse section through a sample solidified at 0.0005 cm/s and a thermal gradient of 38 °C/cm. The smallest interdendritic regions are circular in shape and exhibit typical diameters from 20-40  $\mu$ m. Equation [3] was utilized to theoretically predict the pressure drop through the mushy zone by assuming that the interdendritic spaces formed small circular 'pipes' through which liquid metal flowed to feed solidification at the eutectic temperature. The thermophysical property and relevant process data utilized for Mar-M247 are shown in Table III. Calculations were performed for a range of solidification velocities from 0.0005 – 0.05 cm/s and the predicted local pressures in the bottom of the mushy zone are presented in Figure 11(b). The maximum local pressure is shown as  $P_o + \rho gh$ . Note that the metallostatic head only increases the maximum local pressure by approximately 10 kPa (or 10% of one atmosphere). At the experimental velocity utilized here (0.0005 cm/s), the local pressure is predicted to remain positive unless the capillary diameter decreases to 0.1  $\mu$ m. This value is approximately two orders of magnitude smaller than the interdendritic sizes exhibited by the samples and the corresponding pore diameters. Higher velocities of 0.05 cm/s are theoretically shown to require capillary diameters of the order of 1  $\mu$ m before the local pressures are predicted to be negative. Thus the presence of capillary flow does little to reduce local pressures and facilitate pore formation.

The segregation of dissolved gases and precipitation of gas bubbles can play a dominant role in formation of porosity. The gas pressure  $P_G$  due to rejection of dissolved gases was calculated following the work of Sung *et.al.*<sup>22</sup> utilizing the equivalence method developed by Schurmann *et.al.*<sup>23</sup> Sievert's law was used to calculate  $P_G$  as follows:

$$K_H = \frac{C_H f_H}{(P_{H_2})^{1/2}} \quad [4]$$

where  $C_H$  is the hydrogen concentration in weight %,  $K_H$  is the equilibrium constant,  $f_H$  is the activity coefficient and  $P_{H_2}$  is the local pressure of hydrogen gas in equilibrium with the hydrogen dissolved in the liquid. The activity of hydrogen in liquid Mar-M247 was estimated as

$$\ln f_H = d_x \theta + f_x \theta^2 + (e_x \theta + g_x \theta^2)/T \quad [5]$$

where

$$\theta = \sum_{i=1}^N b_H^i X^i \quad [6]$$

and  $d_x$ ,  $f_x$ ,  $e_x$ ,  $g_x$ , and  $b_H^i$  are constants obtained from Schurmann *et.al.*<sup>22</sup> and given in Table IV for both hydrogen and nitrogen;  $X^i$  is the atomic fraction of element  $i$  and  $T$  is temperature in Kelvin.

The Sieverts' equilibrium constants<sup>23</sup> for hydrogen and nitrogen are

$$\ln K_H = -4.154 - \frac{2613}{T} ; \quad \ln K_N = -4.106 - \frac{4972}{T} . \quad [7]$$

Figure 12 plots the results of calculations of gas pressures at the eutectic temperature for hydrogen and nitrogen for a wide range of gas contents. The gas pressure in the liquid is seen to be highly influenced by the amount of hydrogen in the samples; the influence of nitrogen on the gas pressure is minimal and can be neglected. Brandes<sup>24</sup> gives a partition coefficient for hydrogen in pure nickel as  $k=0.44$  which would produce an interdendritic liquid hydrogen content of 2.3 times the average alloy composition. Assuming that hydrogen segregation in Mar-M247 is similar to pure nickel means that hydrogen levels of 5-11 ppm in the bulk alloy would yield values from 11-25 ppm hydrogen in the interdendritic liquid. Figure 12 shows that these interdendritic hydrogen contents at the eutectic temperature would produce equivalent gas pressures of 65-350 kPa. Such high local gas pressures would greatly assist nucleation of porosity in these samples.

Chen *et.al.*<sup>25</sup> note that carbides can heterogeneously nucleate in nickel-based superalloys

at temperatures from within the mushy zone to temperatures higher than the liquidus depending upon the nucleation potential of the liquid. During the low velocity cellular-dendritic solidification of MAR-M247 LC alloy, Chen *et.al.*<sup>25</sup> found that carbides tend to become preferentially trapped by the advancing solid at the bottom of the mushy zone. This observation is consistent with the present series of samples. This is not surprising since the density of the liquid is 7.4 g/cm<sup>3</sup> and the density of HfC, TaC, and W<sub>2</sub>C are 12.7 g/cm<sup>3</sup>, 14.5 g/cm<sup>3</sup>, and W<sub>2</sub>C is 17.2 g/cm<sup>3</sup>, respectively.<sup>19</sup> Thus carbides nucleating in the enriched interdendritic liquid would tend to settle to the bottom of the mushy zone. Figure 14 is a SEM micrograph showing an interdendritic carbide particle associated with porosity (behind it with respect to the direction of dendritic growth). The extensive metallographic characterization of porosity in this investigation revealed that a high percentage of pores were located adjacent to carbide particles. This close association of porosity with carbides suggests that the particles may be settling to the bottom of the interdendritic spaces during cellular-dendritic growth and block off the feeding path to feed the final solidification at the eutectic temperature. Thus interdendritic carbides may create isolated micropools of liquid metal than then become micropores during final solidification. Additional studies with varying amounts of carbon and carbide forming elements are required to test this possibility.

### *C. Intermediate Velocity Samples: $V_s=0.005$ cm/s (and 0.01 cm/s)*

Interestingly, none of the samples withdrawn at 0.005 cm/s exhibited significant density variation with position along the length of the bars. Perhaps the decreased permeability of the mushy zone due to secondary and tertiary arm development prevented significant penetration of bulk convection into the mushy zone and allowed microsegregation to develop in a quiescent liquid. Additional studies utilizing computational models of the present experiments are necessary to quantify this effect.



The secondary and tertiary arm development of the 0.005 cm/s samples also prevented significant growth of micropores resulting in a larger number of smaller pores as compared to the 0.0005 cm/s samples. Since the volume of each isolated pore would scale as  $d^3$ , reducing the size of pores dramatically reduces their effect on the measured porosity and density of any given sample. As noted above, Bachelet<sup>16</sup> *et. al.* proposed that there should be optimum casting conditions between fast and slow cooling leading to small evenly distributed micropores. These conditions appear to have been met for the samples withdrawn at 0.005 cm/s.

## V. CONCLUSIONS

(1) As originally proposed by Bachelet<sup>16</sup> *et. al.*, there appears to be an optimum directional solidification velocity for MAR-M247 of 0.005 – 0.01 cm/s that leads to small evenly distributed micropores with the minimum total porosity. Micropore growth appears to be limited by the isolating effects of secondary and tertiary dendritic arms.

(2) Directional solidification velocities higher than 0.01 cm/s for MAR-M247 in the present apparatus enable solidification outside of the adiabatic zone, radial dendritic growth, and severe centerline shrinkage.

(3) Directional solidification velocities for MAR-M247 lower than 0.005 cm/s lead to cellular-dendritic solidification, greater levels of overall porosity, and a smaller number of larger pores than at higher velocities. In addition, greater levels of axial macrosegregation are found in these samples as compared to the higher withdrawal velocity samples. The macrosegregation levels are great enough to significantly impact density measurements of the castings.

(4) Applied thermal gradients of 19-34°C/cm for MAR-M247 in the present apparatus do not appear to exert significant influence on either macrosegregation or porosity.

(5) Dissolved hydrogen levels of 5-11 ppm in the bulk alloy can produce local hydrogen

gas pressures from 65-350 kPa in the interdendritic regions.

(6) Carbides appear to be highly associated with micropores in MAR-M247. Further studies are required to assess the statistical significance of this association and any possible implications regarding cause and effect.

### Acknowledgments

This material is based upon work supported by, or in part by, the U.S. Army Research Office under grant number ARO DAAHO4-96-I-0321 and the National Aeronautics and Space Administration under cooperative agreement number NCC8-128. The samples were graciously provided by Howmet Corporation, Whitehall, MI. Technical discussions and the assistance of Dr. Boyd Mueller and Mr. Terry Simon of Howmet Corporation in preparing the investment cast precursor bars are especially appreciated.

### REFERENCES:

1. G.K. Sigworth and C. Wang: *Met. Trans.*, 1993, vol 24B, pp. 349-364.
2. J. Lecomte-Beckers: *Met. Trans.*, 1988, vol. 19A, pp. 2341-2348.
3. S.T. Kao, E. Chang and Y.W. Lee: *Mat. Sci. Tech.*, 1995, vol 11, pp. 933-938.
4. C.S. Chin and J.A. Sekhar: *J. Mat. Sci.*, 1994, vol 29, pp. 5005-5013.
5. C.T. Ho, C.J. Cheng and J.A. Sekkar: *Met. Trans.*, 1991, vol 22A, pp. 225-234.
6. T.S. Piwonka and M.C. Flemings: *Trans AIME*, 1966, vol 236, pp. 1157-1165.
7. J.K. Tien and R.P. Gamble: *Mater. Sci. Engrg.*, 1971, vol 8, pp. 152-160.
8. J.D. Hunt: *Solidification and Casting of Metals*, The Metals Society, London, 1979, pp. 3-9.
9. W. Kurz and D.J. Fisher: *Acta Metall.*, 1981, vol 29, pp. 11-20.
10. D. Bouchard and J.S. Kirkaldy: *Metall. Mat. Trans.*, 1997, vol 28B, pp. 651-663.
11. D. Ma and P.R. Sahm: *Metall. Mat. Trans.*, 1998, Vol. 29A., pp. 1113-1119.
12. J.D. Hunt and S.Z. Lu: *Met. Trans.*, 1996, Vol. 27A., pp. 611-623.
13. H.S. Whitesell, L. Li and R.A. Overfelt: *Metall. Mater. Trans.*, 2000, vol 31B, pp. 546-551.
14. D.R. Poirier: 1987, *Met. Trans.*, Vol. 18B, pp. 245-255.
15. B. Goyeau, T. Benihaddadene, D. Gobin, and M. Quintard: 1999, *Metall. Mater. Trans.*, Vol. 30B, pp. 613-622.
16. E. Bachelet and G. Lesoult: *High Temperature Alloys for Gas Turbines* (ed. D Coutsouradis), Applied Science, London, 1978, pp. 665-699.
17. M. Vijayakumar, S.N. Tewari, J.E. Lee and P.A. Curreri: *Mater. Sci. Engrg.*, 1991, vol A132, pp. 195-201.
18. D.G. McCartney and J.D. Hunt: *Acta Metall.*, 1981, vol 29, pp. 1851-1863.

19. K.L. Zeisler-Mashl, Ph.D. Dissertation, 1992, Michigan Technological University, Houghton, MI
20. P.K. Sung and D.R. Poirier: *Mater. Sci Engrg.*, 1998, vol A245, pp. 135-141.
21. C. Mack: *Essential of Statistics for Scientists and Technologists*, 1975, Plenum, New York, pp. 47-49.
22. PK Sung, DR Poirier, SD Felcelli, EJ Poirier and A Ahmed, 2000, personal communication.
23. E Schurmann, M Sittard and R Volker: *Z Metallkd*, 1987, vol 78, pp. 457-466.
24. E.A. Brandes: *Smithells Metals Reference Book*, Butterworths, London, 1983, p. 12-5.
25. J. Chen, J.H. Lee, C.Y. Jo, S.J. Choe, and Y.T. Lee: *Mater. Sci. Engrg.*, 1998, Vol. A247, pp. 113-125.
26. Boyd Mueller, Howmet Corporation: 1999, personal communication.
27. P. Bannerjee and R.A. Overfelt: *Intl. J. Thermophysics*, 1999, Vol. 20, No. 6, pp. 1791-1800.
28. E.A. Brandes, *ibid*, p. 14-7.

## List of Tables

- I. Composition of the Samples Utilized in this Investigation
- II. Statistical Data on Metallographic Measurements of Porosity in Samples Withdrawn at 0.005 and 0.0005 cm/s
- III. MAR-M247 Thermophysical Property Data
- IV. Hydrogen and Nitrogen Activity Coefficients

Table I

**Composition of the Samples Utilized in this Investigation**

Element	Ni	W	Co	Cr	Al	Ta	Hf	Ti	Mo	C	Zr	B	H	N
Wt. %	bal.	10.0	10.1	8.35	5.7	3.07	1.23	0.99	0.80	0.16	0.045	0.015	0.0008	0.0022

Table II

**Statistical Data on Metallographic Measurements of Porosity in Samples Withdrawn at 0.005 and 0.0005 cm/s**

V (cm/s)	G (C/cm)	Bottom of sample			Top of Sample		
		n	mean	$\sigma$	n	mean	$\sigma$
0.0005	26	55	0.21	0.20	39	0.23	0.31
0.0005	38	52	0.19	0.18	50	0.19	0.21
0.0005	43	58	0.13	0.14	58	0.22	0.25
0.005	25	59	0.10	0.086	53	0.17	0.46
0.005	35	57	0.050	0.046	42	0.084	0.12
0.005	40	60	0.070	0.056	58	0.046	0.030

Table III

**Properties of MAR-M247 Used in the Calculations**

Property	Value	Reference
Liquid density, $\rho_L$ (g cm <sup>-3</sup> )	7.43	26
Solid density, $\rho_S$ (g cm <sup>-3</sup> )	7.95	26
Viscosity, $\mu$ (mPa s)	8.5	27
Surface tension, $\sigma_{LV}$ (N m <sup>-1</sup> )	1.7	28
Liquidus Temperature (K)	1628	26
Eutectic Temperature (K)	1549	26

Table IV  
Hydrogen and Nitrogen Activity Coefficients

Property	Hydrogen	Nitrogen
$d_x$	-2.97302	18.8573
$f_x$	0.008199	-34.8763
$e_x$	12956.4	-70200.4
$g_x$	18495.6	89008.10
Element	$b_H^i$	$b_N^i$
Co	0.171	0.0642
Al	0.47	-0.354
Ti	-0.075	2.83
Ta	0.52	0.85
Mo	0.334	0.86
W	0.52	0.85
Cr	0.143	1
Hf*	0.52	0.85

\*Estimated from Ta and W

## List of Figures

1. Schematic of aligned dendritic and cellular growth
2. Schematic of the directional solidification apparatus utilized in this investigation
3. Typical microstructures of directionally solidified samples
  - a, b:  $V = 0.1$  cm/s,  $G = 19$  °C/cm (transverse and longitudinal, respectively)
  - c, d:  $V = 0.005$  cm/s,  $G = 39$  °C/cm (transverse and longitudinal, respectively)
  - e, f:  $V = 0.0005$  cm/s,  $G = 43$  °C/cm (transverse and longitudinal, respectively)
4. Primary dendritic spacing along selected sample lengths
5. Density along the sample length for samples withdrawn at:
  - a. 0.1 cm/s
  - b. 0.005 cm/s
  - c. 0.0005 cm/s
6. Longitudinal segregation measurements (wt. %) for a sample withdrawn at:
  - a. 0.005 cm/s
  - b. 0.0005 cm/s
7. Comparison of density measurements and theoretical predictions of density from local composition measurements along the length of samples withdrawn at 0.0005 cm/s
8.
  - a. Metallographic measurements of porosity for samples withdrawn at 0.005 and 0.0005 cm/s
  - b. Metallographic measurements of porosity for samples withdrawn at 0.005 and 0.0005 cm/s (expanded scale)
9. Distribution of pore sizes for samples withdrawn at (a) 0.005 cm/s and (b) 0.0005 cm/s.
10.
  - a. Cross section of a vertical bar casting where the presence of an axial thermal gradient creates a tapered liquid pool in the center to feed the casting (after Sigworth and Wang<sup>1</sup>)
  - b. Cross section of a vertical bar casting where lack of an axial thermal gradient and uneven freezing leaves isolated pools of liquid
11.
  - a. Lightly etched transverse cross section near the eutectic freezing isotherm of a quenched DS sample showing the interdendritic spaces available to feed final solidification ( $V = 0.0005$  cm/s,  $G = 41$  °C/cm)
  - b. Calculations of the local pressure due to capillary flow through assumed cylindrical interdendritic spaces for the withdrawal velocities shown.
12. Theoretical predictions of pressure at the eutectic temperature due to rejection of dissolved hydrogen and nitrogen.
13. Typical as-cast pores associated with large carbide particles.

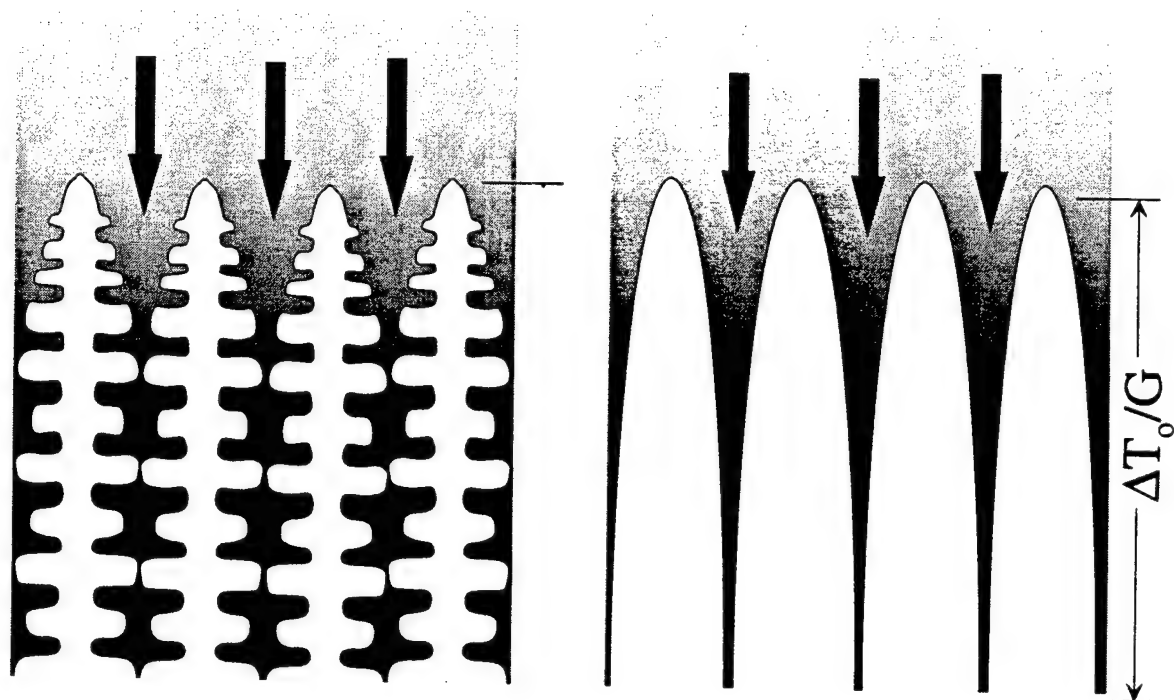


Figure 1



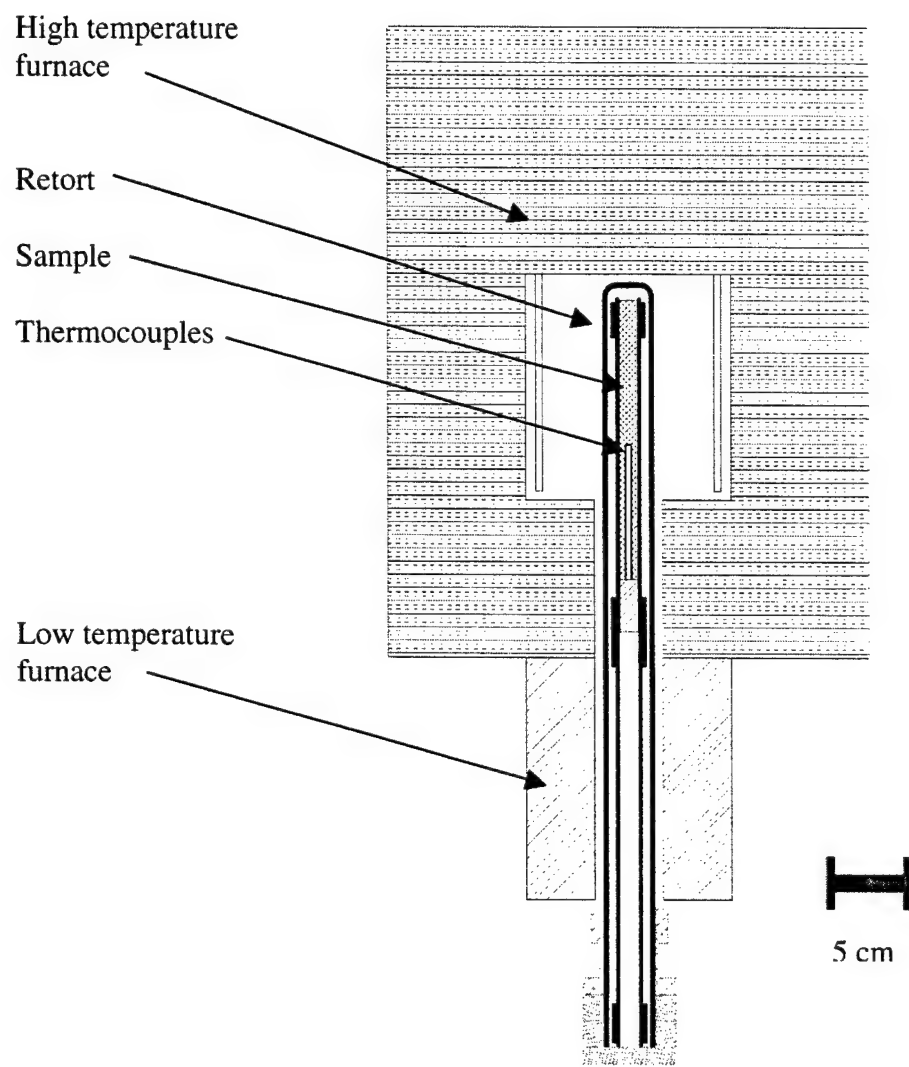


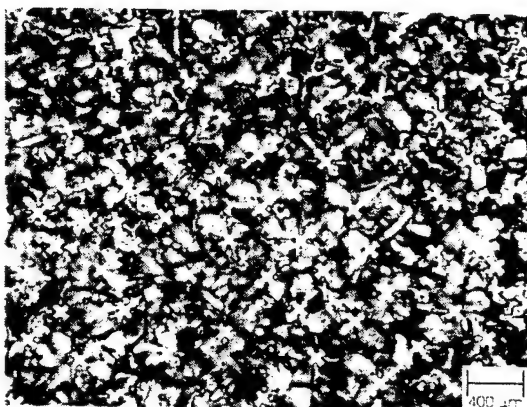
Figure 2



(a)



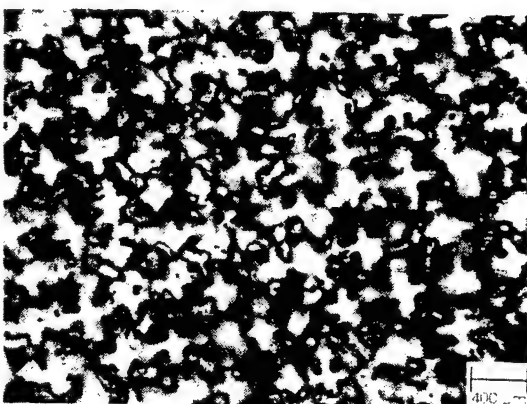
(b)



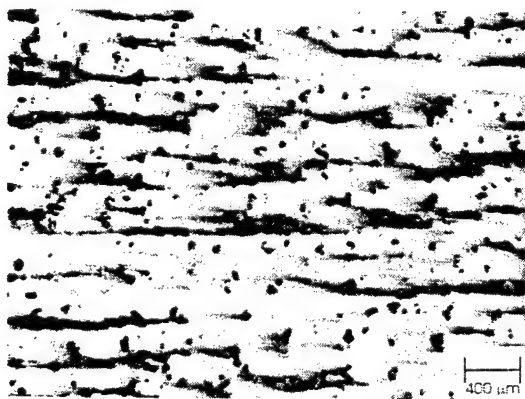
(c)



(d)



(e)



(f)

Figure 3

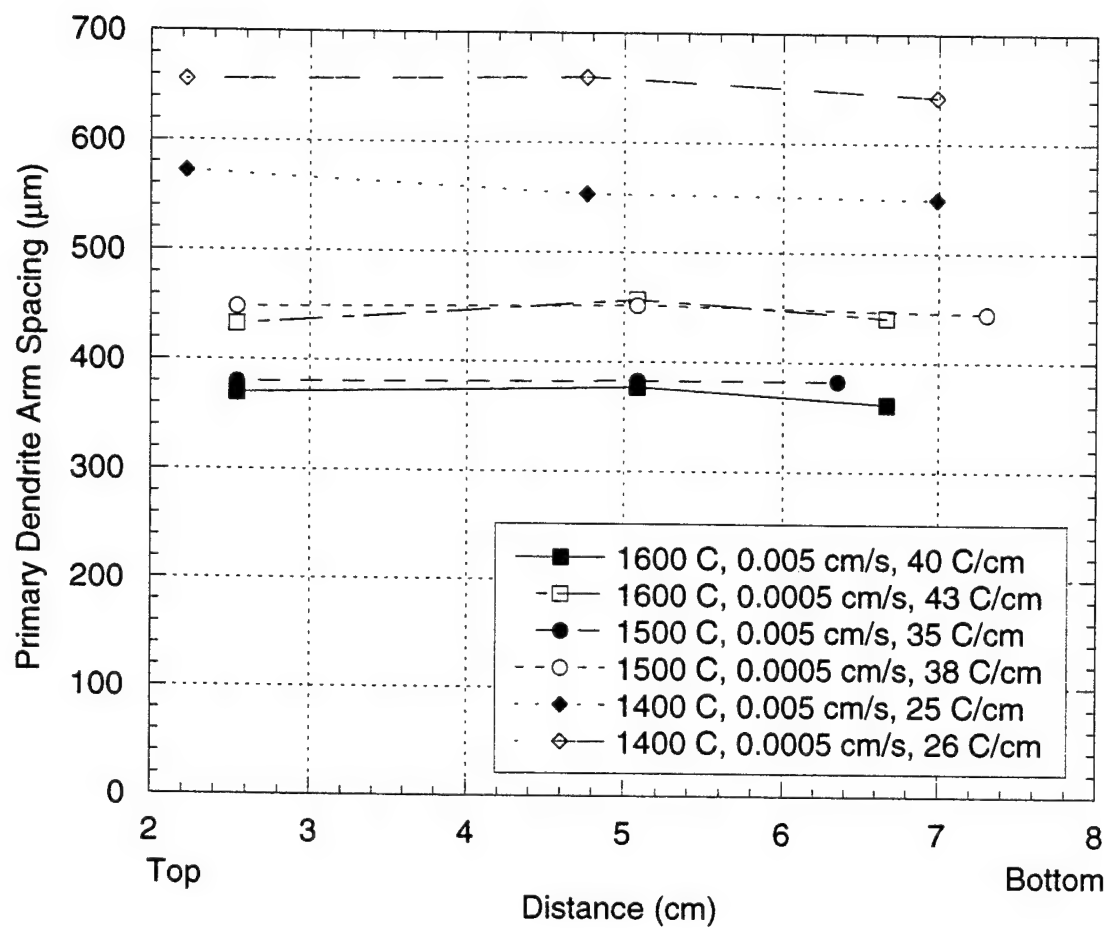


Figure 4

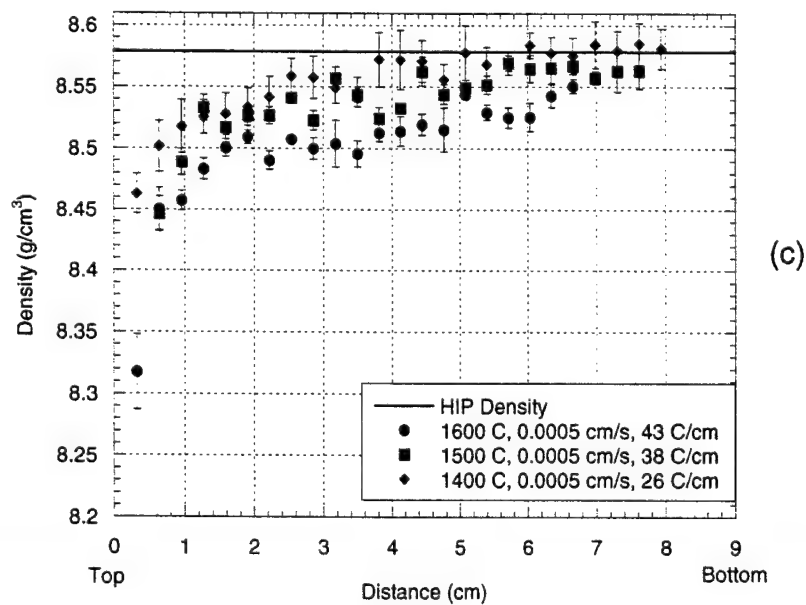
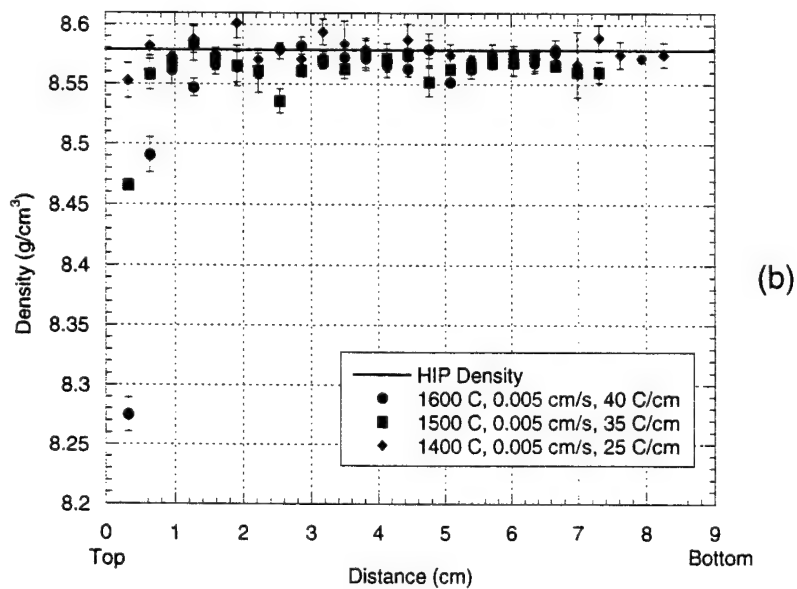
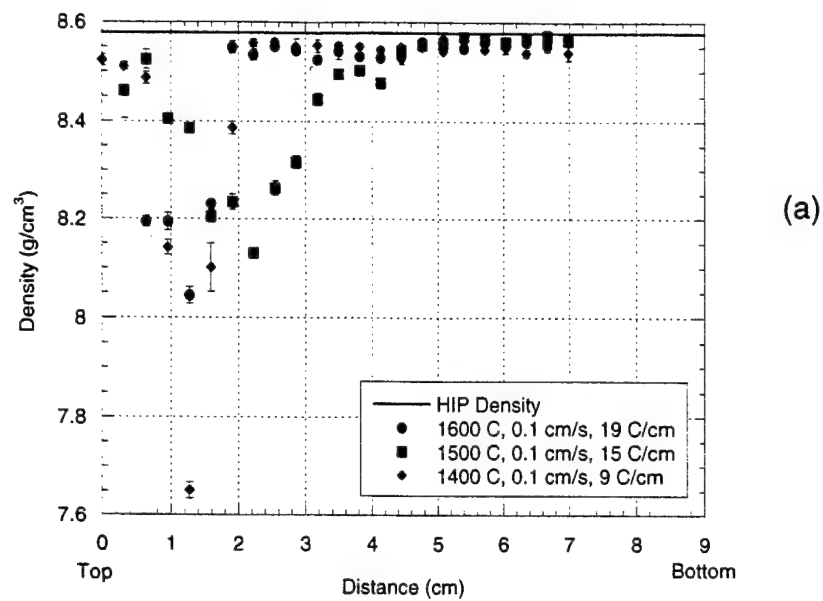
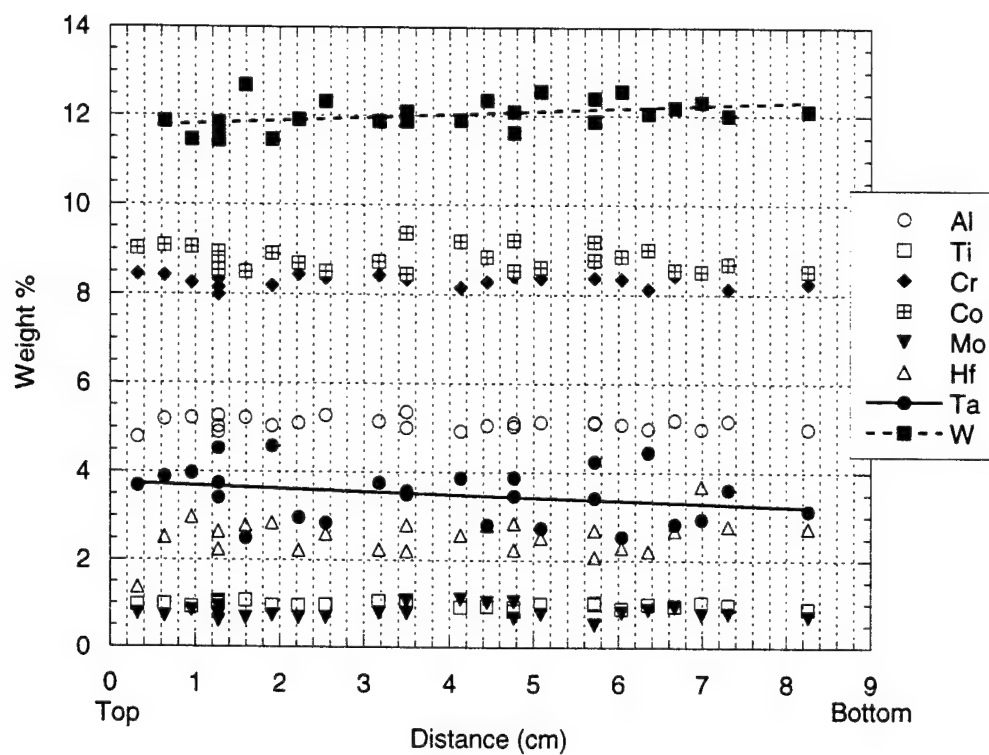
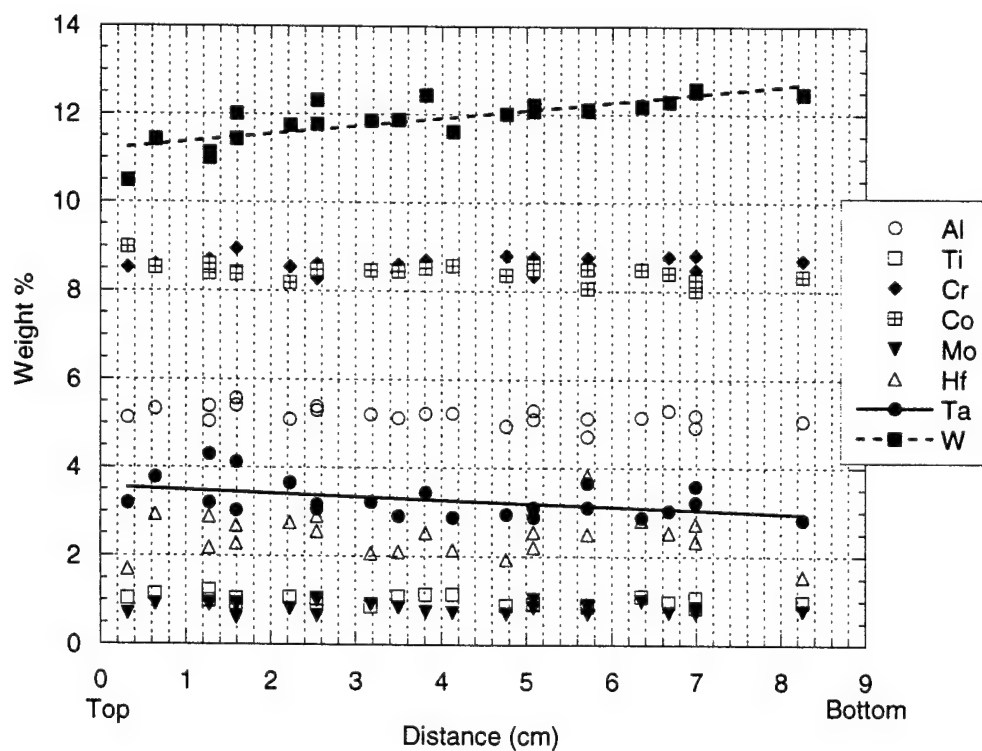


Figure 5



(a)



(b)

Figure 6

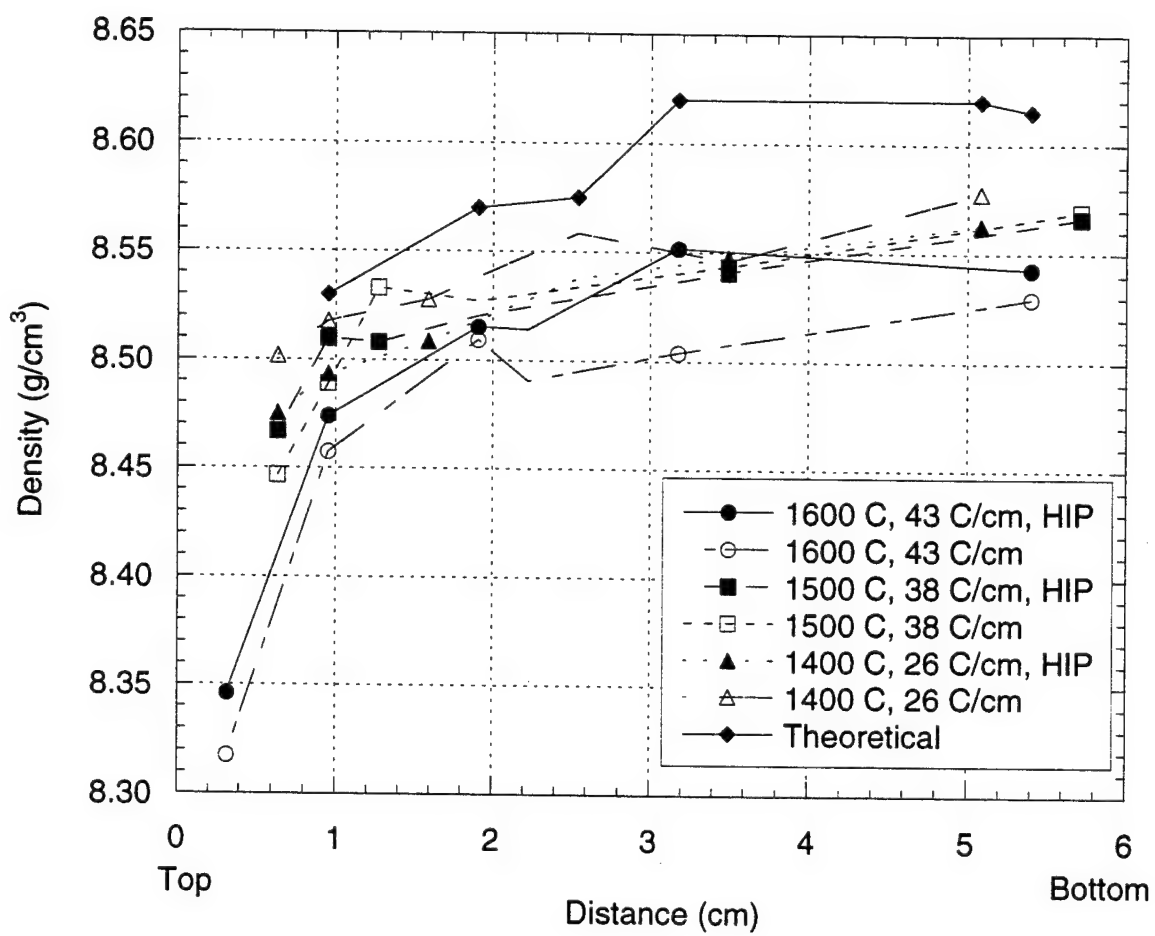
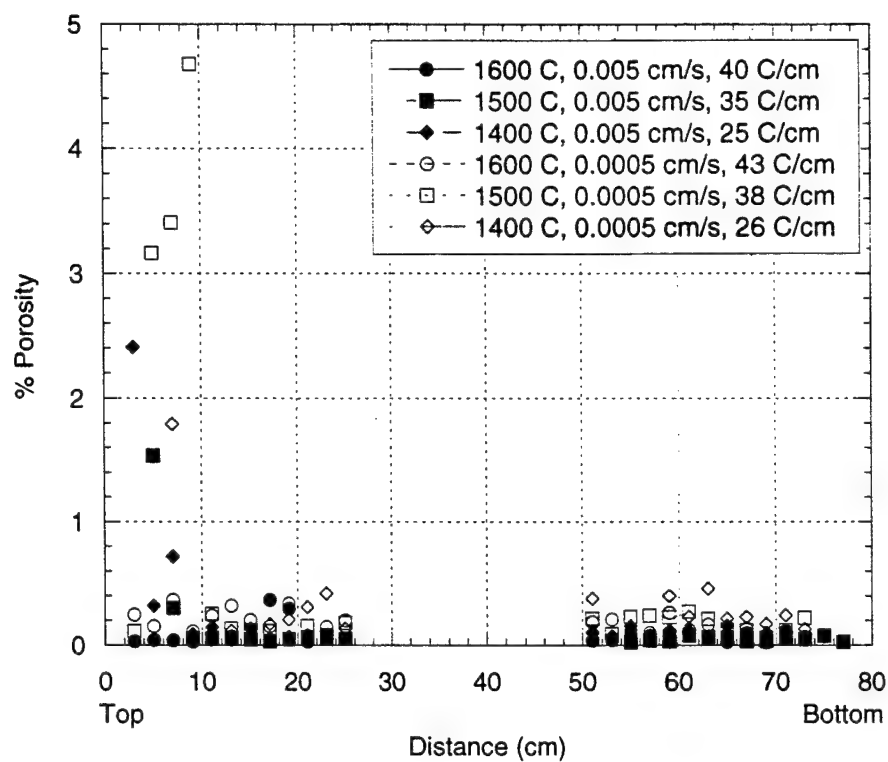
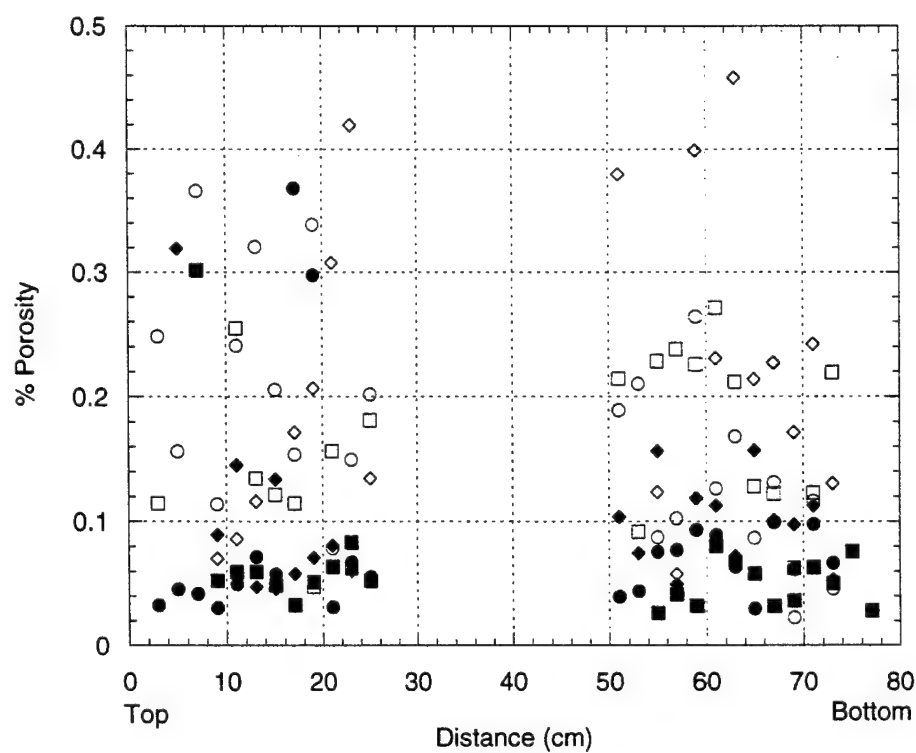


Figure 7



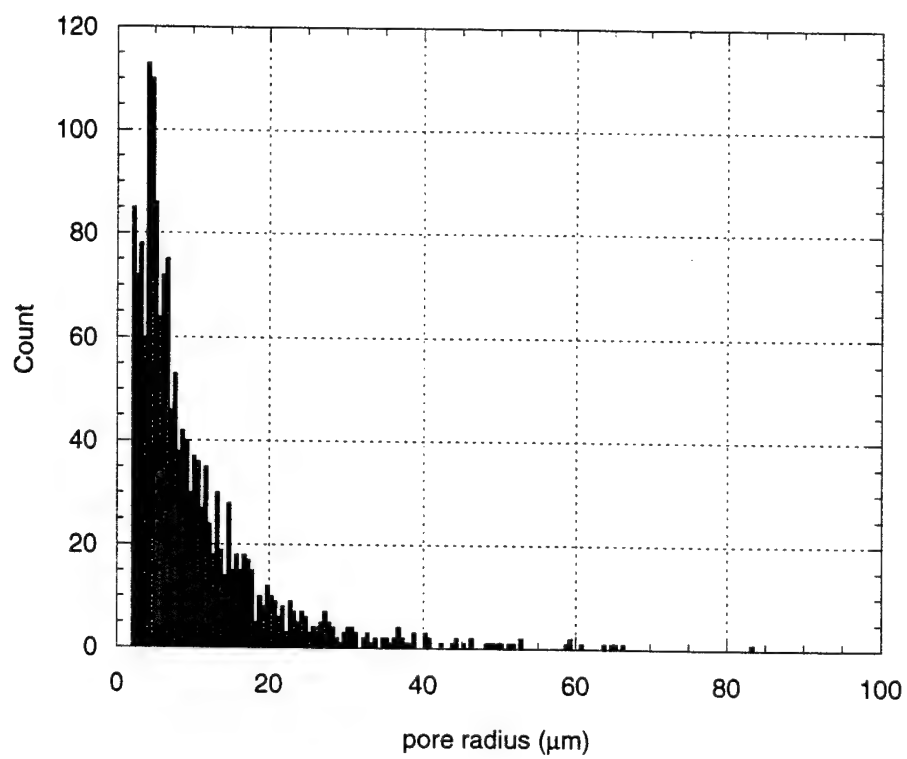
(a)



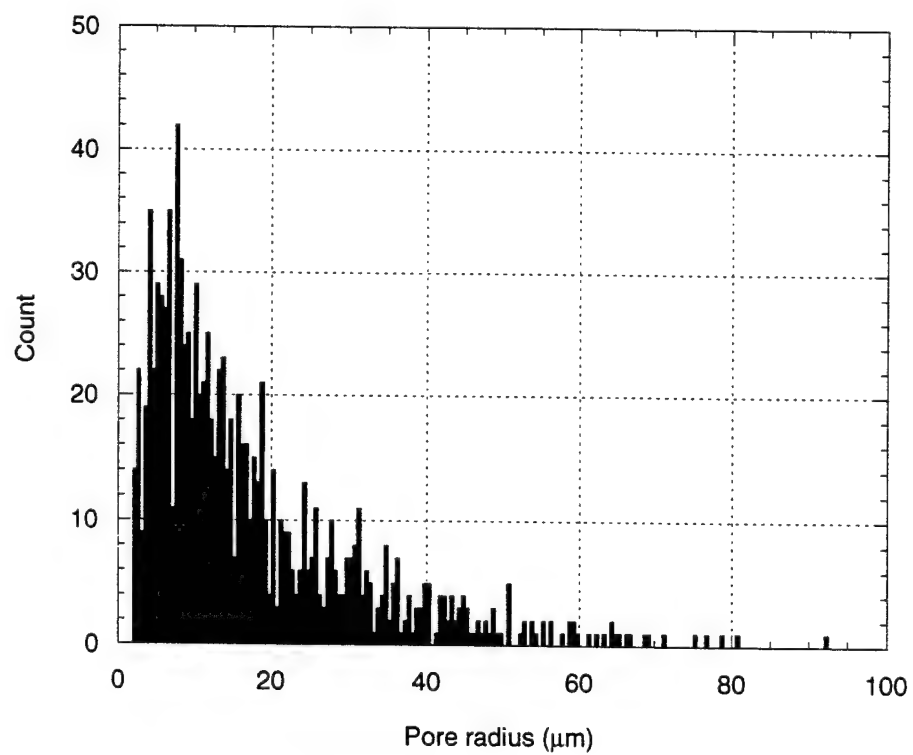
(b)

Figure 8





(a)



(b)

Figure 9

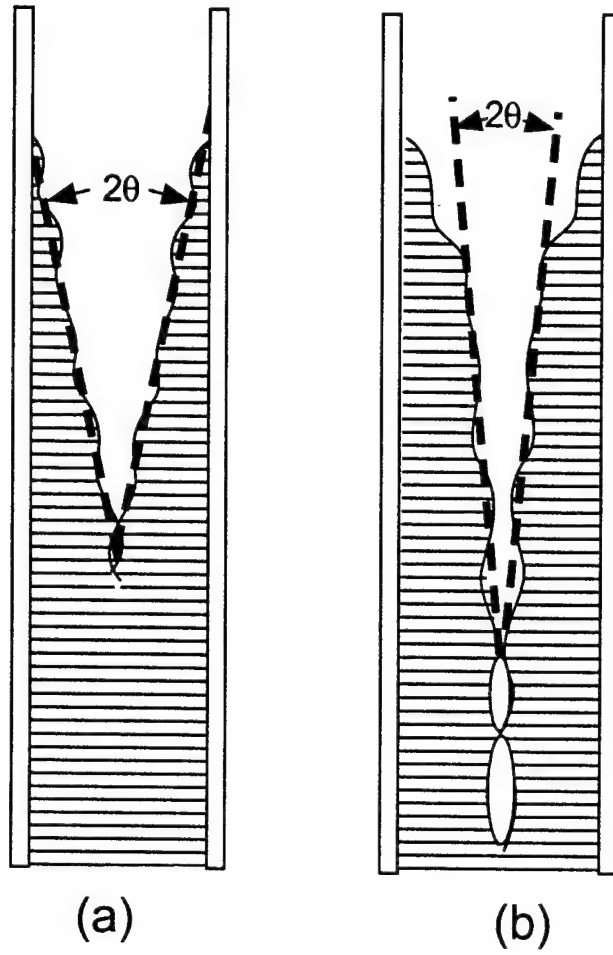
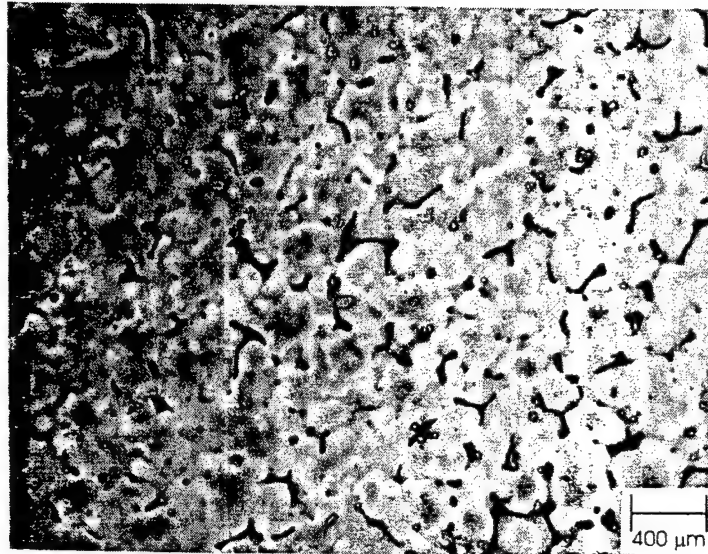
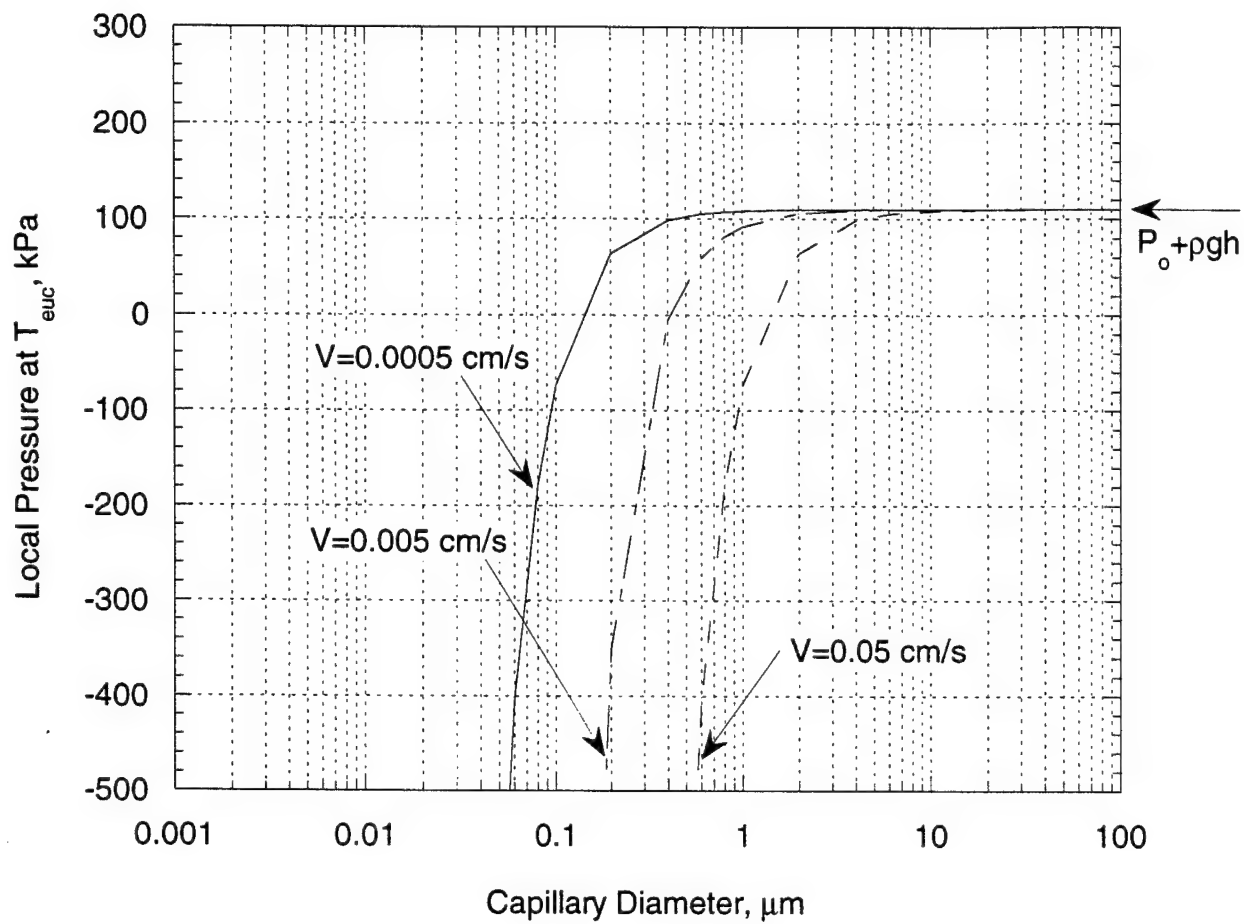


Figure 10



(a)

Figure 11



(b)

Figure 11

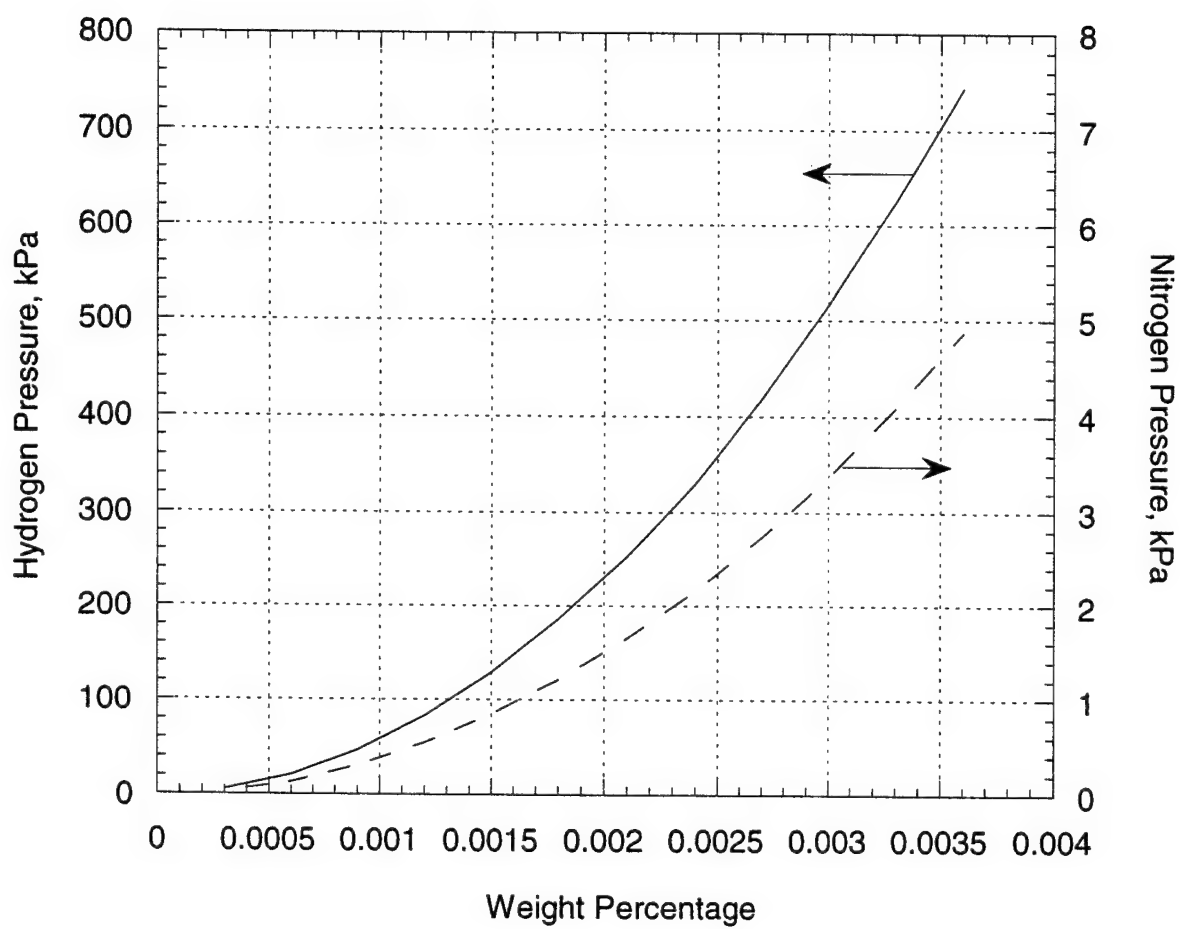


Figure 12



(a)



withdrawal velocity (b)

— 10  $\mu\text{m}$

Figure 13

## **Influence of Directional Solidification Variables on the Cellular and Primary Dendrite Arm Spacings of PWA1484**

Lichun Li and Ruel A. Overfelt  
Mechanical Engineering Department  
Materials Engineering Program  
Auburn University  
201 Ross Hall  
Auburn, AL 36849

### **Abstract**

A series of directional solidification experiments have been performed to elucidate the effects of thermal gradient  $G$  and growth velocity  $V$  on the solidification behavior and microstructural development of the multicomponent Ni-base superalloy PWA 1484. The primary arm spacings that developed in the Bridgman-grown samples are examined in terms of current theoretical models of the effects of the process parameters. A range of aligned solidification microstructures were exhibited by the alloy when examined as-cast at room temperature: aligned dendrites with well developed secondary and tertiary arms; flanged cells aligned with the growth direction and without secondary arms; and cells with no evidence of flanges or secondary arms. The presence of secondary arms increases the spacings between dendrites and leads to a greater sensitivity of  $\lambda_1$  on  $G^{-1/2}V^{1/4}$ . Under conditions of high longitudinal thermal gradients ( $G > 30\text{K/cm}$ ), only negligible radial thermal gradients were found in the samples. For such experimental conditions, the primary dendrite arm spacings ( $\lambda_1$ ) were well described by the theoretical model of Ma and Sahm. However, at low longitudinal thermal gradients ( $G < 30\text{K/cm}$ ), significant radial thermal gradients were found in the directionally solidified samples. These radial gradients enhanced the growth of secondary arms and increased the primary arm spacings necessitating a modification of the theoretical relationship for primary dendrite arm spacings by a geometrically-based empirical factor.



## I. Introduction

The columnar arm spacings of directionally solidified materials are very important microstructural features that impact basic transport phenomena in the mushy zone and the subsequent mechanical properties of cast products. The dendrite arm spacings and morphology directly influence convection in the mushy zone and dominate the occurrence of grain defects, freckle/channel segregates and porosity in the microstructure.<sup>[1-3]</sup> Thus the variation of primary dendrite arm spacings during directional solidification has been intensively studied<sup>[4-10]</sup>. Although the fundamental phenomena of microstructural development and transition (i.e., planar interface→cells→dendrites→equiaxed grains) are qualitatively understood, there is still work to do to quantitatively describe multi-component systems, growth with mis-aligned thermal fields, and growth during transient thermal conditions.

Hunt<sup>[11]</sup> developed the first theoretical formulation to predict dendrite arm spacings based upon the imposed process parameters. In Hunt's model, several assumptions were invoked to simplify the treatment: 1) the thermal and compositional gradients in the direction vertical to the growth direction were constant; 2) the tip of the dendrite or cell was a steady parabolic shape; and 3) the cell or dendrite grew at the minimum undercooling for a given growth velocity (or maximum growth velocity). Hunt's model resulted in a relationship of the form:

$$\lambda_1 = \left\{ 2.83 \left( \frac{\gamma D}{\Delta S} \right)^{1/4} \left[ m(1-k)C_0 + \frac{kGD}{V} \right]^{1/4} \right\} G^{-1/2} V^{-1/4} \quad (1)$$

The first term in the braces { } is primarily a combination of material constants for a given alloy.  $\gamma$  is the alloy solid-liquid interfacial energy,  $D$  is the solute diffusion coefficient,  $\Delta S$  is entropy of fusion per unit volume,  $m$  is the slope of the liquidus,  $k$  is the solute distribution coefficient and  $C_0$  is the alloy composition.  $G$  and  $V$  are the longitudinal thermal gradient and growth velocity at the aligned dendrite tip, respectively.

Two years later Kurz and Fisher<sup>[12]</sup> published a modified theoretical model utilizing the stability criterion proposed by Langer and Muller-Krumbhaar.<sup>[13]</sup> In addition, Kurz and Fisher

assumed the tips of the cells/dendrites were smooth ellipsoids and the cells/dendrites form uniform hexagon arrays. Thus, Kurz and Fisher obtained the following results for cells and dendrites:

$$\text{Cells:} \quad \lambda_1 = \left[ \frac{6\Delta T'}{G(1-k)} \right]^{1/2} \left[ \frac{D}{V} - \frac{k\Delta T_0}{G} \right]^{1/2} \quad (2)$$

$$\text{Dendrites:} \quad \lambda_1 = 4.3 \{ \Delta T'^2 \frac{\Gamma D}{k\Delta T_0} \}^{1/4} G^{-1/2} V^{-1/4} \quad (3)$$

where  $\Gamma$  is the Gibbs-Thomson coefficient and  $\Delta T'$  and  $\Delta T_0$  are the non-equilibrium and equilibrium freezing ranges, respectively. As in Hunt's previous model, the first term in the braces { } for dendrites is an alloy dependent constant. For dendritic growth, even though Hunt and Kurz and Fisher applied different arguments, very similar expressions for dendritic growth were obtained. In fact, the only difference was in the derived alloy dependent constants.

Although overly simplistic, these two analytic models provide excellent insight into the growth mechanisms and qualitative agreement with experimental data. More exacting models are now under development. Hunt and Lu <sup>[14,15]</sup> have reported predictions of spacing from time dependent finite-difference models of solute transport during array growth of cells and dendrites. Fully self-consistent solutions were produced for axisymmetric interface shapes for well aligned growth conditions. The analytic relationship of the results of the numerical models is:

$$\lambda_1 = 0.156(\Gamma k)^{a_d+0.4} D^{-a_d} \Delta T_0^{-a_d+0.2} \left(1 - \frac{V_c}{V}\right)^{\frac{3}{4}} G^{-0.6} V^{a_d} \quad (4)$$

where  $V_c$  is the critical velocity where the interface will break down from a planar to a cellular structure and  $a_d$  is a gradient dependent exponential factor. An important feature of the numerical approach was that the spacing selection mechanism was incorporated and no *a priori* assumptions were required (marginal stability, minimum undercooling, etc.). The critical spacing was

considered achieved when the composition along the cell groove was nearest in composition to the equilibrium composition line. A principal result was that spacing deviations below the critical array spacing led to overgrowth. Although the model was originally established for cells, it was extended to dendritic growth when it appeared to provide reasonable predictions for dendritic structures. Finally, Hunt and Lu's model didn't consider the effect secondary arms or possible transverse thermal gradients.

Recently, Ma and Sahm<sup>[16]</sup> proposed a new analytic model to explain the variation in primary arm spacing with growth velocity and specifically included the effects of secondary arm growth on primary dendrite arm spacing. Ma and Sahm's analysis concluded that:

$$\lambda_1 = 2\pi(kD\Gamma\Delta T_0)^{\frac{1}{4}}\left(1 - \frac{V_c}{V}\right)^{\frac{3}{4}}G^{-\frac{1}{2}}V^{-\frac{1}{4}} \quad (5)$$

In this model, dendritic growth was resolved into 2 parts - growth of the dendritic center core and growth of side arms. The arm spacings are considered to be the sum of the dendrite core diameter and twice the sidearm length. The dendritic core diameter was directly related to dendrite core tip radius  $R$ . The side arm length was determined by the local free growth time and growth velocity until the side arm encountered the neighboring side arms. The side arm tip radius was assumed to be equal to the primary tip radius and the side arm growth velocity was assumed to be equal to the primary growth velocity (for dendritic growth only). Transverse (i.e., radial) thermal gradients were assumed to be negligible. As the result, this model gave a reasonable dependence of cells/dendrites spacing on the process parameters. Ma and Sahm tested their model and the Hunt and Lu<sup>[14,15]</sup> model against experimental data of  $\lambda$  vs.  $V$  for directionally solidified succinonitrile-0.35 wt. pct. acetone, SRR99 superalloy and Pb-Ti alloy and found that their model gave better agreement.

The ability of mushy zone microstructures to adjust to non-ideal (transient, mis-aligned, etc.) growth conditions is becoming of increasing interest. Han and Trivedi<sup>[4]</sup> investigated the primary dendrite spacing adjustment process in succinonitrile-acetone after sudden increases in

velocity and proposed a new lateral adjustment mechanism. Bouchard and Kirkaldy<sup>[8]</sup> evaluated the applicability of steady-state theories of Hunt and Kurz and Fisher to the unsteady-regime. Su *et al.*<sup>[17,18]</sup> found that although the primary and secondary dendrite arm spacings in Al-4.5 wt. pct. Cu quickly adjust to increases in imposed velocity, the compositional profiles adjust more slowly. Growth when the dendrites are mis-aligned with the thermal gradient was examined in succinonitrile-water alloys by Grugel and Zhou<sup>[19]</sup>. The primary dendrite arm spacing in SCN-H<sub>2</sub>O alloys was measured as a function of growth velocity and orientation angle with respect to the applied temperature gradient. The spacings were found to increase with the angle from 0° to 45° at constant composition, growth velocity and thermal gradient  $G$ . Grugel and Zhou postulated that the increase in primary spacing was due to an increase in side arm growth velocity from the off-axis thermal gradients.

While the effects of  $V$  and  $G$  on primary arm spacings have been extensively investigated with simple binary alloys, experimental data on high melting point multi-component alloys, particularly at very low thermal gradients consistent with production conditions, are limited. These experiments were designed to investigate the cellular and dendritic solidification behavior of the multicomponent Ni-base superalloy PWA 1484 over a wide range of imposed solidification velocities  $V$  and thermal gradients  $G$ .

## II. Experimental Procedures

Cylindrical bars of PWA 1484 with 1.9 cm diameter and 20 cm length were directionally solidified by Howmet Corp., Whitehall, MI. The composition of the PWA 1484 alloy utilized is listed in Table 1. All sample bars were then remelted and solidified in a vertical Bridgman-type furnace apparatus at Auburn University. The device features a hot zone at the top and cold zone at the bottom, divided by a thin layer of adiabatic insulation. The system is shown schematically in Figure 1. The hot zone furnace is an ATS Model 3320 which can be monitored and controlled at constant temperature up to 1600 °C. High thermal gradients were produced by a cold zone

consisting of a water cooled copper coil. Low thermal gradients were produced by a “cold” zone consisting of a custom booster furnace. Thus a wide range of thermal gradients could be obtained from 16 to  $\sim 105$  K/cm

Sample bars were contained in alumina crucibles within alumina retorts. B-type thermocouples were located at the center of the samples and shielded from the melt by alumina sheaths. The alumina retort tube was sealed at the bottom to enable evacuation followed by a purge of argon gas to minimize oxidation of the alloy at elevated temperatures. The sample, crucible and retort assembly were attached to a Parker Compumotor drive system that allowed precise control of sample withdrawal velocity via computer. All the alloy bars were remelted and soaked for at least 60 min at the desired elevated temperature prior to initiating withdrawal and solidification. Withdrawal velocities varied between 0.00005 cm/sec to 0.01 cm/sec.

The as-cast directionally solidified samples were lightly sanded and macro-etched to reveal the surface grain structure and any grain and/or segregation defects prior to sectioning for microstructural analyses. After macroetching, samples were sectioned at selected locations. Transverse sections, perpendicular to the growth direction, were cut from the middle of the samples. In this region dendrite arm spacing measurements are constant along the length indicating that steady state growth conditions were achieved. Longitudinal sections 2cm long in the growth direction were also cut from the center of the cylindrical bar and immediately adjacent to the previously described transverse section. The sectioned pieces were mounted, ground and polished by standard metallographic techniques. All polished samples were etched for metallographic examination using a fresh solution of 10 ml HCl + 10 ml HNO<sub>3</sub> + molybdic acid 0.3 gm+15 ml distilled water.

Metallographic examination was performed with an Olympus PME3 inverted metallurgical microscope. The transverse samples were used to determine the primary dendrite arm spacing  $\lambda_1$ , and longitudinal sections were used for the assessment of secondary dendrite arm spacing  $\lambda_2$ .  $\lambda_1$  was calculated by using the relationship  $\lambda_1 = (A/N_1)^{0.5}$ , where  $A$  is the area within

which the number of dendrites  $N_1$  was counted.  $\lambda_2$  was calculated by using  $\lambda_2 = N_2/L$ , where  $L$  is the length of well-aligned dendritic trunks and  $N_2$  is the number of secondary dendrite arms along the segment  $L$ .

Elemental distributions were measured by energy dispersive spectroscopy (EDS) in a JEOL 840 scanning electron microscope on transverse and longitudinal sections of a typical as-cast sample grown at  $V=0.0005$  cm/sec and  $G=40.6$  K/cm. Compositional analyses were performed on dendritic trunks, interdendritic regions, and secondary phases. The elemental partition ratio for each element was estimated as  $k = C_s/C_L$  where  $C_s$  is the composition of the element at the center of a dendrite trunk, and  $C_L$  is the average composition at the center of the interdendritic region.

### III. Results and Discussion

#### (A) Directional Solidification Morphology

Figures 2 and 3 illustrate the microstructures observed in typical transverse and longitudinal sections of samples solidified over a range of velocities at high thermal gradient (54-105 K/cm) and low thermal gradient (20-31 K/cm), respectively. The growth velocities utilized are indicated on the figures and varies from 0.0005 to 0.01 cm/sec. The cells and dendrite cores exhibited excellent alignment with the axial thermal gradients imposed. The basic solidification microstructure of these samples is comprised of dendritic primary  $\gamma$  along with precipitates of  $\gamma'$  and metal carbides (MC) distributed throughout the interdendritic area. The average compositions of the various phases are listed in Table 1.

The samples also displayed a transition from well developed dendrites with tertiary arms (Figures 2a and 3a) to flanged cells (Figures 2c and 3c). Some authors characterize the microstructures shown in Figures 2c and 3c as cellular dendrites. The experimental velocities for transition from cellular to dendritic growth ( $V_t$ ) can be difficult to evaluate as there is often

inconsistency on the terminology employed in the literature. Some researchers prefer to describe a microstructure as dendritic only when secondary branches can be discerned, e.g., Flemings<sup>[20]</sup>. Cells grow without significant regard to the crystallographic orientation of the crystal structure. However, Kurz and Fisher<sup>[21]</sup> note that there is a range of intermediate forms (dendritic cells and cellular dendrites) when various degrees of crystallographic directionality persist in the growth form even though no secondary arm development has occurred. The samples shown in Figures 2c and 3c exhibit microstructures where the underlying crystallographic orientation is clearly important in the growth process, but no secondary dendrite arms were exhibited in the as-cast condition.

Samples were also grown at  $V = 0.0001$  and  $0.00005$  cm/sec with  $G = 40$  K/cm. Each sample was grown for approximately 6 cm and then quenched to preserve the mushy zone microstructure. Transverse and longitudinal sections of these samples are shown in Figure 4. Examination of the cells near their tips in the longitudinal section shows evidence of secondary arms on some cells at growth velocities as low as  $0.00005$  cm/sec. These secondary arms were preserved from elimination by coarsening phenomena by the rapid cooling of the quenching process. Thus it appears that this sample is in transition from cellular to dendritic growth and  $V_i$  can be approximated as  $0.00005$  cm/sec. It also seems probable that the flanged cells shown in Figures 2c and 3c likely exhibited secondary arms near their dendrite tips and that this morphology degenerated into the flanged cells seen at room temperature.

*(B) Primary Dendritic and Cellular Arm Spacings:  $\lambda_1$*

Figure 5 illustrates the primary cell/arm spacings ( $\lambda_1$ ) of PWA1484 correlated with the process parameter  $G^{-1/2}V^{1/4}$ . The velocities utilized and the morphology of each sample's microstructure at room temperature (cellular, flanged cellular, mixed cellular/dendritic, or dendritic) are identified by the symbols in Figure 5. At the highest values of  $G^{-1/2}V^{1/4}$  (i.e., lowest



cooling rates), the samples exhibited cellular microstructures after cooling to room temperature. At the lowest values of  $G^{-1/2}V^{1/4}$  (i.e., highest cooling rates), the samples exhibited well aligned dendritic microstructures with secondary arms. Intermediate values of  $G^{-1/2}V^{1/4}$  yielded samples which displayed mixed results. Intermediate values of  $G^{-1/2}V^{1/4}$  utilizing high velocities (e.g. 0.005 and 0.01 cm/sec and low gradients) produced dendritic microstructures. Intermediate values of  $G^{-1/2}V^{1/4}$  with a low velocity of 0.0005 cm/sec produced flanged cellular microstructures. Intermediate values of  $G^{-1/2}V^{1/4}$  with an intermediate velocity of 0.0025 cm/sec produced microstructures with mixed flanged-cellular and dendritic growth. The results of Figure 5 show two distinct growth regimes: (1) dendritic growth with a marked dependence of  $\lambda_1$  on the imposed process parameter  $G^{-1/2}V^{1/4}$  and (2) cellular growth with a much smaller dependence of  $\lambda_1$  on the imposed process parameter  $G^{-1/2}V^{1/4}$ .

In order to better understand the individual roles of  $V$  and  $G$ , as opposed to their coupled effects as exhibited by the theoretical growth parameter  $G^{-1/2}V^{1/4}$ , the experimentally determined primary spacings are plotted versus  $V$  in Figure 6. The gradients achieved in the samples are also shown in Figure 6 and lines approximating constant  $G$  for 3 representative thermal gradients have been estimated and are also included. As noted before, exclusively dendritic microstructures were exhibited at  $V > 0.0025$  cm/sec while exclusively cellular microstructures were exhibited at  $V < 0.0025$  cm/sec. Mixed microstructures of cells and dendrites were seen at  $V = 0.0025$  cm/sec for all gradients. In addition, Figure 6 shows that for all  $G > 30$ -33 K/cm,  $\lambda_1$  decreases with increasing  $V$ , as expected. However, for a low gradient of  $G < 30$  K/cm,  $\lambda_1$  first decreases with increasing  $V$  for  $0.0001 < V < 0.001$  cm/sec but then unexpectedly increases with increasing  $V$  for  $V > 0.001$  cm/sec. For velocities as low as these, theoretical considerations indicate that the primary spacing should always decrease with an increasing velocity,<sup>[11,12,14]</sup> unless the thermal gradient also decreases with increasing velocity as seen by H.Jamgotchian *et al.*<sup>[22]</sup> and Grugel *et al.*<sup>[19]</sup> Decreases in experimental thermal gradient can not explain the unusual behavior seen in

the present samples as the axial thermal gradient was reasonably constant at 20~26 K/cm for these samples.

The physiochemical properties of PWA 1484 required for the theoretical analysis are shown in Table 2. A 2.5 cm long and 1.9 cm diameter sample of PWA1484 with a thermocouple inserted in the center was melted and frozen 6 times. The cooling curves obtained were evaluated by the method of Backerud<sup>[23]</sup> to identify the fraction solid  $f_s$  vs. temperature relationship. The maximum and minimum experimental curves thus obtained are shown in Figure 7. In addition, the fraction solid vs. temperature relationship was estimated using Scheil's equation,<sup>[8]</sup> assuming that the liquidus and solidus are straight lines, viz.,

$$f_s = 1 - \left[ \frac{T_m - T}{T_m - T_o} \right]^{1/(k-1)}. \quad [6]$$

A pseudo-binary partition coefficient of  $k=0.83$  is seen in Figure 7 to give good agreement with the observed solidification behavior. Such a pseudo-binary partition coefficient is in agreement with the elemental partition coefficients shown in Table 1. In addition,  $\Delta T_o$  of PWA1484 was found to be 75 K. The Gibbs-Thomson coefficient  $\Gamma$  is approximately  $1 \times 10^{-5}$  cm K for a number of alloys.<sup>[21]</sup> This value was utilized in the theoretical estimations below. The mean diffusion coefficient  $D$  in the liquid was determined following the theory of constitutional supercooling where  $D = \Delta T_o V_c / G$ .<sup>[21]</sup> The critical velocity for planar growth was estimated as  $V_c = kV$ , following Kurz and Fisher.<sup>[12]</sup>

The present primary spacing results were compared to the established theoretical models proposed by Hunt and Lu<sup>[14,15]</sup> and Ma and Sahm<sup>[16]</sup> in Figures 8a-d. In these figures, the Ma and Sahm relationship, i.e. Eq. [5] above, is plotted as a solid line and the Hunt and Lu relationship, i.e., Eq. [4] above, is plotted as a dashed line. As seen in Figures 8a – 8d, excellent agreement was found between the trends of the experimental data and the predicted primary arm spacings from the model of Ma and Sahm for all thermal gradients investigated. However, close inspection of Figure 8d shows that the experimentally determined primary arm spacings increase with

increasing velocity while both Ma and Sahm's model and Lu and Hunt's model predict that the spacings should decrease with increasing  $V$ . This unusual behavior was examined more closely as discussed below.

### *(C) Effects of Off-Axis Heat Flow*

The theoretical model proposed by Hunt and Lu<sup>[14,15]</sup> assumes no transverse thermal gradients and neglects the growth of secondary arms. Although Ma and Sahm's model<sup>[16]</sup> includes the effects of secondary arms, transverse thermal gradients are also assumed to be negligible. However, high growth velocities during directional solidification can move a sample's mushy zone down and out of the adiabatic zone, thus producing non-negligible transverse (i.e., radial) thermal gradients, especially when the axial thermal gradients being utilized are themselves quite low. Analysis of thermocouples placed along the centerline and along the outsides of samples showed that when  $G < 30$  K/cm, the ratio of radial to longitudinal thermal gradient ( $G_r/G$ ) varied from 0.9, 0.5, and 0.2, respectively for velocities of 0.01, 0.005, 0.0025 cm/sec. All other experimental conditions reported in this paper produced  $G_r/G < 0.01$ .

Only the Ma and Sahm model<sup>[16]</sup> incorporated the phenomenon of secondary arm growth during dendritic solidification. In that model, the dendrite tip radius of the side arms was assumed to be equal to the dendrite tip radius of the primary trunks and the growth velocity of the side arms was assumed to be related to the longitudinal growth velocity  $V$  by  $V_s = V(1 - V_c/V)$ , where  $V_c$  is the critical velocity for planar interface instability. It seems reasonable to assume that if  $G_r > 0$ , then the mean side arm growth velocity would be increased. With such a modification, Ma and Sahm's analysis could be applicable to growth conditions where the dendrites are not aligned with the thermal gradient.

Grugel and Zhou<sup>[19]</sup> investigated the effects of off-axis heat flow on the primary dendrite spacings for succinonitrile-1.4 and 4.7 wt. pct. water alloys and found good empirical correlation

between the spacings and the angular relationship between the dendrite growth direction and the total thermal gradient. Grugel and Zhou defined the orientation angle  $\phi$  such that

$$\tan(\phi) = \frac{G_T}{G} \quad (7)$$

where  $G_T$  is the thermal gradient in the transverse direction and  $G$  is the thermal gradient in the longitudinal direction. These researchers found that the primary spacings increased with misalignment angle from 0-40° for constant conditions of composition, velocity, and thermal gradient. For increasing angles from 50-70°, the secondary arms assumed the roles of primaries and the spacings rapidly decreased. Grugel and Zhou correlated  $\lambda_1$  with the heat flow geometry and found for the succinonitrile-1.4 wt. pct. water alloy that

$$\lambda_1(\phi) = \lambda_1(\phi=0) + 120 \tan^2\phi \quad (\mu\text{m}) \quad (8)$$

where the 120 factor is an empirical determined fitting parameter. Thus the primary spacings of the samples in the misaligned thermal field were equal to the theoretical spacings during aligned growth ( $\phi=0$ ) plus a correction factor that depended upon the misalignment angle  $\phi$ . Although the data were limited, Grugel and Zhou found a correction factor of approximately  $260\tan^2\phi$  for misaligned growth in succinonitrile-4.7 wt. pct. water alloy. Thus the factor in front of the  $\tan^2\phi$  term does not appear to be constant. More work on the basis of this factor is clearly needed.

The high velocity, low thermal gradient samples of the present investigation exhibited non-negligible radial thermal gradients within the mushy zone. Thus the theoretically predicted primary spacings from the Ma and Sahm model in Figure 8d were adjusted by adding an empirical correction factor equal to  $120 \tan^2\phi$ , as Grugel and Zhou found for succinonitrile-1.4 wt. pct. water alloy. The results are listed in Table 3 and shown in Figure 9. Good agreement between the experimentally determined primary spacings and the modified theoretical predictions can be seen in Figure 9 where the radial temperature gradients increase the mean primary spacings as  $V$  decreases.

Misalignment of growth direction and thermal gradient provides for enhanced growth of the secondary arms that find themselves rotated closer to the maximum thermal gradient. Conversely, secondary arms on the opposite side will find their growth retarded since they are rotated away from the maximum thermal gradient. In the limit of a complete rotation through  $90^\circ$ , the secondary arms would become primary arms. Such conditions could be realized by rapid withdrawal of a sample from the furnace followed by air cooling. Quantitative theoretical treatment of the effects of misalignment would require numerical modeling the coupled solute/thermal diffusion fields at the dendrite tips.

#### IV. Summary

Directional solidification experiments were performed on PWA1484, a complex multi-component nickel-base superalloy. Solidification velocities were varied from 0.00005 to 0.01 cm/sec and thermal gradients varied from 16-105 K/cm. A range of aligned solidification microstructures were exhibited by the alloy when examined as-cast at room temperature: aligned dendrites with well developed secondary and tertiary arms; flanged cells aligned with the growth direction and without secondary arms; and cells with no evidence of flanges or secondary arms. Quenched directional solidification experiments indicated that although no secondary arms were present in the as-cast condition, secondary arms were present in the vicinity of the cell tips during solidification. Presumably coarsening phenomena eliminated the secondary arms during cooling through the mushy zone.

The well-known exponential equation ( $\lambda_1 \propto G^{-1/2} V^{-1/4}$ ) describing primary arm spacing  $\lambda_1$  with thermal gradient  $G$  and solidification velocity  $V$  exhibits excellent agreement with experimental data for PWA1484. However, the constant of proportionality is different depending upon whether the solidification microstructure contains secondary arms or not. The presence of secondary arms increases the spacing between dendrites and leads to a greater sensitivity of  $\lambda_1$  on

$G^{-1/2}V^{1/4}$ . When the secondary arms are not preserved in the room temperature microstructure, the primary spacing is much less sensitive to changes in the solidification parameter  $G^{-1/2}V^{1/4}$ .

More recent theoretical models of cellular and dendritic growth by Hunt and Lu and Ma and Sahm have been tested against the primary spacing data of PWA1484. The model of Ma and Sahm provided excellent agreement over a wide range of thermal gradients, solidification velocities, and microstructural morphologies. Only minor corrections were needed to Ma and Sahm's model to account for off-axis heat flow during solidification experiments at the highest velocities (0.01 cm/sec) and lowest thermal gradients.

### Acknowledgments

This material is based upon work supported by, or in part by, the U.S. Army Research Office under grant number ARO DAAHO4-96-I-0321 and the National Aeronautics and Space Administration under cooperative agreement number NCC8-128. The samples were graciously provided by Howmet Corporation, Whitehall, MI. Technical discussions and the assistance of Dr. Boyd Mueller and Mr. Terry Simon of Howmet Corporation in preparing the investment cast precursor bars are especially appreciated.

## References

1. J. R. Sarazin, A. Hellawell: *Metall. Trans.*, 1988, vol.19A, pp. 1861-1871.
2. S.N. Tewari and R.Shah: *Metall. Mater. Trans.*, 1996, vol.27A, pp. 1353-1362.
3. T.M. Pollock and W.H. Murphy: *Metall. Mater. Trans.*, 1996, vol.27A, pp. 1081-1094.
4. S.H. Han and R.Trivedi: *Acta metall. mater.*, 1994, vol.42, pp. 25-41.
5. H.K. Kim, J.C. Earthman and E.J.Lavernia: *Acta metall. mater.*, 1992, vol.40, pp. 637-647.
6. M. Vijayakumar and S.N. Tewari: *Mater. Sci and Eng.*, 1991, vol.A132, pp. 195-201.
7. M.A. Chopra and S.N. Tewari: *Metall. Trans.*, 1991, vol.22A, pp. 2467-2473.
8. D.Bouchard and J.S. Kirkaldy: *Metall. Mater. Trans.*, 1997, vol.28B, pp. 651-663.
9. K. Somboonsuk, J.T. Mason and R.Trivedi: *Metall. Trans.*, 1984, vol.15A, pp. 967-975.
10. R.Trivedi: *Metall. Trans.*, 1984, vol.15A, pp. 977-982.
11. J.D Hunt: *Solidification and Casting of Metals*, The Metals Society, London, 1979, pp. 3-9.
12. W. Kurz and D.J.Fisher: *Acta Metallurgica*, 1981 vol.29, pp. 11-20.
13. J.S. Langer and H. Möller-Krumbhaar, *J. Crystal Growth*, vol. 42, 1977, pp. 11-23.
14. J.D. Hunt and S.Z. Lu: *Metall. Trans.*, 1996, vol.27A, pp. 611-623.
15. S.Z. Lu and J.D. Hunt: *J. Crystal Growth*, 1992, vol.123, pp.17-34.
16. D. Ma and P. Sahm: *Metall. Mater. Trans.*, 1998, vol.29A, pp. 1113-1119.
17. R. J. Su, Ruel. A. Overfelt and W.A. Jemian: *Metall. Mater. Trans*, 1998, vol 29A, pp. 2375-2381.
18. R.J. Su, W.A. Jemian and Ruel. A. Overfelt: *J. Crystal Growth*, 1997, vol.179, pp. 625-634.
19. R.N. Grugel and Y.Zhou: *Metall. Trans.*, 1989, vol.20A, pp. 969-973.
20. M.C. Flemings: *Solidification Processing*, McGraw-Hill Inc., New York, 1974, pp. 66-77.
21. W. Kurz and D.J. Fisher: *Fundamentals of Solidification*, Trans Tech Publications, Aedermannsdorf, Switzerland, 1992, pp. 65-69.
22. H. Jamgotchian, B.Billia, and L. Capella: *J. Crystal Growth*, 1983, vol.64, pp. 338-344.
23. L. Backerud, G.Chai, and J.Tamminen: *Solidification Characteristics of Aluminum Alloys, Vol 1: Wrought Alloys*, AFS/Skanaluminium, Des Plaines, IL 1990, pp. 65-70.

## List of Tables

1. Average Compositions of the Solidification Phases
2. Physiochemical Materials Data for PWA1484
3. Calculations of the Effects of Off-Axis Heat Flow

## List of Figures

1. Schematic of the Bridgman Directional Solidification Apparatus
2. Typical microstructures of directionally solidified samples under high thermal gradients (54-105 K/cm) and a range of solidification velocities. Axial thermal gradients and solidification velocities utilized are shown.  
Top: tranverse sections; botton: longitudinal sections.
3. Typical microstructures of directionally solidified samples under low thermal gradients (20.4-31.1 K/cm) and a range of solidification velocities. Axial thermal gradients and solidification velocities utilized are shown.  
Top: tranverse sections; botton: longitudinal sections.
4. Cellular microstructure of the quenched mushy zone of samples solidified at:
  - (a)  $V = 0.0001$  cm/sec and  $G = 40$  K/cm, and
  - (b)  $V = 0.00005$  cm/sec and  $G = 40$  K/cm.
5. The primary arm spacings as a function of the solidification parameter  $G^{-1/2}V^{1/4}$ . The velocities utilized and microstructures exhibited are shown.
6. The primary arm spacings as functions of the solidification velocity for the range of thermal gradients shown.  $G^{-1/2}V^{1/4}$ . The microstructures exhibited by the samples are also shown.
7. Temperature vs. fraction solid relationship for PWA1484. Minimum and maximum of a sample melted and frozen 6 times as well as estimates using Scheil's Eq.
8. Comparison of the growth velocity dependence of the primary spacing of PWA1484 with theoretical predictions.
  - (a)  $G_{theoretical} = 100$  K/cm
  - (b)  $G_{theoretical} = 60$  K/cm
  - (c)  $G_{theoretical} = 34$  K/cm
  - (d)  $G_{theoretical} = 25$  K/cm
9. Comparison of the growth velocity dependence of the primary spacing of PWA1484 with theoretical predictions from model of Ma and Sahn<sup>[16]</sup> modified for off-axis heat flow with  $G_{expt} \sim 20-26$  K/cm and  $G_{theoretical} = 25$  K/cm



**Table 1.****PWA 1484 Composition Distribution Data**(Solidified at  $V = 0.0005$  cm/sec. and  $G = 40.6^\circ\text{C/cm}$ )

	Al	Cr	Co	Mo	Ta	W	Re	Ni
Bulk alloy composition*	5.66	4.96	9.88	1.89	8.74	5.86	2.98	60.03
Dendritic trunk( $\gamma$ )	4.51	5.28	9.57	1.93	7.43	9.55	4.70	57.03
Interdendritic( $\gamma+\gamma'$ )	5.07	5.65	9.07	2.24	10.39	7.39	2.58	57.61
$k$ , partition ratio	0.89	0.93	1.06	0.86	0.72	1.29	1.82	
Gamma prime( $\gamma'$ )	6.74	2.01	6.42		18.62	3.63		62.58
Carbides(MC)					95.86			4.14

\* alloy composition (wt%): data reported from alloy supplier.

**Table 2.****Physiochemical Data of PWA1484 Used in the Theoretical Analysis**

<u>Parameter</u>	<u>Value</u>
$k$	0.83
$\Gamma$ , K cm	$1 \times 10^{-5}$
$D$ , $\text{cm}^2/\text{s}$	$2 \times 10^{-5}$
$\Delta T_o$ , K	75

**Table 3**  
**Calculations of the Effect of Off-Axis Heat Flow**  
( $G_{\text{theoretical}} = 25 \text{ K/cm}$ )

Velocity (cm/s)	$G_r/G$	$\tan^2 \phi$	$\lambda_l$ (Ma & Sham)	$\lambda_l$ (modified)
0.01	0.9	0.81	419	516
0.005	0.5	0.25	498	528
0.0025	0.2	0.04	592	596
0.001	0	0	740	740

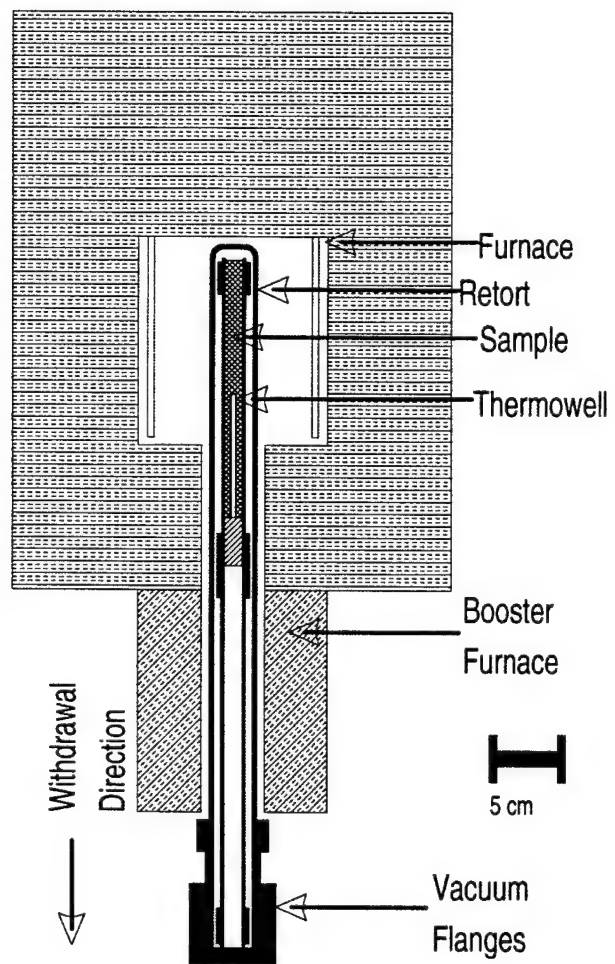
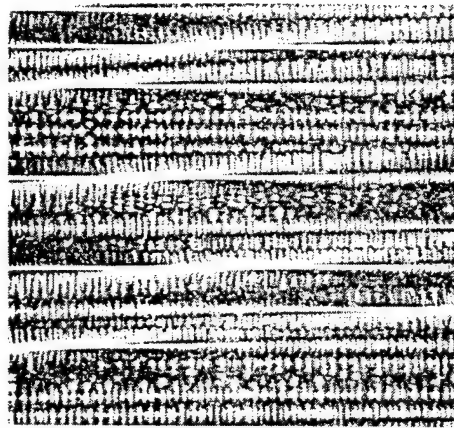
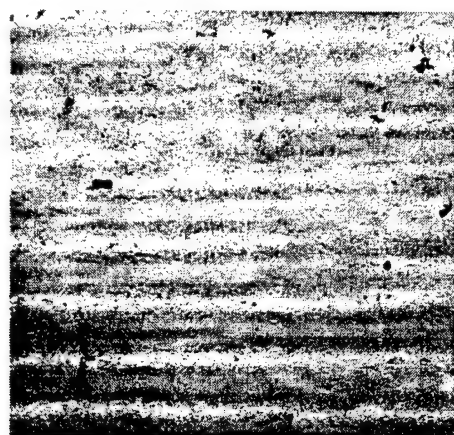
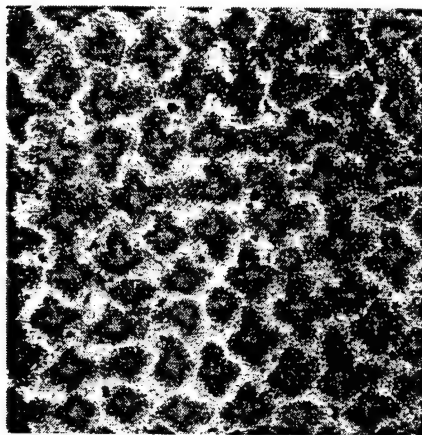
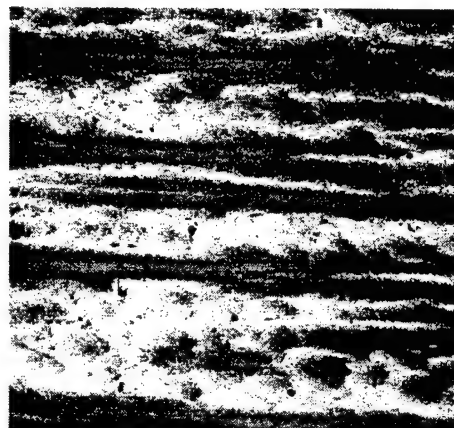
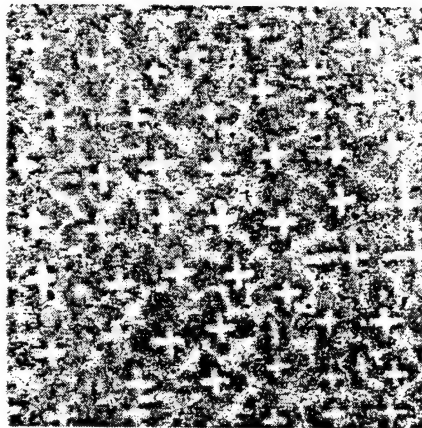


Fig 1



500  $\mu\text{m}$

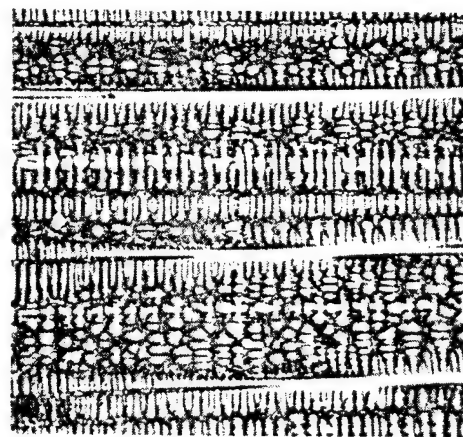
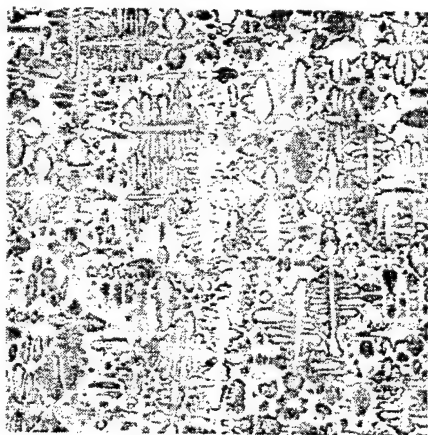


(a)  $V=0.01\text{cm/sec}$ ;  $G=105\text{K/cm}$

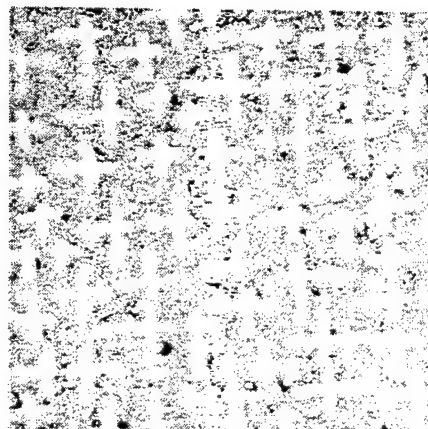
(b)  $V=0.001\text{cm/sec}$ ;  $G=88\text{K/cm}$

(c)  $V=0.0005\text{cm/sec}$ ;  $G=54\text{K/cm}$

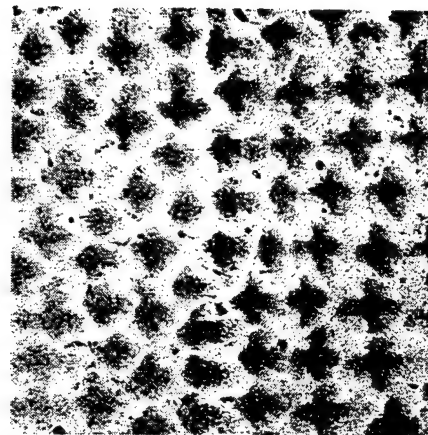
**Figure 2**



(a)  $V=0.01$  cm/sec;  $G=20.4$  K/cm



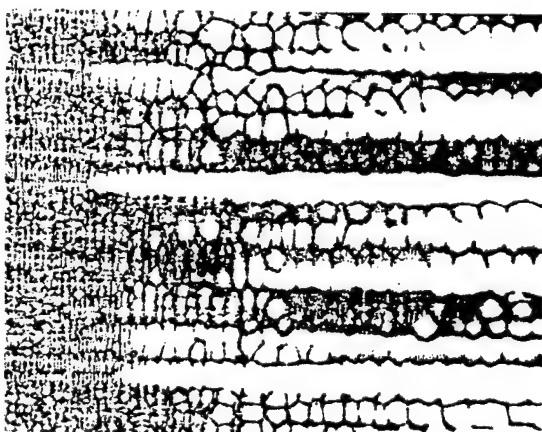
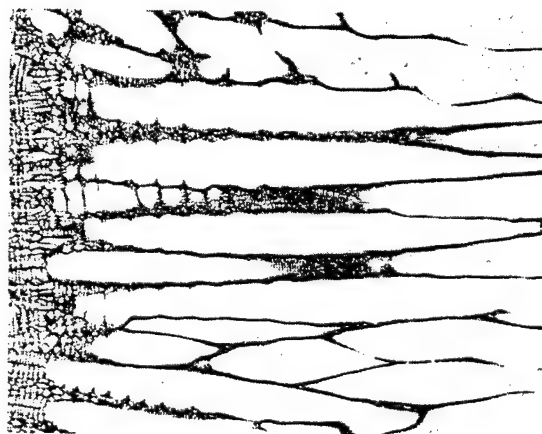
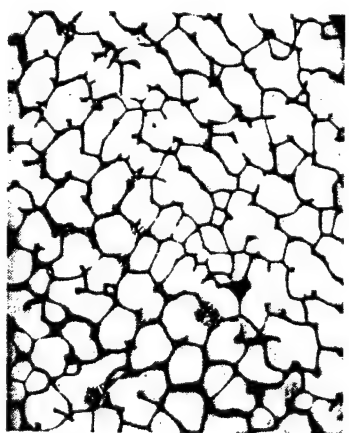
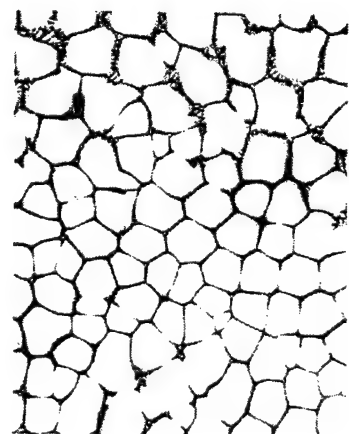
(b)  $V=0.001$  cm/sec;  $G=31.1$  K/cm



(c)  $V=0.0005$  cm/sec;  $G=25.8$  K/cm

500 $\mu$ m

**Figure 3**



500  $\mu\text{m}$

(b)  $V=0.00005$  cm/sec;  $G=40$  K/cm

(a)  $V=0.0001$  cm/sec;  $G=40$  K/cm

Fig. 4

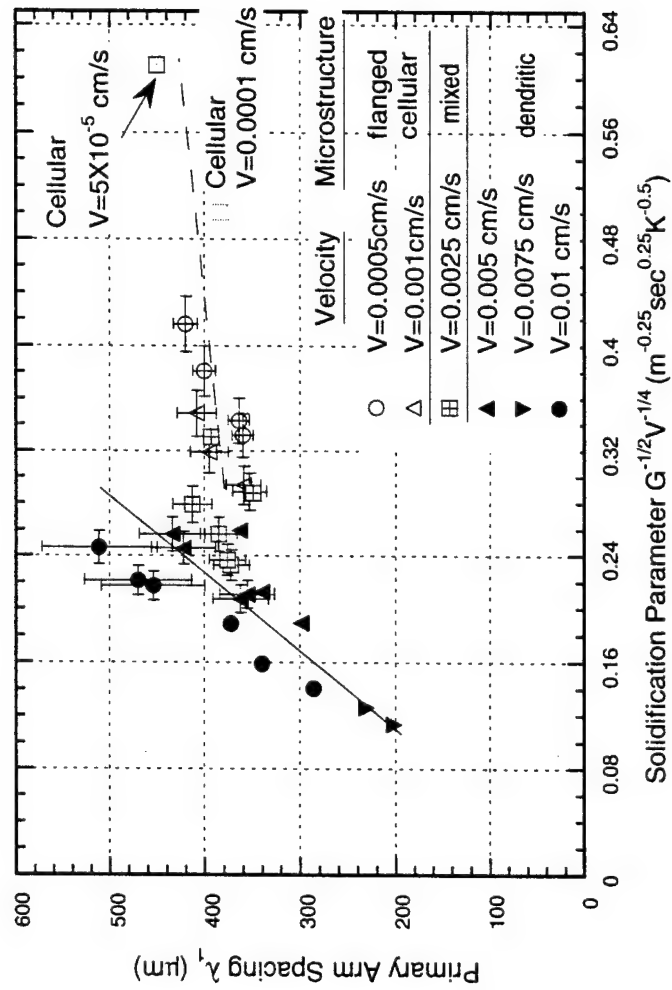


Fig. 5

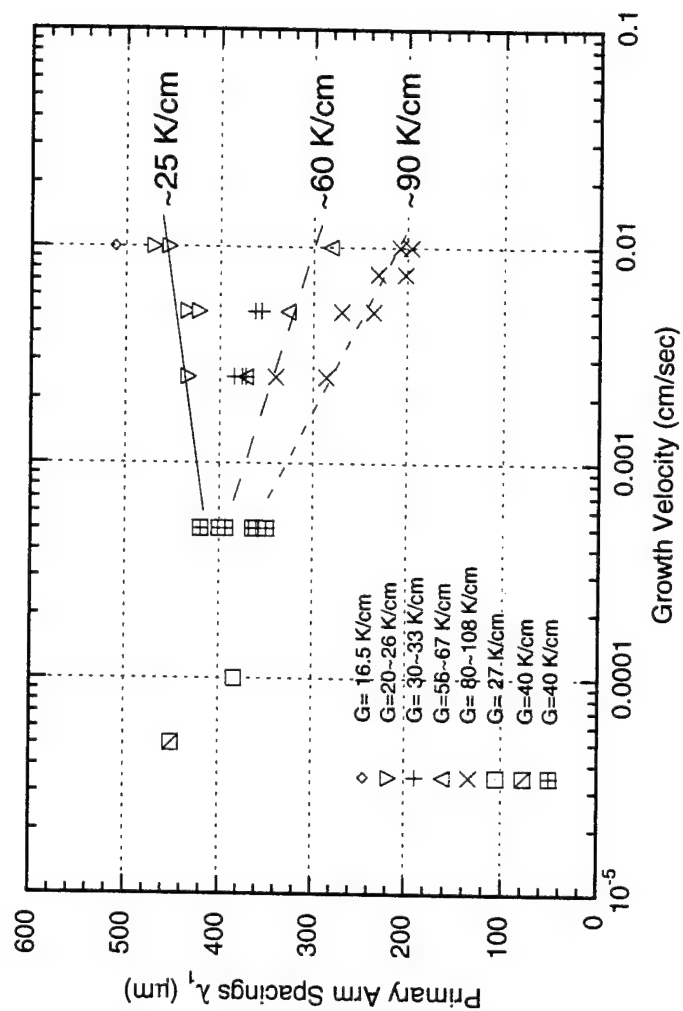


Fig. 6



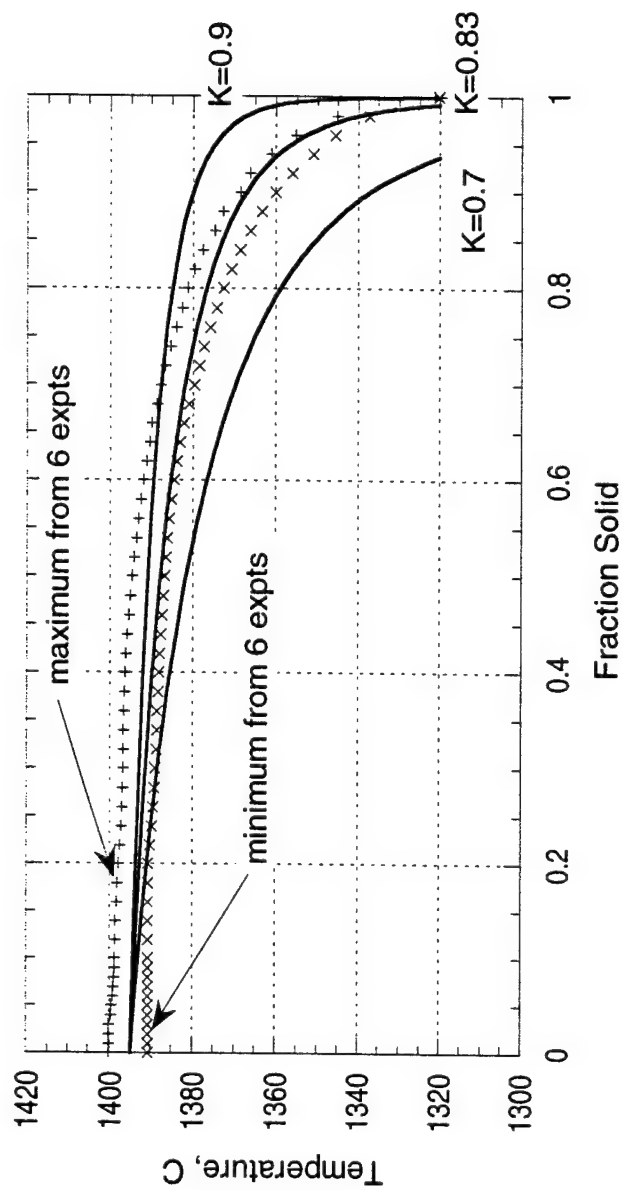


Fig 7

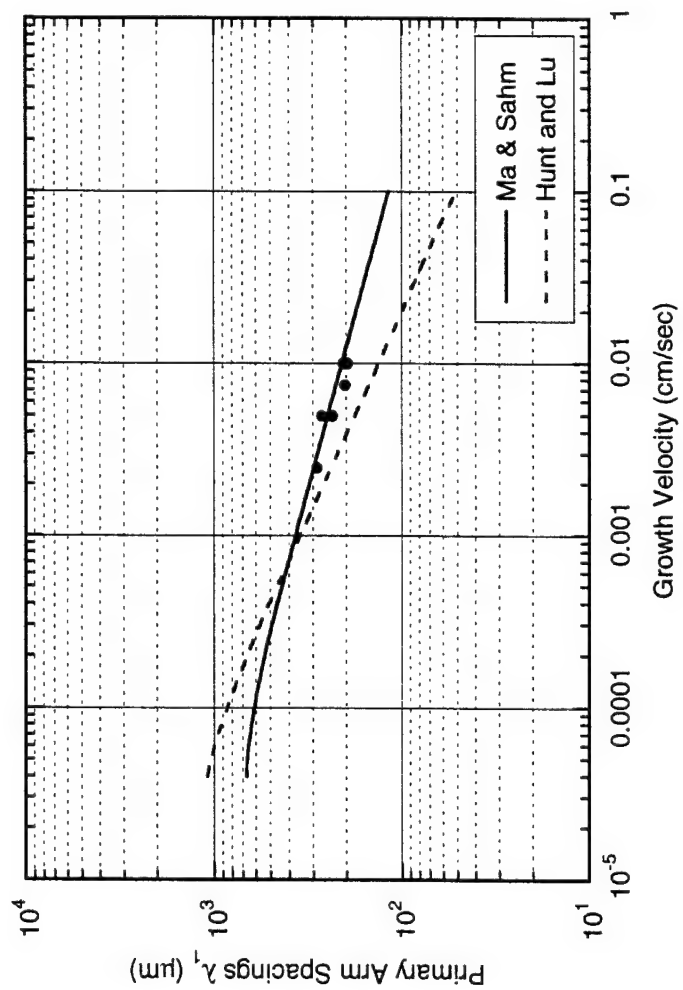


Fig 8a

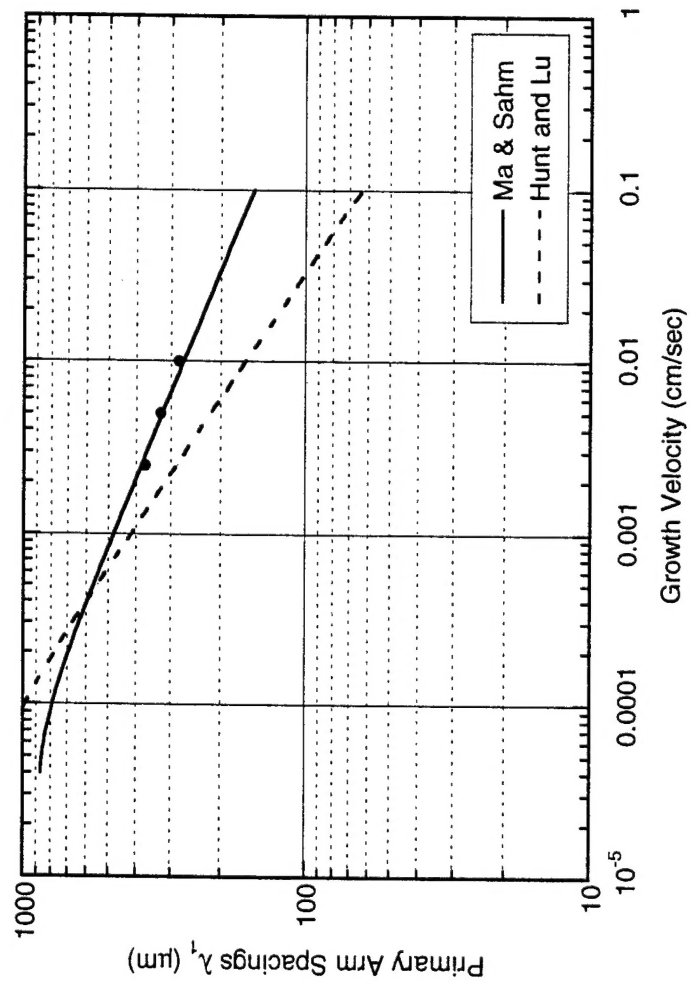


Fig 8b

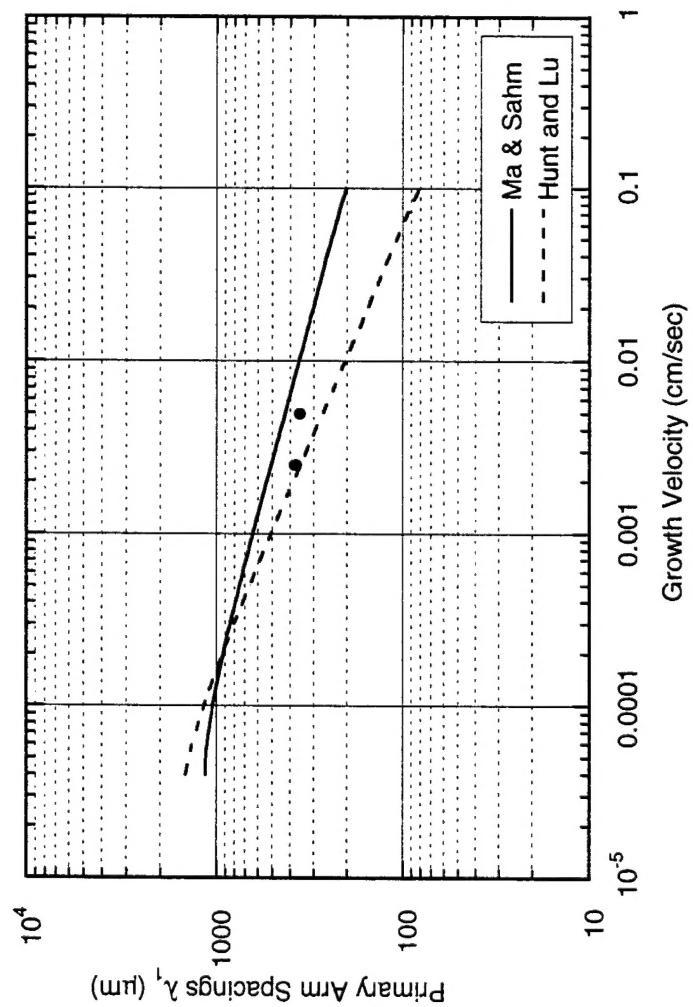


Fig 8c

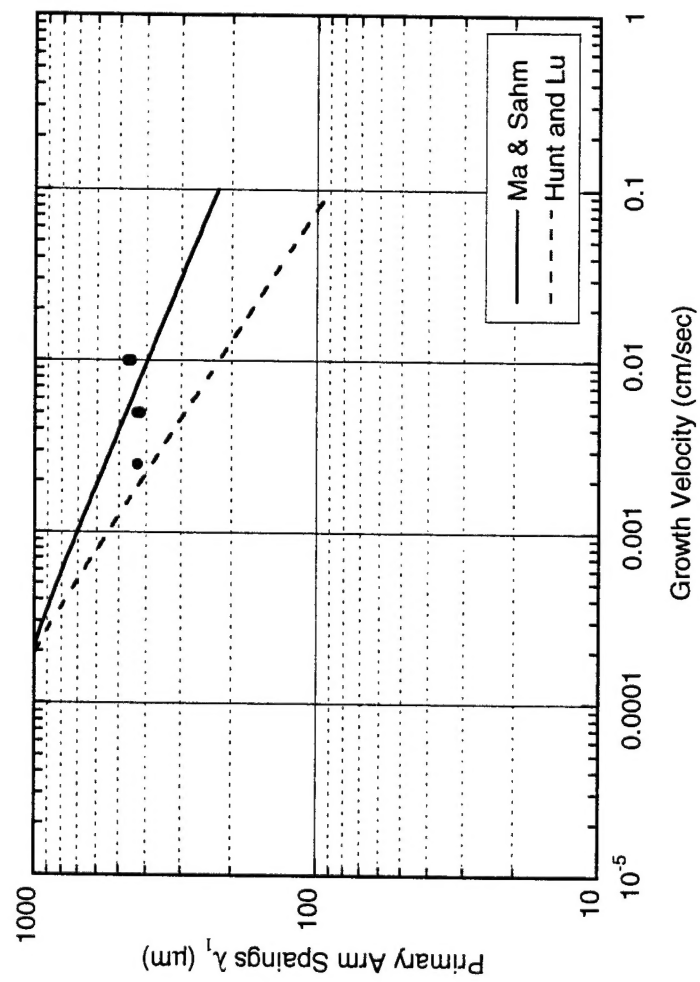


Fig. 8d

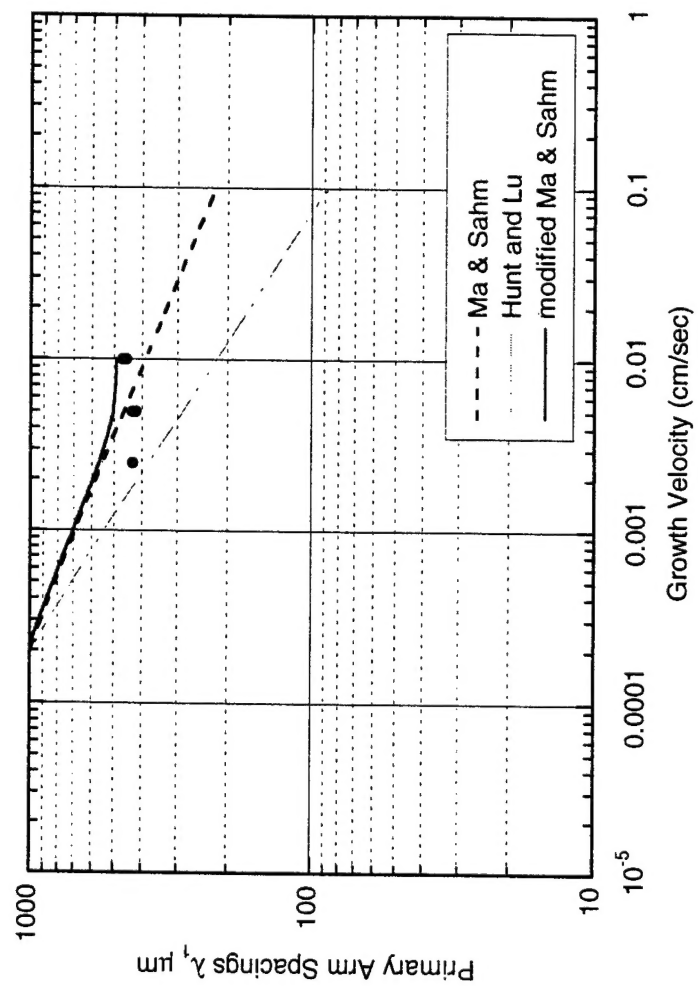


Fig 9